Shaping Mechano-Responsiveness

3D-Printing of Piezoelectric and Living Materials

Ammu, S.K.

DOI
10.4233/uuid:62db8d80-bbb9-4bbe-948e-e148b0beaaca

Publication date
2025

Document Version
Final published version

Citation (APA)
Ammu, S. K. (2025). *Shaping Mechano-Responsiveness: 3D-Printing of Piezoelectric and Living Materials*. [Dissertation (TU Delft), Delft University of Technology]. https://doi.org/10.4233/uuid:62db8d80-bbb9-4bbe-948e-e148b0beaaca

Important note
To cite this publication, please use the final published version (if applicable).
Please check the document version above.

SHAPING MECHANO-RESPONSIVENESS

3D-PRINTING OF PIEZOELECTRIC AND LIVING MATERIALS

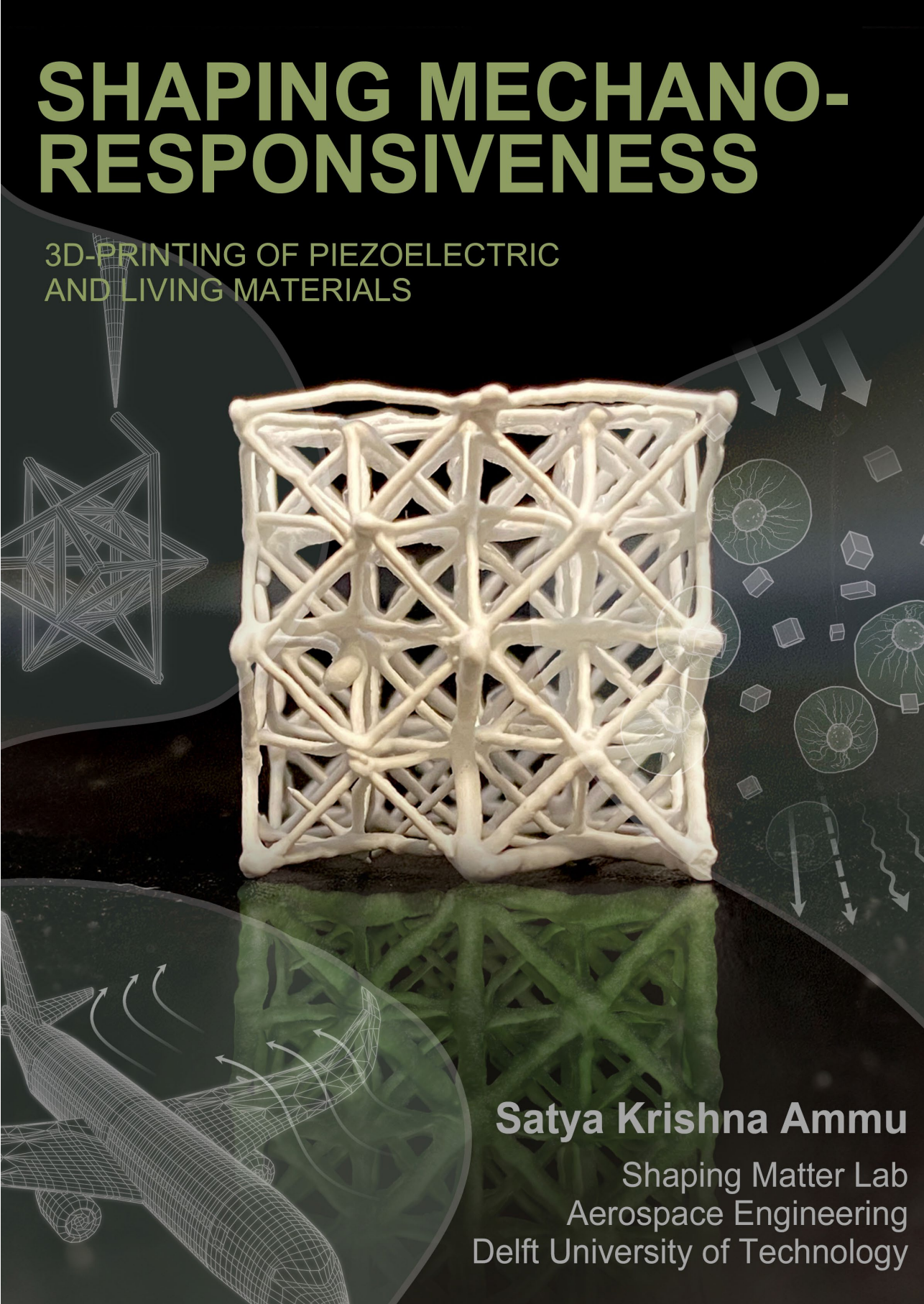

Satya Krishna Ammu

Shaping Matter Lab
Aerospace Engineering
Delft University of Technology

SHAPING MECHANO-RESPONSIVENESS

3D-PRINTING OF PIEZOELECTRIC AND LIVING MATERIALS

SHAPING MECHANO-RESPONSIVENESS

3D-PRINTING OF PIEZOELECTRIC AND LIVING MATERIALS

Dissertation

for the purpose of obtaining the degree of doctor,
at Delft University of Technology,
by the authority of the rector Magnificus Prof. dr. ir. T.H.J.J van der Hagen,
chair of the Board of Doctorates,
to be defended publicly on
Wednesday, 7th of May 2025 at 12:30

by

Satya Krishna AMMU

Master of Science in Aerospace Engineering,
Delft University of Technology, Delft, Netherlands
Born in Hyderabad, India

This dissertation has been approved by the promotors

Composition of the doctoral committee:

Rector Magnificus,	Delft University of Technology, chairperson
Dr. K. Masania	Delft University of Technology, promotor
Prof. C. A. Dransfeld	Delft University of Technology, promotor

Independent members:

Prof. dr. R. Benedictus	Delft University of Technology, NL
Prof. dr. C.R. Bowen	University of Bath, UK
Prof. dr. A. O. Krushynska	University of Groningen, NL
Dr. A. Hunt	Delft University of Technology, NL
Prof. dr. P. G. Steeneken	Delft University of Technology, NL, reserve member

TU Delft
Delft University of Technology

Keywords: Direct ink writing, piezoelectric, algae, pressure sensing
Printed by: Proefschriftspecialist.nl
Cover: Flyazure @ fiverr

ISBN 978-94-6384-782-7
An electronic version of this dissertation is available at
https://repository.tudelft.nl/

CONTENTS

SUMMARY

Biological systems have evolved over billions of years to achieve remarkable energy efficiency. To replicate these efficiencies in synthetic materials, it is essential to emulate the fundamental characteristics of living systems, particularly energy transduction and adaptability. Mechano-responsive materials, which convert mechanical energy into other forms of energy, show significant promise for developing adaptive materials. By integrating functional materials like piezoelectric into synthetic structures, it is possible to create systems capable of dynamic and autonomous responses inspired by nature's sophisticated mechanisms. This thesis explores the development of 3D-printed mechano-responsive synthetic and living materials, aiming to create structures that mimic the adaptability and efficiency of living organisms.

Chapter 1 establishes a foundational understanding of mechano-responsive materials, both synthetic and living and highlights the versatility of direct ink writing (DIW) as a tool for efficiently printing multiple materials with minimal waste. It reviews current literature on DIW of mechano-responsive materials.

Chapter 2 focuses on embedding synthetic mechano-responsive materials, particularly UV-curable piezoelectric ceramic-polymer composites, enabling them to be printed alongside other structural materials. This approach was used to create piezoelectric vibrating membranes co-printed with clamping structures, offering flexibility in tuning transducer dimensions and facilitating their integration into complex structures.

Chapter 3 advances the shaping complexity of these piezoelectric composites by developing an embedded in-gel DIW method to fabricate lattice structures with properties unattainable in bulk materials. A generative machine learning framework was developed to design lattice geometries with specified performance coefficients. These computationally designed lattice structures were printed within a gel without requiring support structures, ensuring directional uniformity and electrical integrity. Both gel and ink composition were optimised along with the printing path and speed to achieve features as small as 5mm, and the printed lattices were tested for their electromechanical anisotropy. Measured results show good agreement with theoretical predictions validating the approach for generating and manufacturing optimised piezoelectric lattices.

While synthetic materials offer desirable properties, they often have high embodied energy due to intensive production processes. In contrast, living materials like algae are self-sustaining and require low-temperature, low-pressure conditions to survive. The thesis explores embedding these organisms into functional materials to harness their natural properties.

Chapter 4 creates biohybrid 3D-printed structures with living materials, replicating the "living" characteristics found in nature. Hydrogels embedded with living *Chlamydomonas reinhardtii* algae cells were developed and 3D printed, with optimisation of printing and crosslinking processes to study growth distribution and photosynthesis. The study observed algae clustering at surfaces with favourable gas exchange and light conditions, suggesting that increasing surface area enhances functionality and provides insights into the requirements for engineered living materials.

Finally, Chapter 5 explores mechano-responsive living materials by embedding dinoflagellate cells into hydrogels. Building on the previous work with algae, the mechanical response of these materials was tuned to induce bioluminescence, demonstrating the potential for creating living materials with responsive functionalities.

In Chapter 6, we summarise the key findings related to DIW of mechanoresponsive materials presented in this thesis and provide recommendations and outlooks for exciting future research directions.

SAMENVATTING

Biologische systemen hebben zich over miljarden jaren geëvolueerd om opmerkelijke energie-efficiëntie te bereiken. Om deze efficiëntie in synthetische materialen na te bootsen, is het essentieel om de fundamentele kenmerken van levende systemen te imiteren, met name energieoverdracht en aanpassingsvermogen. Mechano-responsieve materialen, die mechanische energie omzetten in elektrische of chemische energie, tonen veelbelovende mogelijkheden voor de ontwikkeling van adaptieve materialen. Door functionele materialen zoals piëzo-elektrische materialen in synthetische structuren te integreren, is het mogelijk systemen te creëren die in staat zijn tot dynamische en autonome reacties, geïnspireerd door de verfijnde mechanismen van de natuur. Dit proefschrift onderzoekt de ontwikkeling van 3D-geprinte mechano-responsieve synthetische en levende materialen met ingebedde functionaliteiten, met als doel structuren te creëren die het aanpassingsvermogen en de efficiëntie van levende organismen nabootsen. Het doel is om materialen te ontwerpen die omgevingsveranderingen, zoals schade, kunnen waarnemen en erop kunnen reageren om hun prestaties en levensduur te verbeteren.

Hoofdstuk 1 legt een fundamenteel begrip van mechano-responsieve materialen, zowel synthetisch als levend, vast en benadrukt de veelzijdigheid van direct ink writing (DIW) als een tool om efficiënt meerdere materialen te printen met minimaal afval. Het hoofdstuk biedt een overzicht van de huidige literatuur over DIW van mechano-responsieve materialen.

Hoofdstuk 2 richt zich op het inbedden van synthetische mechano-responsieve materialen, met name UV-uithardbare piëzo-elektrische keramisch-polymeercomposieten, waardoor ze samen met andere structurele materialen kunnen worden geprint. Deze benadering werd gebruikt om piëzo-elektrische vibrerende membranen te creëren die samen met klemstructuren worden geprint, waardoor flexibiliteit wordt geboden in het afstemmen van transducerafmetingen en hun integratie in complexe structuren wordt vergemakkelijkt.

Hoofdstuk 3 verhoogt de complexiteit van deze piëzo-elektrische composieten door een ingekapselde gel DIW-methode te ontwikkelen om roosterstructuren te vervaardigen met eigenschappen die niet kunnen worden bereikt in bulkmaterialen. Deze structuren werden binnen een gel georiënteerd zonder ondersteunende structuren te vereisen, waardoor directionele uniformiteit en elektrische integriteit

werden gewaarborgd. Hoewel synthetische materialen wenselijke eigenschappen bieden, hebben ze vaak een hoge belichaamde energie door intensieve productieprocessen. Daarentegen zijn levende materialen zoals algen zelfvoorzienend en vereisen ze lage temperatuur- en drukomstandigheden om te overleven. Het proefschrift onderzoekt het inbedden van deze organismen in functionele materialen om hun natuurlijke eigenschappen te benutten.

Hoofdstuk 4 creëert biohybride 3D-geprinte structuren met levende materialen, waarbij de "levende" kenmerken uit de natuur worden nagebootst. Hydrogelen met ingekapselde levende Chlamydomonas reinhardtii algen werden ontwikkeld en 3D-geprint, met optimalisatie van print- en crosslinkprocessen om groeidistributie en fotosynthese te bestuderen. De studie observeerde algenclusters op oppervlakken met gunstige gasuitwisseling en lichtomstandigheden, wat suggereert dat een vergroting van het oppervlak de functionaliteit verbetert en inzicht geeft in de vereisten voor ontworpen levende materialen.

Ten slotte onderzoekt Hoofdstuk 5 mechano-responsieve levende materialen door dinoflagellaatcellen in hydrogels in te kapselen. Voortbouwend op het eerdere werk met algen, werd de mechanische respons van deze materialen afgestemd om bioluminescentie op te wekken, wat het potentieel aantoont voor het creëren van levende materialen met responsieve functionaliteiten.

In Hoofdstuk 6 vatten we de belangrijkste bevindingen met betrekking tot DIW van mechano-responsieve materialen samen die in dit proefschrift worden gepresenteerd, en geven we aanbevelingen en vooruitzichten voor spannende toekomstige onderzoekslijne

1

INTRODUCTION

1.1. EMBEDDED FUNCTIONALITY

Given the urgency in achieving net zero carbon emissions by 2050 published by the Intergovernmental Panel on Climate Change (IPCC) [1], there is a growing need for technologies with drastically reduced energy demand and less use of critical raw materials. Biological systems, having evolved over billions of years, are highly energy-efficient and serve as an excellent model for developing such technologies. To replicate these characteristics in synthetic materials, living organisms can offer key new insights. Despite the vast diversity among all forms of life, certain common characteristics shown in **Figure 1.1** enable life to thrive[2]. Among these key characteristics, energy transduction and adaptability are crucial for the sustenance and survivability of living systems.

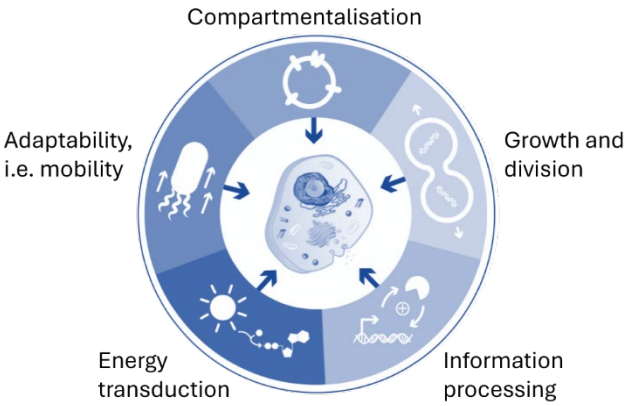

Figure 1.1: Hallmarks of living systems. Schematic illustrating five fundamental characteristics of all living systems required to live and thrive (adapted from [2]). To develop bio-mimetic structures, hallmarks such as energy transduction and adaptability need to be embedded within synthetic structures.

Energy transduction is essential for maintaining cellular functions such as metabolism while also allowing living systems to perceive changes in their environment and respond appropriately, supporting adaptability and mobility. One such class of materials that enable such adaptability are mechano-responsive materials, which convert mechanical energy to electrical or chemical energy, and are fundamental for the survival and development of all living systems[3]. Examples of mechano-responsiveness in nature include the ability of plant cells to sense and respond to mechanical stress[4], and the enhanced cell proliferation and osteogenic differentiation of human bone marrow cells upon mechanical vibration[5].

Such sensing and adaptability characteristics provide living systems with the ability to change their actions or behaviour such as adapting bone density based on their local stress, thus using their limited resources in the best possible way. Creating similar functionalities in synthetic structures requires embedding functional materials, such as piezoelectric materials that can create mechano-responsiveness. By integrating these materials, we can develop adaptive systems capable of dynamic responses and autonomous operation inspired by the sophisticated mechanisms found in nature.

1.1.1. SYNTHETIC MECHANO-RESPONSIVE MATERIALS

Piezoelectricity is a phenomenon observed in certain non-centrosymmetric, non-conductive (poly)crystalline materials, where the lack of symmetry within the crystal structure enables the generation of an electric dipole moment when a mechanical force is applied[6]. This provides these materials the ability to convert mechanical energy to electrical energy and vice versa below their Curie temperature (*Tc*), as shown in **Figure 1.2a**.

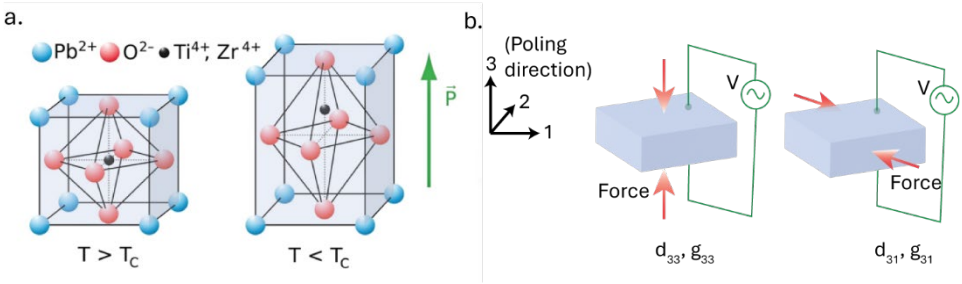

Figure 1.2: Fundamentals of piezoelectricity (a) Non-centrosymmetric crystal structure of piezoelectric materials below their Curie temperature (Tc) leads to a net polarisation, enabling the conversion of mechanical energy to electrical energy and vice versa (adapted from [7]). (b) The direction of the piezoelectric constants is determined by the poling direction, which is always denoted as 3, as well as the orientation of the applied electric field and mechanical force.

This interaction is described by Equation 1[6]:

$$D = d_{ij}T + \epsilon^{T}E \tag{1.1}$$

where D is the electric displacement, d_{ij} is the piezoelectric charge coefficient, T is the mechanical stress, ϵ^{T} is the dielectric permittivity under constant stress and E is the electric field.

Similarly, the figure of merit for sensing which is defined by the output voltage per unit force applied is indicated by the parameter, g_{ij}

$$g_{ij} = \frac{d_{ij}}{\epsilon^T} \tag{1.2}$$

Where (i,j) represent the direction of electric field and deformation, respectively, in Equations 1 and 2, with the poling direction always taken as 3, as shown in **Figure 1.2b**.

A notable subclass of piezoelectric materials is pyroelectric materials, which exhibit spontaneous polarisation even in the absence of an external force. In these materials, a dipole moment exists naturally, and changes in temperature can induce a variation in this polarisation, generating an electric field[6].

Ferroelectrics are a further subset of piezoelectric materials in which the orientation of the spontaneous polarisation can be flipped through a process called poling. While biological materials such bone[8], wood[9], and various fibrous proteins[10] exhibit piezoelectricity, synthetic ferroelectric ceramics such as lead zirconate titanate (PZT) and barium titanate (BT) demonstrate orders of magnitude higher piezoelectric charge coefficient compared to naturally occurring materials[10].

1.1.2. LIVING MECHANO-RESPONSIVE MATERIALS

Though synthetic materials usually have higher properties, living materials are much more energy efficient due to hierarchically complex mechanisms and are typically self-sustaining[11]. Engineered living materials (ELMs) aim to integrate living organisms as active components within natural or synthetic matrices to create bio-hybrid, life-like functionalities such as stimuli-responsiveness in synthetic materials.

Living organisms such as microalgae, which are unicellular photosynthetic microorganisms, respond to mechanical stimuli through changes in growth patterns or metabolic activity. For example, research on ultrasound treatment to increase the biomass and lipid production of *Scenedesmus sp*. showed positive effects[12], indicating that mechanical stimuli can enhance productivity in these organisms.

Similarly, certain species of dinoflagellates, such as the *Noctiluca scintillans* shown in **Figure 1.3a**, which are a group of marine or freshwater eukaryotes, produce bioluminescence as shown in **Figure 1.3b** through the reaction of the

enzyme luciferase and protein-like compound luciferin in the cell's plasma membrane upon mechanical stimulation due to shear stress[13].

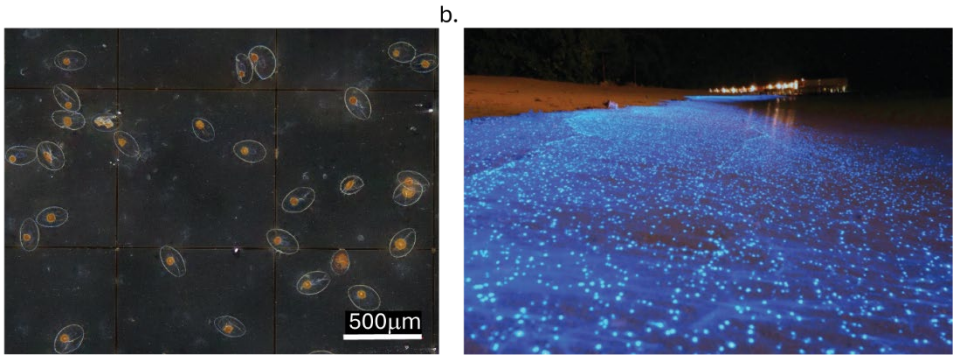

Figure 1.3: Mechano-responsiveness in living cells (a) Dinoflagellates *Noctiluca scintillans* observed under the microscope. (b) Massive bio-luminescent blooms of dinoflagellates in the Arabian Sea observed during December 2017 caused by the thriving of the species *Noctiluca*[14].

These bio-luminescent dinoflagellates are not only robust and self-powering via photosynthesis but also have quick response coupled with high sensitivity when compared to other inorganic mechano-luminescent solids such as $SrAl_2O_4:Eu^{2+}$ and ZnS: Cu^{2+}/Mn^{2+} making the integration of such materials into a bio-hybrid structure a promising alternative to conventional electronic materials paving for new applications in adaptive soft robotics and sensors[15].

1.1.3. MANUFACTURING EMBEDDED MECHANO-RESPONSIVENESS

Whilst capturing these functions into materials is compelling, conventional manufacturing methods for mechano-responsive materials, like piezo-ceramics, rely on Si-wafer-based technologies, leading to rigid and rectangular form factors for sensors and actuators[16]. These methods require the separate production and subsequent assembly of structural and functional components, resulting in bulky electronic assemblies that are hard to integrate into structurally optimised complex geometries.

In contrast, three-dimensional (3D) printing of mechano-responsive materials along with structural materials facilitates embedded sensing and morphing capabilities in energy-efficient structures. An example of such an architected system is the bio-inspired wings of the Airbus concept “Bird of Prey”[17]. This futuristic conceptual airliner, inspired by the efficient mechanics of a bird, features wing and tail structures that mimic those of a bird with individually controlled

feathers for active flight control. To achieve this would require both structural optimisation[18] along with embedded sensors and actuators [19], allowing them to morph in real time, as shown in **Figure 1.4**.

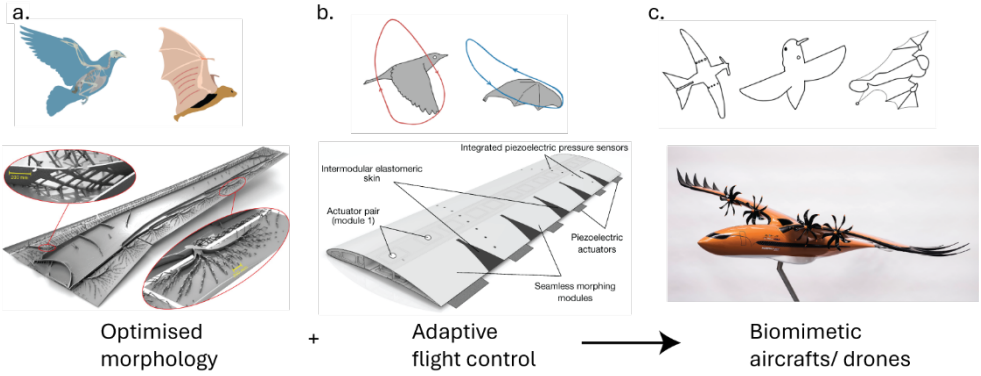

Figure 1.4: Combining both morphological and behavioural solutions from nature can help design energy efficient structures. (a) Wing design by optimizing material distribution at giga-voxel resolution computation results in intricate structures resembling natural bone architecture. (b) Integrated piezoelectric sensors in SmartX wing to detect laminar to turbulent flow transition and enable seamless shape morphing. (c) Future aircraft designs such as Airbus- 'Bird of Prey' showing biomimetic wing design with active flight control (adapted from [12]-[14]).

There is limited research on 3D printing mechano-responsive materials that can be directly integrated into structures to create life-like or responsive synthetic and living materials. This represents a significant opportunity for further exploration and innovation. One such 3D process that has gained great attention is direct ink writing.

1.2. DIRECT INK WRITING

Direct ink writing is a versatile 3D printing technique for multi-material fabrication, offering straightforward and quick printing of a wide range of materials at room temperature. The process involves the extrusion of a viscoelastic ink from a syringe, depositing it layer by layer onto a substrate.

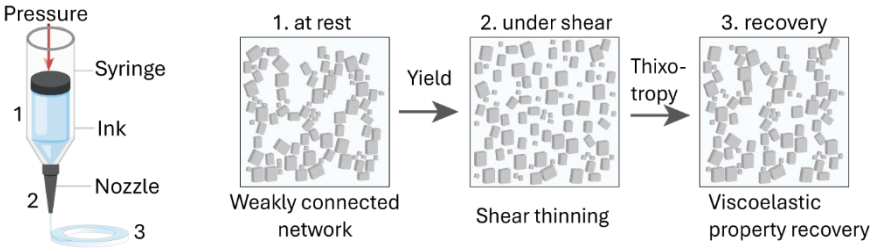

Figure 1.5: Schematic of the direct ink writing process. The material, ideally a weakly flocculated colloidal system with a volume fraction above the gel point (1), undergoes shear thinning behaviour (2) while being extruded through a nozzle by applying pressure and reforms upon the removal of shear forces after printing (3).

Since DIW uses materials that undergo viscoelastic transition on the application of shear forces, as shown in **Figure 1.5**, careful control of its rheological properties is key to achieving sufficient shaping freedom.

Typically, they consist of a weakly interconnected colloidal network that can enable a controlled viscoelastic response and have a sufficiently high shear yield point (τ_y) to not flow out while stored in the syringe. Then, the inks experience shear-induced breakdown while being extruded, initiating flow from the nozzle and exhibiting shear thinning behaviour as described by the Herschel-Bulkley model[20],

$$\tau = \tau_y + K\dot{\gamma}^n \tag{1.3}$$

where τ is the shear stress, n is the shear thinning exponent (< 1), K is the viscosity parameter, and $\dot{\gamma}$ is the shear rate. The shear rate, $\dot{\gamma}$ is influenced by volume flow rate and nozzle diameter, and the viscosity of the ink must be tuned to match printer specifications. The inks must quickly recover their elastic properties after the removal of shear stress to maintain the shape of printed filaments. The dynamic yield stress of the recovered ink (σ_y) must be high enough to prevent distortion from gravity and capillary pressure and is determined from Equation 4[21].

$$\Xi = \frac{\sigma_y}{\gamma R^{-1} + \rho g h} \tag{1.4}$$

The dimensionless number, Ξ, must be greater than or equal to 1 for the material to counter these forces, where γ is surface tension, R is nozzle diameter, ρ is density, h is the height of the printed object, and σ_y is dynamic yield stress.

For slip-based extrusion, the materials print almost independently of their yield stress. Highly concentrated particle pastes often exhibit desirable slip behaviour[22,23].

By understanding and optimising these extrusion properties, DIW can be effectively utilised to create complex, multi-material structures with embedded functionality.

1.3. STATE OF THE ART ON DIW OF MECHANO-RESPONSIVE MATERIALS

This section provides a comprehensive review of the current state of direct ink writing of mechanoresponsive materials, focusing particularly on piezoelectric materials and living organisms such as bacteria, fungi, algae and dinoflagellates.

1.3.1. DIW OF PIEZOELECTRIC MATERIALS

DIW of near-net-shaped piezoelectric ceramics involves the use of colloidal gels followed by high-temperature sintering (around 1000 °C). Smay et al.[24] were among the early researchers to utilise directed deposition of PZT colloidal gels to fabricate linear (**Figure 1.6a**) and annular (**Figure 1.6b**) PZT arrays. The printed shapes were dried, sintered, and then infiltrated with a polymer phase into the PZT skeletal structure, achieving a d_{33} of approximately 500 $pC \cdot N^{-1}$. More recently, Li et al.[25] developed a combined process of DIW and secondary shaping of a flexible ceramic green body, producing curved piezoelectric ceramics as shown in **Figure 1.6c** and **1.6d** with an average d_{33} of 265 $pC \cdot N^{-1}$. However, the requirement for high-temperature sintering presents challenges in integration despite the method's capability to produce intricate ceramic components. Additionally, EU regulations on the restriction of lead usage in electronic components due to its bio-toxicity have prompted the search for alternatives to PZT despite its promising performance[26].

To address this, piezoelectric polymers such as PVDF and its co-polymers have been studied for DIW. Kim et al.[27] explored the possibility of printing PVDF with Barium Titanate dispersed in it to increase the β-phase content, though the d_{33} was observed to be two orders of magnitude lower than commercial films. Bodhke et al.[28] developed a solvent-evaporation assisted DIW of piezoelectric PVDF nanocomposite, achieving a ~22% increase in the β-phase over unfilled PVDF and a maximum $d_{33}$of 18 $pC \cdot N^{-1}$with 10 wt.% BT nanoparticle loading as shown in **Figure 1.6e**.

Similarly, Ikei et al.[29] showed the ability to 3D printing and poling of PVDF-TrFE with a d_{33} of up to 18 $pC \cdot N^{-1}$, as shown in **Figure 1.6f,** utilising the ability of the -TrFE monomer to impede the formation of the α phase through steric hindrance, leading to an increase in the β phase of the PVDF-TrFE copolymer. Yan et al.[30] further improved the properties of printed PVDF-TrFE by adding 15 wt.% of electro-spun nanowires of the lead-free $Ba_{0.85}Ca_{0.15}Ti_{0.9}Zr_{0.1}O_3$ (BCZT) to the PVDF-TrFE polymers in solution and then DIW to make flexible sensor films as shown in **Figure 1.6g**.

However, most of these PVDF-based printing methods use large volume fractions of solvent, leading to significant shrinkage of the structures post-printing. This gives limitations both on the mechanical properties and the shaping ability, leading to the shapes being relatively planar, as seen in **Figure 1.6 f** and **g**. Further, though PVDF and its co-polymers have higher g_{33} values compared to ceramics and offer high flexibility, their low thermal stability, poor adherence to substrates, and lower mechanical properties limit their use as integrated actuators.

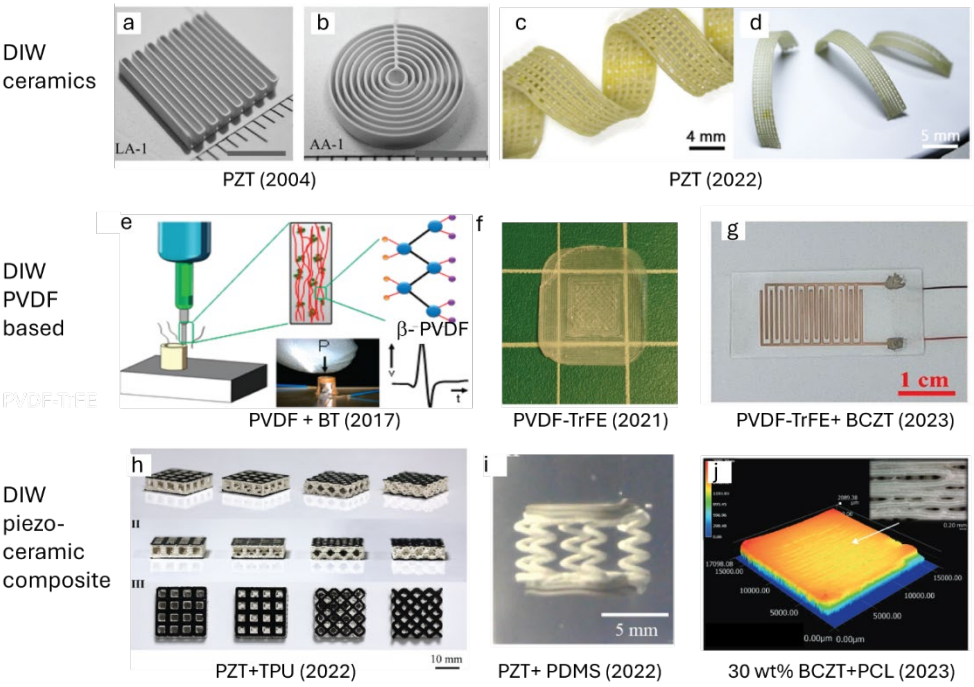

Figure 1.6: State of the art for DIW of piezoelectric materials. (a) and (b) Sintered linear and annular PZT arrays made from DIW of PZT colloidal gels[24]. (c) and (d) PZT ceramics shaped by DIW, followed by twisting and reshaping of the flexible green ceramic and then sintering to achieve complex unsupported ceramic structures[25]. (e) 10 wt.% $BaTiO_3$ nanoparticles dispersed in PVDF, 3D printed via a one-step solvent evaporation and in-situ poling-assisted DIW method to create readily integrable sensors[28]. (f) Fused filament deposition of PVDF-TrFE coupled with in-situ poling[29]. (g) BCZT nanowire filled PVDF-TrFE films manufactured via DIW and drying leading to flexible sensors[30]. (h) 30 vol% PZT particles dispersed in flexible TPU and printed via FFF[31]. (i) 30 vol% PZT particles mixed with PDMS printed inside a gel to allow free-form shapes without requiring support structures with application as flexible sensors[32]. (j) 30wt% BCZT in PCL composites 3D printed via DIW showing promise as antibacterial surfaces[33].

Piezo ceramic-polymer composites, consisting of an active piezo-ceramic filler within a passive polymer matrix, were first developed by Kitayama and Sugawara in

1972[34]. These composites offer a favourable combination of good piezoelectric properties, high-temperature stability, low poling voltages, and adaptability for various applications. Current research on DIW of piezo composites includes work by Tao et al.[31] on DIW of TPU with 30 vol% PZT as shown in **Figure 1.6h**, showing potential for lightweight sensors and energy harvesters. Tao et al.[32] also demonstrated DIW of polydimethylsiloxane (PDMS) with 30 vol% PZT, achieving a d_{33} of 6.3 $pC \cdot N^{-1}$, allowing for conformal (non-planar) and freeform 3D printing as shown in **Figure 1.6i**. In the realm of lead-free piezoelectric ceramic-based composites, Tsikriteas et al.[33] utilised a solvent-free DIW process to print 30 wt.% of BCZT with PCL, as shown in **Figure 1.6j**, achieving a d_{33} value of 1.2 $pC \cdot N^{-1}$and demonstrating potential for antimicrobial surfaces.

Though these are promising directions for developing DIW piezoelectric materials, current research still lacks materials that have simultaneously, both high piezo performance combined with the ability to be easily integrated with other materials, while ensuring shaping freedom.

1.3.2. DIW OF LIVING MATERIALS

Recent advancements in direct ink writing of engineered living materials (ELMs) have focused on the integration of living cells that have been selected or programmed for specific functionalities into hydrogels to create biohybrid functional living structures. Schaffner et al.[35] studied the multi-material 3D printing of hydrogels with P. *putida* and *B. subtilis* to create functional living inks that are capable of degrading pollutants and producing bacterial cellulose, as shown in **Figure 1.7a**. Similarly, Liu et al.[36] employed genetically programmed *E. coli* cells in hydrogel to create structures, as shown in **Figure 1.7b,** such that the cells can communicate and process signals, enabling novel applications such as logic gates and wearable devices using 3D printed cells. Duraj-Thatte et al.[37] went one step further by completely developing the 3D printable ink from genetically engineered E. coli, which formed nanofiber networks in the standard bacteria culture, enabling the desired viscoelastic response to create a 3D printable ink. Printed structures from this microbial ink are shown in **Figure 1.7c.** Additionally, research has focused on creating robust and sustainable living materials. Gantenbein et al.[38] utilised hydrogels loaded with *Ganoderma lucidum* to print structures that promote mycelial growth, as shown in **Figure 1.7d**, showing potential application in mechanically robust, hydrophobic and self-healing robotic skins.

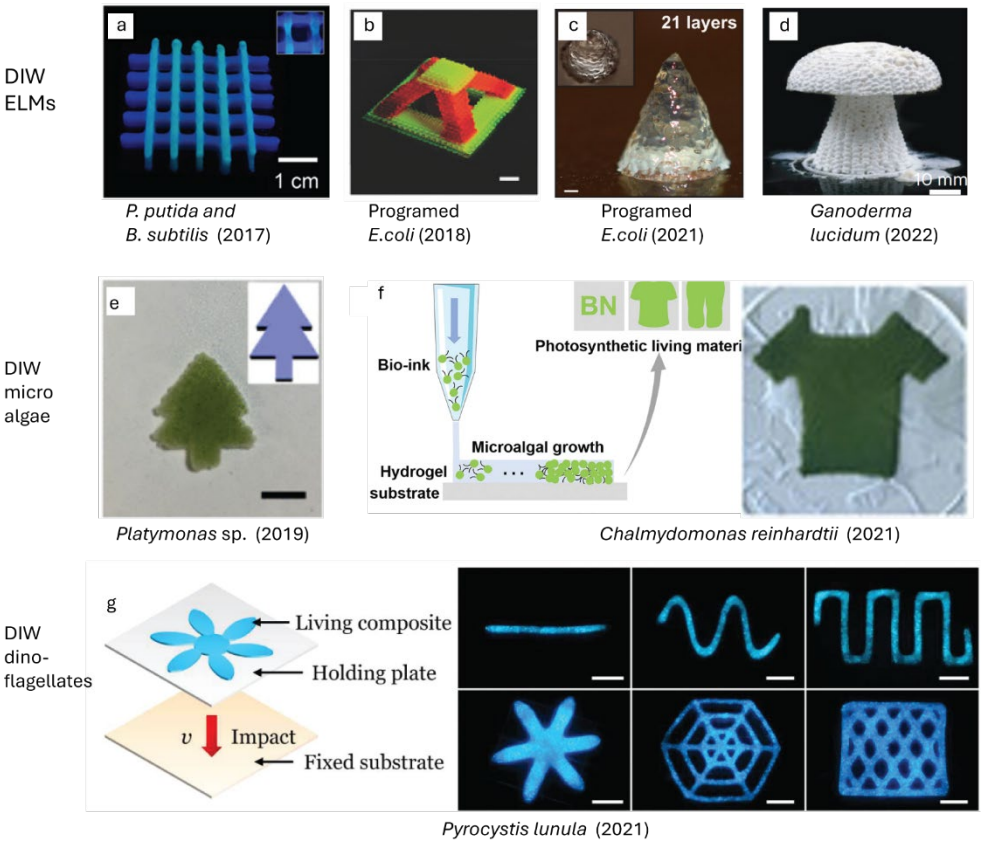

Figure 1.7: State of the art for DIW of engineered living materials (ELMs). (a) 3D printed structures with two bacterial inks, the horizontal lines with the blue label containing *P. putilda*, and the vertical lines with the green label containing *B. subtilis*[35]. (b) Pyramid-shaped printed structures after UV crosslinking of Pluronic F127-DA hydrogel ink that are used as a biocompatible matrix for the programmed bacteria E. coli [36]. (c) Cone-shaped structure printed from the ink generated entirely by programmed E. coli showing sufficient viscoelastic response to be able to be printed into a 21-layer, 3D structure[37]. (d) *Ganoderma lucidum*-laden hydrogels, which were 3D printed separately as the top and base of a mushroom structure, subsequently joined into a single cohesive object due to the growth of mycelium hyphal network upon surface contact[38]. (e) Silk-based crosslinked hydrogel used to create a four-layer, tree-shaped structure with embedded *Platymonas* sp microalgae[39].(f) Multilayered structures of alginates-based hydrogels with embedded *Chlamydomonas reinhardtii* microalgae, printed on sheets of bacterial cellulose (Adapted from [40]). (g) 3D printed structures containing *P.lunula* emitting blue light upon mechanical impact[41].

Recently, there has been an increased interest in the bio-printing of microalgae due to their adaptability to harsh conditions, robustness, and sustainability. Zhao et al.[39] developed silk protein-based hydrogels hosting living microalgae, optimised for long-term cell viability and photosynthetic activity, suggesting applications in environmental sustainability. Balasubramanian et al.[40] demonstrated a bioprinting technique that encapsulated microalgae in alginate hydrogels and printed them

onto a bacterial cellulose substrate to produce planar structures with high mechanical resilience, suitable for applications like artificial leaves and bio-garments.

Such advancements in 3D printing of living algae-based inks have been used to develop DIW of living mechano-responsive materials. Li et al. developed robust mechanoluminescent living composites using alginate-based hydrogels embedded with marine dinoflagellates. These hydrogels, once crosslinked, exhibited a near-instantaneous and ultrasensitive bioluminescent response to mechanical stress. The hydrogels with dinoflagellates also demonstrated high viability, and with hydrophobic coatings, the living composites had a lifetime of approximately five months under harsh conditions with minimal maintenance. Additionally, they showed the use of these mechano-sensing composites for biomimetic soft actuators that emitted coloured light upon magnetic actuation. These studies collectively highlight the potential of 3D printing to create complex, functional living materials with applications ranging from environmental sustainability to mechanosensitive materials[36].

1.4. SCOPE AND OUTLINE OF THESIS

The goal of this thesis is to 3D print mechanoresponsive materials while retaining the ease of integrating these materials with structural components to achieve active complex shapes. The thesis is divided into two parts: the first part focuses on Direct Ink Writing (DIW) of synthetic mechanoresponsive materials, such as piezoelectric composites and the second part examines DIW of living mechanoresponsive materials, such as microalgae and dinoflagellate cells.

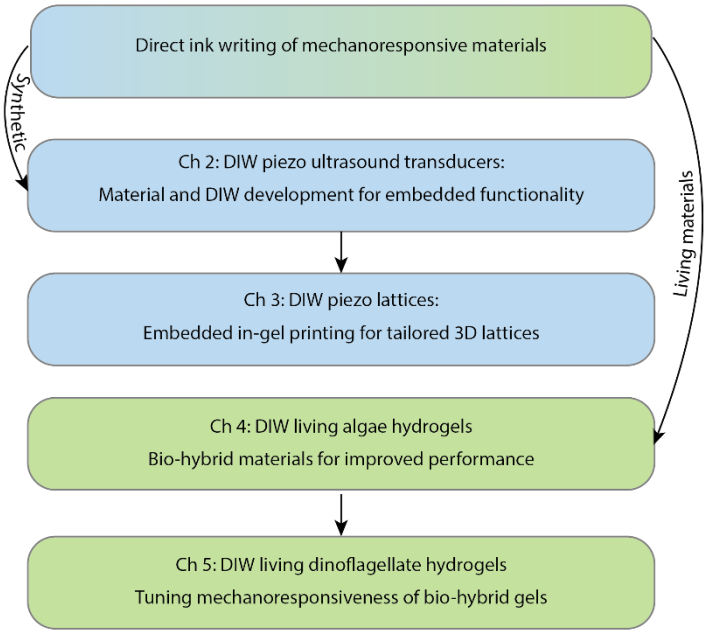

Figure 1.8: Schematic overview of the thesis, highlighting the focus on DIW mechano-responsive materials and the interconnections between chapters.

Chapter 2: focuses on the direct ink writing of UV-curable, lead-free KNLN-based piezo ceramic-polymer composites to create ultrasound transducers. The performance of the ink for printing and its piezoelectric properties are studied. Design simulations in COMSOL are used to investigate the effect of transducer dimensions on out-of-plane displacement. The manufactured transducers are tested via laser Doppler Vibrometry, and their sound pressure is measured. Finally, an application in distance measurement is demonstrated.

Chapter 3: investigates the DIW of KNLN-based composites embedded within a gel matrix. Lattice structures are designed to achieve properties not available in bulk materials A manufacturing method to produce such lattices with high piezoelectric ceramic content is developed by developing an embedded DIW system for UV-

curable piezo-composites. Matrix rheology is optimized, and printing parameters such as speed and viscosity are studied to achieve the manufacturing of the modelled lattices. The piezoelectric properties in orthogonal directions are measured and compared to theoretical predictions.

Chapter 4: By embedding microalgae in hydrogels, we create structures capable of absorbing CO_2 and photosynthesizing. The formulation of the gel to support the microalgae, along with its ability to be printed and cross-linked via $CaCl_2$-mediated ionic cross-linking, is studied. The growth distribution and photosynthetic activity of the microalgae within the hydrogels are analysed, and the effect of shaping on their functionality is examined.

Chapter 5: focuses on developing mechano-responsive living materials by embedding dinoflagellate cells into hydrogels. Building on the insights from Chapter 4 on direct ink writing (DIW) of algae, the study optimizes ink formulations to incorporate dinoflagellates, tuning the material's mechanical properties to induce bioluminescence. This work examines the trade-offs between material composition, printability, and functional performance, to understand the potential to produce living materials with responsive, light-emitting properties.

Chapter 6: This chapter concludes and summarizes the findings of the thesis, highlighting the key contributions and implications for future research and applications in the field of 3D-printed mechanoresponsive materials.

1.5. REFERENCES:

[1] "Summary for Policymakers of IPCC Special Report on Global Warming of 1.5°C approved by governments — IPCC.", **2018**, Available: https://www.ipcc.ch/2018/10/08/summary-for-policymakers-of-ipcc-special-report-on-global-warming-of-1-5c-approved-by-governments/.

[2] N. A. Yewdall, A. F. Mason, J. C. M. van Hest, *Interface Focus* **2018**, *8*, 20180023.

[3] A. W. Orr, B. P. Helmke, B. R. Blackman, M. A. Schwartz, *Dev. Cell* **2006**, *10*, 11.

[4] O. Hamant, M. G. Heisler, H. Jönsson, P. Krupinski, M. Uyttewaal, P. Bokov, F. Corson, P. Sahlin, A. Boudaoud, E. M. Meyerowitz, Y. Couder, J. Traas, *Science* **2008**, *322*, 1650.

[5] S. Camarero-Espinosa, L. Moroni, *Nat. Commun.* **2021**, *12*, 1.

[6] J. Holterman, W. Groen, *An Introduction to Piezoelectric Materials and Applications*, Stichting Applied Piezo, Apeldoorn, **2013**.

[7] A. H. Meitzler, D. Berlincourt, G. A. Coquin, H. F. Tiersten, F. S. Welsh III, A. W. Warner, *IEEE Standard on Piezoelectricity ANSI/IEEE Std 176*, The Institute of Electrical and Electronics Engineers, Inc, New York, New York, **1987**.

[8] E. Fukada, I. Yasuda, *J. Phys. Soc. Jpn.* **1957**, *12*, 1158.

[9] E. Fukada, *Wood Sci. Technol.* **1968**, *2*, 299.

[10] S. Guerin, S. A. M. Tofail, D. Thompson, *NPG Asia Mater.* **2019**, *11*, 1.

[11] W. Wagermaier, K. Razghandi, P. Fratzl, *Adv. Mater.* **n.d.**, *n/a*, 2413096.

[12] R. Sivaramakrishnan, A. Incharoensakdi, *Biocatal. Agric. Biotechnol.* **2019**, *20*, 101230.

[13] M. Valiadi, D. Iglesias-Rodriguez, *Microorganisms* **2013**, *1*, 3.

[14] "Studying Bioluminescent Blooms in the Arabian Sea | Lamont-Doherty Earth Observatory," **2017**, Available: https://lamont.columbia.edu/news/studying-bioluminescent-blooms-arabian-sea.

[15] C. Li, Q. He, Y. Wang, Z. Wang, Z. Wang, R. Annapooranan, M. I. Latz, S. Cai, *Nat. Commun.* **2022**, *13*, 3914.

[16] G.-L. Luo, Y. Kusano, D. A. Horsley, *J. Microelectromechanical Syst.* **2021**, *30*, 81.

[17] "An Airbus futuristic conceptual airliner 'takes flight' to inspire next-generation engineers - Innovation - Airbus.", **2019**, Available: https://www.airbus.com/newsroom/news/en/2019/07/airbus-conceptual-airliner-to-inspire-new-generation-engineers.html.

[18] N. Aage, E. Andreassen, B. S. Lazarov, O. Sigmund, *Nature* **2017**, *550*, 84.

[19] V. L. Stuber, T. Mkhoyan, R. De Breuker, S. van der Zwaag, *Meas. Sens.* **2022**, *19*, 100356.

[20] J. A. Lewis, *Adv. Funct. Mater.* **2006**, *16*, 2193.

[21] A. M'Barki, L. Bocquet, A. Stevenson, *Sci. Rep.* **2017**, *7*, 1.

[22] U. Yilmazer, D. M. Kalyon, *J. Rheol.* **1989**, *33*, 1197.
[23] J. E. Smay, G. M. Gratson, R. F. Shepherd, J. Cesarano, J. A. Lewis, *Adv. Mater.* **2002**, *14*, 1279.
[24] J. E. Smay, J. Cesarano, B. A. Tuttle, J. A. Lewis, *J. Am. Ceram. Soc.* **2004**, *87*, 293.
[25] Z. Li, J. Li, H. Luo, X. Yuan, X. Wang, H. Xiong, D. Zhang, *J. Eur. Ceram. Soc.* **2022**, *42*, 3841.
[26] European Chemical Agency, *Support Document for Identification of Lead (Lead Powder and Lead Massive) as a Substance of Very High Concern Because of Its Toxic for Reproduction Properties*, European Chemical Agency, **2018**.
[27] H. Kim, F. Torres, D. Villagran, C. Stewart, Y. Lin, T.-L. B. Tseng, *Macromol. Mater. Eng.* **2017**, *302*, 1700229.
[28] S. Bodkhe, G. Turcot, F. P. Gosselin, D. Therriault, *ACS Appl. Mater. Interfaces* **2017**, *9*, 20833.
[29] A. Ikei, J. Wissman, K. Sampath, G. Yesner, S. N. Qadri, **2021**, 1.
[30] M. Yan, H. Li, S. Liu, Z. Xiao, X. Yuan, D. Zhai, K. Zhou, C. R. Bowen, Y. Zhang, D. Zhang, *ACS Appl. Polym. Mater.* **2023**, *5*, 4879.
[31] R. Tao, J. Shi, F. Granier, M. Moeini, A. Akbarzadeh, D. Therriault, *Appl. Mater. Today* **2022**, *29*, 101596.
[32] R. Tao, F. Granier, D. Therriault, *Addit. Manuf.* **2022**, *60*, 103243.
[33] Z. M. Tsikriteas, R. A. Heylen, S. Jindal, E. Mancuso, Z. Li, H. Khanbareh, *Adv. Mater. Technol.* **2023**, *8*, 2202127.
[34] K. Uchino, in *Adv. Piezoelectric Mater. Second Ed.* (Ed.: K. Uchino), Woodhead Publishing, **2017**, pp. 1–92.
[35] M. Schaffner, P. A. Rühs, F. Coulter, S. Kilcher, A. R. Studart, *Sci. Adv.* **2017**, *3*, eaao6804.
[36] X. Liu, H. Yuk, S. Lin, G. A. Parada, T.-C. Tang, E. Tham, C. de la Fuente-Nunez, T. K. Lu, X. Zhao, *Adv. Mater.* **2018**, *30*, 1704821.
[37] A. M. Duraj-Thatte, A. Manjula-Basavanna, J. Rutledge, J. Xia, S. Hassan, A. Sourlis, A. G. Rubio, A. Lesha, M. Zenkl, A. Kan, D. A. Weitz, Y. S. Zhang, N. S. Joshi, *Nat. Commun.* **2021**, *12*, 6600.
[38] S. Gantenbein, E. Colucci, J. Käch, E. Trachsel, F. B. Coulter, P. A. Rühs, K. Masania, A. R. Studart, *Nat. Mater. 2022 221* **2022**, *22*, 128.
[39] S. Zhao, C. Guo, A. Kumarasena, F. G. Omenetto, D. L. Kaplan, *ACS Biomater. Sci. Eng.* **2019**, *5*, 4808.
[40] S. Balasubramanian, K. Yu, A. S. Meyer, E. Karana, M.-E. Aubin-Tam, *Adv. Funct. Mater.* **2021**, *31*, 2011162.
[41] C. Li, N. Schramma, Z. Wang, N. F. Qari, M. Jalaal, M. I. Latz, S. Cai, *Sci. Adv.* **2023**, *9*, eadi8643.

2

THREE-DIMENSIONAL PRINTING OF LEAD-FREE PIEZOELECTRIC ULTRASOUND TRANSDUCERS

*Multi-material direct ink writing (DIW) combined with smart materials allows the 3D printing of functional and structural materials together, opening new possibilities for manufacturing complex structures with embedded sensing and actuation capabilities. In this study, DIW of UV-curable piezoelectric actuators is developed, which, in contrast to earlier work, do not require high-temperature sintering post-printing, allowing direct integration with structural materials. Through particle size and ink rheology optimization, the highest d_{33}*g_{33} piezoelectric constant compared to other DIW fabricated piezo composites is achieved, enabling tuneable actuation performance without the need for sintering post-printing. This is used to fabricate ultrasound transducers by printing piezoelectric vibrating membranes along with their support structures made from a structural ink. Furthermore, the impact of transducer design and scaling up transducer dimensions on the resonance behaviour to design millimetre-scale ultrasound transducers with desired out-of-plane displacement is explored. A significant increase in output pressure with increasing membrane dimensions is observed. Finally, we demonstrated a practical application by using the printed transducer for accurate proximity sensing using time of flight measurements. The scalability and flexibility of the reported DIW of piezo composites can open new advancements in biomedical, human-computer interaction, and aerospace fields.*

This chapter has been published as S. K. Ammu, X. Chen, D. G. Ulcay, S. Sharma, F. Alijani, P. G. Steeneken, P. Groen, K. Masania, “3D Printing of Lead-Free Piezoelectric Ultrasound Transducers”. Adv. Mater. Technol. 2024, 2400858.

2.1. INTRODUCTION

Due to their accuracy, fast response, and energy efficiency, piezoelectric ultrasound transducers find extensive applications in haptic devices[1], gesture detection[2], and time-of-flight sensors[3]. Despite their broad potential, such devices made from silicon-based microfabrication techniques[4] remain bulky and planar, posing challenges for seamless integration into complex structures. The emergence of multi-material 3D printing[5] and functional materials offers new possibilities for the development of intelligent structures with embedded sensing and actuation capabilities[6].

Among these technologies, direct ink writing (DIW) stands out for its ability to combine structural and sensing materials within the same printed object through ink design. DIW has been successfully used in fabricating soft electronics[7] and embedded sensors[8]. Currently, research on 3D-printed ultrasound transducers primarily focuses on piezoelectric ceramics that require high-temperature sintering[9,10]. Previous studies have demonstrated excellent piezoelectric properties of d_{33} from 388 to 496 $pC \cdot N^{-1}$ achieved through DIW of piezoelectric ceramic-based transducers[11]. Nonetheless, the need for high temperature sintering typically above 1000 °C, to densify the ceramic introduces risks of cracks and high porosity in the 3D printed parts and limits their direct integration with other structural materials.

To address this high-temperature processing step, direct printing methods such as solvent evaporation-assisted 3D printing of piezoelectric PVDF nanocomposites, allow for the creation of transducers that offer improved integration into structures[12]. However, this relies on printing using considerable amounts of solvents, which can lead to increased porosity. Although porosity can benefit sensing applications, it poses challenges for actuation applications due to lower mechanical stiffness[12], reduced block force, electrostatic breakdown and poor electro-mechanical coupling efficiency. Further, PVDF and its co-polymers have poor temperature stability compared to piezo-ceramics and poor adhesion to other substrates, making integration into structures challenging.

Piezo ceramic-polymer composites are a promising alternative as they offer a favourable combination of good piezoelectric properties, high-temperature stability, low poling voltages, and the conformability and versatility of the polymeric continuous phase[13]. The piezoelectric properties of these composites are highly dependent on the volume fraction of the piezoelectric particles, with higher fractions leading to enhanced electro-mechanical coupling factors[14]. Despite the

potential demonstrated by DIW of piezoelectric composites, current solutions are constrained by low volume fractions to mitigate nozzle clogging, limiting maximum piezoelectric performance to voltage generation for sensing or energy harvesting applications[15,16].

Consequently, there is a need for a 3D printable piezo-composite system that can offer a combination of high piezoelectric response and seamless integration into structures. Here, we develop a method for direct ink writing of ultrasound transducers using a lead-free, 3% Li-substituted sodium potassium niobate $K_{0.485}Na_{0.485}Li_{0.03}NbO_3$ (KNLN), in combination with UV curable monomers. Potassium sodium niobate (KNN) has shown promise in terms of their piezoelectric properties[17], biocompatibility[18] and have been demonstrated successfully to outperform both bulk PZT and most composites in sensing and energy harvesting applications[19,20]. To ensure both shaping freedom and piezoelectric performance, we propose to split these functions. Using a multi-material 3D printing technique, we print a UV-curable piezoelectric vibrating membrane along with a support structure using a structural ink. This method enables the printing and UV curing of piezoelectric ultrasound transducers without additional high temperature sintering post-processes. By optimising the composite properties, we can attain high piezoelectric properties while ensuring a robust bonding between the piezo materials and other structural materials. We perform finite element simulations to establish the design principles of these transducers and subsequently investigate their acoustic pressure generation and application in distance measurement. Our approach with DIW piezoceramic-polymer composites allows for the creation of ultrasound transducers with millimetre-scale dimensions using commercial 3D printers while providing flexibility in tailoring the transducer's mechano-acoustic properties such as freely tuneable operating frequencies. This scalability and flexibility can benefit a wide array of applications in biomedical, structural, robotic interfaces and energy fields.

2.2. RESULTS AND DISCUSSION

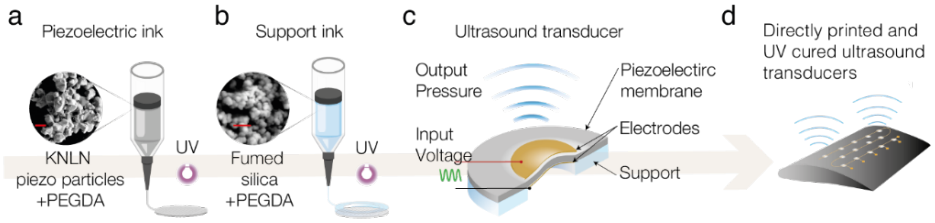

Figure 2.1. Direct ink writing (DIW) of UV-curable piezoelectric ultrasound transducers. (a) DIW process for printing the piezoelectric membrane using a KNLN microparticle-based ink, followed by UV curing. The inset shows the scanning electron microscope (SEM) image of the KNLN particles (red scale bar, 2 µm). (b) Printing of the support structure that clamps the piezoelectric membrane using a support ink containing fumed silica mixed with UV-curable PEGDA. The inset shows the SEM image of the fumed silica particles (scale bar, 200 nm). (c) Cross-sectional representation of the ultrasound transducer, along with top and bottom electrodes. Schematic demonstrates the working principle, indicating the input AC voltage and the resulting ultrasound pressure due to the output vibration of the piezoelectric membrane. (d) Directly printed and UV-cured ultrasound transducers enabling the creation of intelligent structures with embedded transducers.

Our approach to directly printed ultrasound transducers combines the 3D printing of a UV curable piezoelectric-composite ink that is optimised for its piezoelectric performance, along with a structural ink used for printing the clamping support for the piezoelectric membrane. The DIW process used to fabricate piezoelectric ultrasound transducers is shown in **Figure 2.1**. The piezoelectric ink consists of synthesised KNLN micro-particles (**Figure S2.1a**) that are dispersed in a UV-curable monomer, poly-(ethylene glycol) diacrylate, PEGDA-250 (**Figure S2.1b**).

The ink's piezoelectric and rheological properties are optimised for actuation while ensuring compatibility with DIW and co-curing with structural materials. First, the piezoelectric membrane is fabricated through a layer-by-layer extrusion process of the piezo ink, followed by sequential UV curing of each layer. This sequential curing ensures adequate UV penetration and curing in the piezo layers, resulting in structural integrity.

Next, a structural ink comprising UV-curable PEGDA-250 with fumed silica is used to print the membrane's supporting structure (**Figure 2.1b**), enabling radial clamping of the membrane and facilitating out-of-plane vibration. The resulting transducer is inverted after printing. Top and bottom electrodes are then integrated on to the transducer either by gold sputtering or by painting using a conductive carbon paste. This is followed by a poling process to align the piezoelectric domains within the material, as explained in the Experimental Section. **Figure 2.1c** illustrates

the functioning of the poled transducer, depicting the application of input voltage and the resultant ultrasound pressure generated from the output vibration. This allows for directly printed and UV-cured ultrasound transducers, allowing functional material integration into structures which is conceptualised in **Figure 2.1d**.

2.2.1. OPTIMISATION OF PRINTING AND FUNCTIONAL PROPERTIES OF PIEZO AND STRUCTURAL INKS

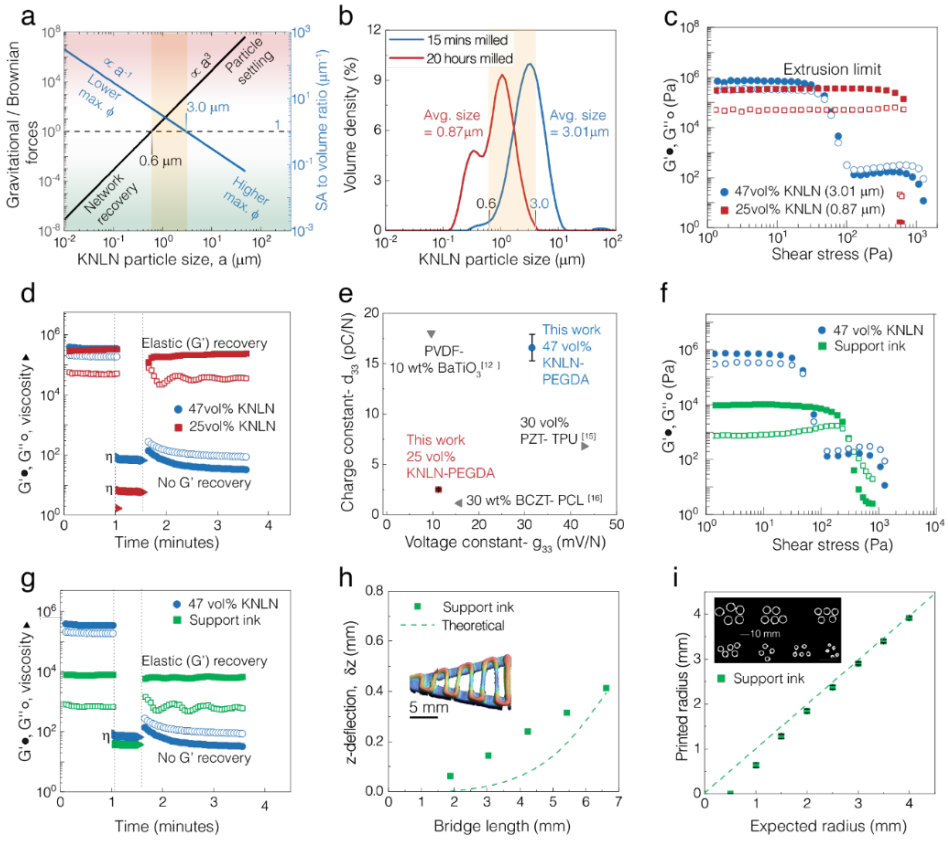

Figure 2.2. Printing and functional properties of the DIW inks for printable ceramic-polymer transducers. (a) Effect of particle size {*a*} on the ratio of gravitational to Brownian forces (black line) vs ratio of surface area to volume (blue line) and their impact on physical phenomena relevant to printing and piezoelectric properties. The highlighted area between 0.6 μm and 3.0 μm denotes the region of interest in particle size where a trade-off occurs between those above two competing effects. (b) As highlighted, the particle size analysis of the synthesised KNLN powder under different milling conditions resulted in two distinct median particle size distributions close to the calculated critical particle size. (c) Impact of particle size on maximum storage and loss moduli (G' and G") and the resultant maximum extrudable volume fraction of the ink for varying particle sizes. (d) Evaluation of the elastic recovery behaviour of the ink after shear tested via oscillation-rotation-oscillation test showing rapid elastic recovery for small particles and no recovery for the larger particles. (e) Piezoelectric properties of ink containing larger particles and a higher volume fraction (47 vol%) surpass state-of-the-art extrusion-based sintering-free piezo-composites. (f) Oscillatory shear sweep of support ink created for printing the support structures. (g) The recovery test of the support ink shows quick elastic recovery compared to the piezo ink. (h) Bridging test evaluating the sagging behaviour with the length of the bridging element for the support ink. The inset shows the optical microscope image of the bridging test. (i) Assessment of dimensional accuracy of the diameters of the support structure, exhibiting close agreement with theoretical values and high repeatability above 1 mm as indicated by the low standard deviation (n=5). The inset shows the image of the printed support structures with varying diameters.

We first study the printing and electro-mechanical properties of the piezoelectric ink and the supporting ink followed by the design of the ultrasound transducers using these inks. The piezoelectric properties of particle-based piezo composites are significantly influenced by the volume fraction of the filler, with a higher fraction leading to higher piezoelectric constants and better electro-mechanical coupling factors[14]. To ensure efficient functioning in both actuation and sensing applications, it is crucial to maximise the volume fraction of the piezoelectric particles in the ink while maintaining compatibility with DIW process. Therefore, we investigated the influence of KNLN particle size on the maximum volume fraction and resulting printing properties and piezoelectric coefficients of the ink when used in DIW. Since the direct ink writing setup uses rheologically engineered inks that undergo a reversible viscoelastic transition in response to shear forces, one of the critical factors to consider is the influence of particle size on the ability of the ink to undergo an elastic to viscous transition on the application of shear and then recover to a weakly flocculated elastic structure on the removal of shear forces. This elastic recovery is governed by the Brownian forces that randomise the particles suspended in the ink and create a weakly interconnected network, thus allowing the ink to support its weight and subsequent layers against gravity and capillary forces, ultimately leading to freestanding 3D shapes.

The ratio of gravitational to Brownian forces is proportional to:[21]

$$Grav/Brownian \propto \frac{a^4 \Delta\rho g}{k_B T} \tag{2.1}$$

where a is the radius of the particle or clump of particles,

$\Delta\rho$ is the difference in density between the particle and the liquid medium,

g= 9.8 m·s^{-2} is the acceleration due to gravity,

k_B=1.38×10^{-23} J·K^{-1} is the Boltzmann constant and,

T= Temperature in K

Based on this equation, inks containing larger particles experience increased sedimentation and phase separation due to the power law growth in gravitational forces with particle size ($\propto a^3$) compared to the Brownian forces that randomise the particles, as depicted in **Figure 2.2a** (black line). From **Equation 2.1**, we calculated the critical size for KNLN particles to undergo sedimentation in the PEGDA medium to be 0.6 µm (SI- **Table S2.1**). Well-distributed particles smaller than 0.6 µm are

preferable for direct ink writing as they quickly recover their randomised network structure after printing, enabling good shape retention and the creation of complex geometries.

Conversely, smaller, sub-micron particles exhibit significantly greater surface area relative to their volume ($\propto a^{-1}$), as illustrated by the surface area to volume ratio in **Figure 2.2a** (blue line). The increase in surface area results in higher inter-particle interactions and faster network jamming, thus increasing viscosity and limiting the maximum volume fraction. Therefore, we hypothesise that depending on the particle size used in the composite, a trade-off emerges between printability governed by the ink recovery and the piezoelectric properties determined by the maximum printable volume fraction, and this trade-off needs to be optimised particularly in applications which demand high electro-mechanical performance.

To further explore this trade-off in the KNLN-PEGDA system and determine the dominant parameter, two sets of KNLN particles with sizes approximating these critical values were synthesised with varying milling durations, as shown in **Figure 2.2b**. We synthesised KNLN particles using a two-step solid-state reaction further described in the Materials and Methods section, followed by either a 15-minute ball milling process that resulted in an average particle size of 3.01 µm or ball milling for 20 hours, leading to smaller particles with an average size of 0.87 µm (**Figure 2.2b**). The sizes of the synthesised particles are close to the theoretically calculated limits, as indicated by the highlighted regions in **Figure 2.2a** and **Figure 2.2b**, allowing for assessing the trade-off between network recovery for printing and high piezoelectric performance.

The influence of particle size on the maximum achievable printable volume fraction was investigated by analysing the successful viscoelastic transition of the inks when subjected to shear stress, as demonstrated in **Figure 2.2c** through oscillatory shear sweep tests. When using larger particles (3.01 µm), we observed that the maximum usable volume fraction with our desktop extrusion-based printer equipped with a 0.58 mm nozzle was 47.5%. At this volume fraction, the ink transitioned from elastic to viscous behaviour at around 50 Pa, indicated by the cross-over between the storage and loss moduli in the oscillatory shear stress sweep (**Figure 2.2c**). Beyond this volume fraction (> 47.5%), the storage modulus and viscosity of the material, as shown in SI- **Figure S2.2 a, b,** were too high and impeded smooth line printing, leading to issues with flow initiation and nozzle clogging. In contrast, when employing smaller particles (0.87 µm), the maximum printable volume fraction was limited to 25%, as shown in **Figure 2.2c**. This variation

in the maximum usable volume fraction aligns with the hypothesis that larger particles, with their smaller surface area to volume ratio, experience fewer interparticle interactions. This results in reduced particle jamming compared to smaller particles and lower viscosity, thus allowing for an increased maximum printable volume fraction. This observation is consistent with literature on colloidal processing of other ceramics[22].

Next, we conducted recovery tests that simulated the printing conditions to assess the viscoelastic recovery behaviour of the inks after printing (**Figure 2.2d**). The ink containing smaller particles showed a quick drop in viscosity on being subjected to rotational shear stress followed by a rapid elastic recovery after removal of the stress, with the elastic shear modulus (solid squares) recovering almost instantly to original values, as seen in **Figure 2.2d**. In contrast, we observed that the ink with larger particles showed no recovery due to the increased gravitational forces compared to Brownian forces, which hinder the recovery of a network structure. This can be seen in **Figure 2.2d**, where the viscous part, G" (hollow circles), demonstrates higher stress values than the elastic part, G' (solid circles).

Whilst this presents a problem for printing relying on the recovery of yield stress to provide fidelity, this lack of recovery of elastic properties in the ink with larger particles can be effectively addressed by in-situ curing of a UV-curable monomer sequentially before printing succeeding layers of ink. The in-situ UV curing of the composite ink leads to a highly cross-linked and stiff polymer matrix with a T_g around 75ºC (**Figure S2.3a**). It significantly increases the yield strength to around 2.1 kPa, compared to the 50 Pa of the uncured ink, as depicted in **Figure S2.3b**, allowing it to achieve sufficient yield strength to resist the weight imposed by subsequent layers and prevent gravitational sagging.

Lastly, we examined how particle size and their resulting volume fractions influence the piezoelectric performance of the two inks. The ink with smaller particles with a volume fraction of 25% has a d_{33} of 2.5 $pC \cdot N^{-1}$ and g_{33} of 11 $V \cdot m \cdot N^{-1,}$ and is consistent with state-of-the-art DIW piezo-composite formulations with similar volume fractions[16]. However, the ink with larger particles exhibits significantly higher d_{33} of 17 $pC \cdot N^{-1}$ and g_{33} of 32 $V \cdot m \cdot N^{-1}$, particularly a much greater d_{33} than the smaller particle ink, as shown in **Figure 2.2e**.

This difference in properties between the two particle sizes is mainly attributed to the dominance of volume-related effects when using larger particles. Based on Yamada's model [14] for binary systems with piezoelectric ceramic fillers distributed in a polymer, we know that the dielectric constant of the composite is highly

dependent on the dielectric constant of the polymer matrix. Particularly in composites with significant differences in dielectric constant between the filler and matrix, the applied electric field gets confined by the low dielectric permittivity of the polymer and is unable to transfer effectively to the filler[19]. Hence, previous work by Stuber et al. has observed that larger particles and agglomerations can increase the dielectric constant, likely due to the lower amount of filler-matrix interfaces[23]. In essence, anything that reduces the mismatch between the permittivity of the filler and matrix or reduces the number of interfaces where these losses can occur, can help in increasing the piezoelectric properties of the composite.

Using larger particles leads to lower interfacial effects, which primarily contributes to reduced viscosity at higher volume fractions, while also reducing dielectric losses at the interface between the high dielectric constant piezoelectric filler and low dielectric constant matrix. Consequently, this leads to significantly higher dielectric and piezoelectric constants for the larger particles.

These findings align with the analytical predictions made for these piezo-composites utilising randomly dispersed particles, as shown in **SI**- **Figure S2.5-S2.7**. This combination of both high d_{33} and g_{33} values for the KNLN ink with larger particles compared to other DIW piezoelectric materials, as shown in **Figure 2.2e**, makes the ink suitable for transducer devices capable of operation in both actuation and sensing modes. This, however, comes at the expense of poor elastic recovery after printing due to increased gravitational forces, which we resolved by sequentially UV-curing each layer (**Figure S2.3b**).

Further, a support ink was developed to print the non-piezoelectric support precisely, clamping the piezoelectric membrane and facilitating its vibrational movement. The support ink was formulated by incorporating 8 wt.% hydrophobic fumed silica into PEGDA. Rheological characterisation of the support ink, as shown in **Figure 2.2f,** demonstrated that the support ink undergoes a similar viscoelastic transition on the application of shear forces compared to the piezoelectric ink, as seen by the cross-over of the storage and loss moduli (G' and G"). The elastic recovery of the support ink was tested similarly to the piezo inks and it can be seen that they exhibit immediate elastic recovery upon removal of shear stress (**Figure 2.2g**) as seen by the instantaneous recovery of the storage moduli (G') after removal of rotational shear. This enables printing support structure layers successively without the need for intermediate curing, as they can retain their shape through elastic recovery and support subsequent layers due to their high elastic properties.

The load-bearing capabilities of the support ink are essential as they serve the critical role of forming the clamping piezoelectric structure. Prints were evaluated by examining the sagging of bridging elements printed with this ink. The results demonstrated that the ink effectively bridged spans of up to 3.5 mm with minimal sagging, maintaining a tolerable sag of less than 0.2 mm. Additionally, the extent of sagging (z-deflection) in the printed filaments increased proportionately to the spanning length, as depicted in **Figure 2.2i**. We hypothesize that the difference in measured vs theoretical deflection, especially for shorter spanning lengths, arises from the viscoelastic nature of the material and due to the shear-thinning nature of the paste. Smaller aspect ratio beams tend to experience more shear-induced deformation, as predicted by Timoshenko's beam theory[24] and for aspect ratios smaller than 5, beam theories become inaccurate. As the aspect ratio increases, the experimental results increasingly match the Euler-Bernoulli predictions as seen in **SI Figure S2.4**, showing that lower aspect ratio beams are significantly influenced by shear deformation.

Since the operating parameters such as frequency and out-of-plane displacement of the piezo membranes also depend on the geometry and clamping efficiency of the support structure, it is important to test the precision in printing of support structure inks. The precision of the support structure was examined by printing circular rings and subsequently measuring the printed diameters. When attempting to print a ring with an inner radius of 0.5 mm, the printed ring gets filled and closed. This may result from a combination of factors, including the nozzle diameter being the same size as the print radius and the viscoelastic material properties leading to extensional effects, cohesion and closing of small gaps. However, from 1.5 mm radius onwards, we identified that reliable prints could be achieved with a nozzle with a diameter of 0.58 mm, as evidenced by low standard deviation values in **Figure 2.2h**.

The optimised piezoelectric ink and support inks were subsequently utilised to print and test ultrasound transducers.

2.2.2. DESIGN AND DYNAMIC CHARACTERISATION OF THE 3D PRINTED ULTRASOUND TRANSDUCERS

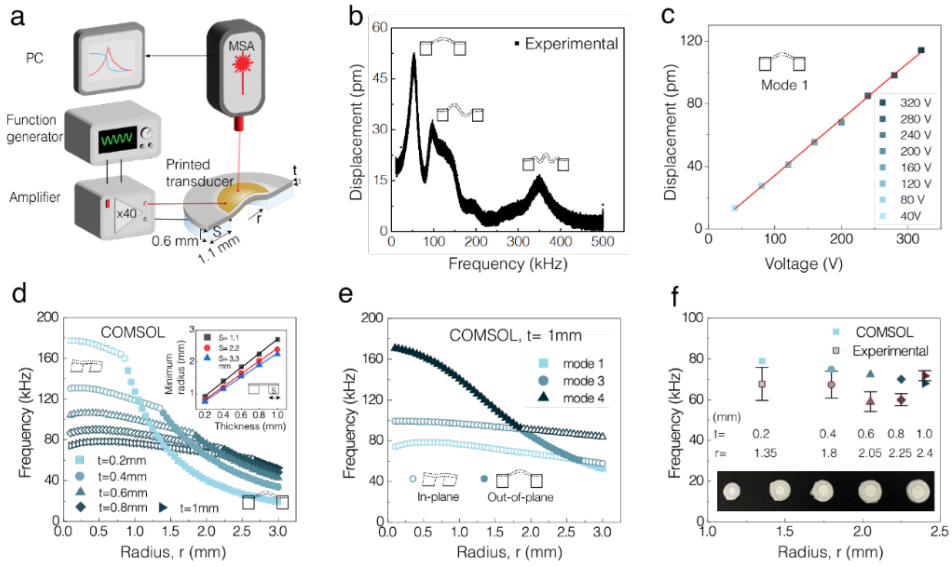

Figure 2.3: Design and dynamic characterisation of the 3D printed ultrasound transducers. (a) Schematic of the setup, illustrating the printed transducer with a radius (r) and thickness (t), driven to resonance by a waveform function generator amplified by a 40x voltage amplifier. Membrane vibrations are measured using a Polytec Laser Doppler Vibrometer (LDV) MSA400. (b) Measured frequency response of a transducer with r= 1.5 mm and t= 0.2 mm, along with the corresponding schematics of mode shapes. The frequency response of the membrane shows maximum out-of-plane displacement in the fundamental mode. (c) The linear increase in the out-of-plane peak displacement amplitude of the first resonant mode with input voltage. (d) COMSOL simulation data illustrating the impact of varying radius (r) and thickness (t) of the transducer on the fundamental mode frequency and mode shape, highlighting the transition from in-plane displacement (hollow points) to out-of-plane (solid points) with increasing radius and decreasing thickness of the piezo-membrane. The inset indicates that for a specific support thickness S, the minimum radius of the membrane required to maintain the out-of-plane mode increases linearly with the thickness of the membrane. (e) Behaviour of higher modes in thicker transducers (t = 1 mm) with varying radii. (f) Specific thickness (t) and radius (r) combinations were used for manufacturing to maintain a constant frequency. Experimental fundamental mode frequencies are compared to those obtained from COMSOL simulation, demonstrating close agreement.

We then utilise the optimised piezoelectric and support inks to print ultrasound transducers and characterise their dynamic behaviour. Circular piezoelectric membranes with radius (*r*) and thickness (*t*) were 3D printed, along with a support structure of constant height (0.6 mm) and wall thickness (*S*= 1.1 mm) to clamp the membrane (**Figure 2.3a,** also **SI Figure S2.8**). The mechanical vibrations of the piezo membranes with electrical input were measured using a Polytec Laser Doppler Vibrometer (LDV), as shown in **Figure 2.3a** (also **SI-Figure S2.9** for actual setup and printed transducers). In order to understand the frequency dependent

dynamic behaviour of the membranes, a linear chirp signal generated by the LDV function generator was used to stimulate the membranes and the resulting out-of-plane displacement was measured. **Figure 2.3b** presents the area- averaged magnitude of the frequency response of the transducer with r = 1.5mm and t = 0.2mm, showing three vibration modes. It is noted that the fundamental mode, observed as the first peak in the frequency response curve, exhibits the highest displacement. This mode corresponds to the axisymmetric out-of-plane bending motion of the piezo-membrane, enabling the membrane to act as a monopole source and efficiently radiate sound by voltage signal.

To understand the voltage-dependent actuation of this mode, we measured the frequency response of the membrane at a point near its centre under different excitation voltages. To prevent electrical and mechanical breakdown of the membranes, we operated the transducer at much lower voltages (max. 200V) than the breakdown voltage (>2000 V). We observed that displacement increases linearly with increasing voltage, as indicated by the linear relationship between the out-of-plane displacement and the voltage in **Figure 2.3c.** This is beneficial for the linear tunability of the sound pressures when developing a sound transducer.

To leverage the capability of fabricating millimetre-scale ultrasound transducers, we investigated the impact of further increasing the transducer dimensions on the resonance behaviour and out-of-plane motion of the membranes. Using finite element simulation with COMSOL, we analysed the effect of changing the radius (r) and thickness (t) on the dynamic behaviour of the membrane. In the simulations, we first derived the mechanical, dielectric, and piezoelectric properties of the 47 vol% KNLN-PEGDA piezo-composites from analytical methods and incorporated them into a custom material in the FEM model (**SI- Figure S2.5-S2.6**). Then, the influence of changing dimensions of the piezo membrane on the mode shapes and resonance frequencies was analysed, as shown in **Figure 2.3d**.

The analysis revealed that increasing the radius while decreasing the thickness of the membrane led to a transition in the fundamental resonance mode, shifting from primarily in-plane displacement (depicted by hollow points) to the desired out-of-plane motion (depicted by solid points) (**Figure 2.3d**). Simulations indicated that once the transducer shifted to the out-of-plane displacement mode, the fundamental frequency decreased exponentially with increasing radius, as expected, which is particularly evident for the t = 0.2 mm membrane (square points). To further investigate this, we examined the relationship between membrane thickness and the minimum radius required to have out-of-plane motion, illustrated

in the inset, demonstrating a linear increase with thickness. This results in a constant ratio of thickness and radius (*t*/*r*) or slenderness of the membrane, as shown in the inset, allowing the piezo layer to vibrate as a membrane.

We also observed that changing the thickness of the support structure (S) affected this slenderness for the membrane mode, with increasing support thickness causing a reduction in the minimum radius (inset of **Figure 2.3d**). However, we observed that further increase in support thickness have a diminishing effect when changing *S* from 2.2 to 3.3 mm. This shows that the support thickness also plays a role in the fundamental frequency of the transducers, particularly if the thickness is insufficient for effective clamping. The optimal support thickness where the effect of the support diminishes depends on the thickness of the membrane.

As discussed earlier, the minimum radius requirement increases with greater thickness. Therefore, we examined the displacement and mode shape of higher modes in thicker transducers (t = 1mm) with varying radii, as depicted in **Figure 2.3e**. It can be seen that when the radii are less than 2.5 mm, the fundamental mode does not exhibit the desired out-of-plane mode, but mode shape with complex bulk motion, since the resonator cannot be taken as a simple plate or membrane. However, to maximize the output sound pressure and transduction efficiency when designing a sound transducer, it is preferable to have the out-of-plane mode as the fundamental mode and higher-order modes such as mode 3 (1.75 < r < 2.5 mm) and mode 4 (r < 1.75 mm) demonstrate some out-of-plane displacement, as emphasised by the solid points.

By understanding how the dimensions of a 3D-printed transducer membrane and support impact its resonance behaviour, we can create custom designs that deliver the desired frequency and displacement type. These insights were utilised to select specific thickness and radius combinations during the manufacturing process to maintain a nearly constant frequency, as illustrated in **Figure 2.3f**. The thickness of the transducer membranes was incrementally increased from 0.2 to 1.0 mm with a 0.2 mm step, aligning with the printing layer height. To maintain a consistent frequency and mitigate the impact of frequency variations on the measured pressure, given that sound attenuation is frequency-dependent, specific radii were chosen for these thicknesses to maintain a nearly constant frequency throughout the samples.

To validate our findings, we compared the experimentally measured fundamental frequencies with the frequencies predicted by our model. We observed that the experimental measurements agree well with the simulations (**Figure 2.3f**), with

slightly lower magnitudes, likely attributed to imperfect clamping conditions (**SI-Figure S2.10a-b**). Further, analysing the standard deviation (SD) of the resonant frequency measurements (n>4) indicates reduced variation for larger transducers. This higher accuracy with larger transducers demonstrates the advantage of DIW of transducers, as it allows for the fabrication of transducers with larger thickness values compared to SOI-based transducers, allowing commercial 3D printing techniques to be utilised without the need for micro-scale precision, showing the practical applicability of the fabrication process.

2.2.3. SOUND PRESSURE MEASUREMENT AND APPLICATION OF 3D PRINTED ULTRASOUND TRANSDUCERS

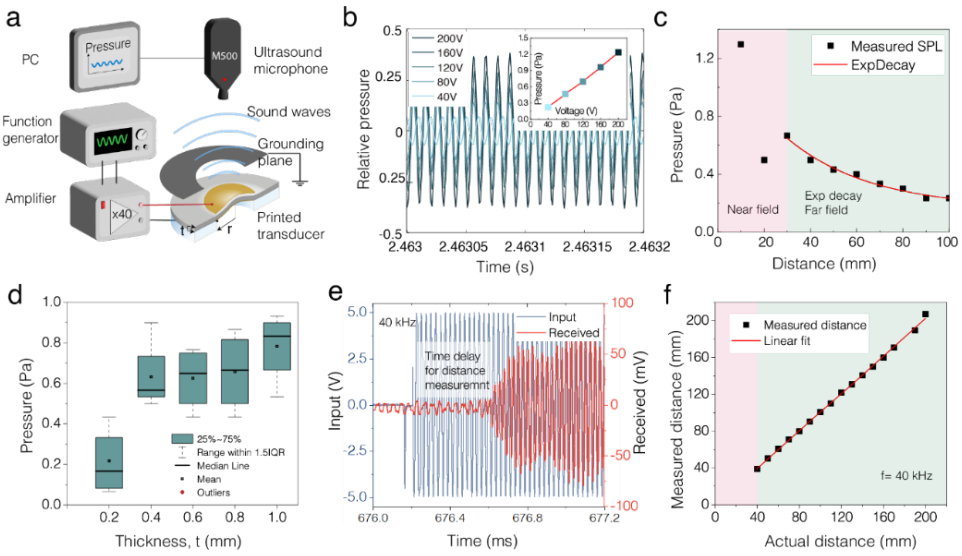

Figure 2.4: Sound pressure measurement and application of 3D printed ultrasound transducers. (a) Schematic of the sound pressure measurement setup testing the actuation mode of the printed transducer, illustrating the sound generation upon application of input voltage signal and measured pressure. A grounding plane eliminates electromagnetic interference between the microphone and the 3D-printed transducer, ensuring the measurement of sound pressure without interference. (b) The signal measured by the microphone shows the pressure and frequency of the generated ultrasound at different input voltages. The inset shows the linear increase in output sound pressure with rising input voltage. (c) Sound pressure versus distance, displaying a power-law decay in the far-field zone from 5 cm. (d) Sound pressure measurements for transducers with different radius and thickness combinations at comparable operating frequencies, illustrating that increasing the transducer size, though not linearly, enhances output pressure. (e) Time of Flight (ToF) is measured using the emitted signal from the 3D-printed transducer as an ultrasound transmitter and the received signal from a commercial transducer for distance measurement. (f) The comparison between measured and actual distances showed good agreement between distances of 40 mm and 200 mm.

We then characterise the sound pressure generated by the 3D-printed ultrasound transducers using the experimental setup as shown in **Figure 2.4a** and **SI Figure S2.11**. By driving the printed transducer to resonance using a sine wave voltage signal, ultrasound was generated through the membrane's vibrations and then captured by a commercial wide-spectrum ultrasound microphone M500. This microphone M500 gave us relative pressure values, which were then calibrated using a commercial Murata 40 kHz ultrasound transducer with a known output sound pressure to convert relative pressure to absolute values, as detailed in Supplementary Information **(SI-Figure S2.12).** Further, we used a conductive grounding plane between the printed transducer and the microphone to eliminate any electromagnetic interference and ensure only the measurement of the transducer's acoustic output.

Figure 2.4b shows the pressure and frequency of the generated ultrasound at various input voltages, as captured by the microphone. Notably, we observed a linear relationship between the output sound pressure and the input voltage (see the inset of **Figure 2.4b**), which shows the advantage of scaling up to millimetre-scale dimensions, as higher input voltages can be applied without electrical breakdown, resulting in higher output pressures. **Figure 2.4c** illustrates the relationship between this generated sound pressure and the distance of measurement, exhibiting a decay in the far-field zone beyond 5 cm. While the sound pressure measurements in the near-field zone (<5 cm) were affected by constructive and destructive interference from reflected waves, the far field (>5 cm) provides a conducive environment for precise sound pressure measurements using a single microphone setup[25] as interference from reflected waves can be minimised. Consequently, all pressure measurements were conducted at this optimal distance.

To underscore the significance of transducer size on the generated output pressure, we measure the sound pressures of transducers with varying radius and thickness combinations, as presented in **Figure 2.4d**. As can be seen in **Figure 2.4d,** enlarging the transducer size from (*t, r*) = (0.2,1.35) mm to (0.4,1.8) mm results in a substantial increase in the mean output pressure from 0.21 to 0.63 Pa**.** This shows the significance of creating ultrasound transducers with larger dimensions, enabling the fabrication of transducers with mm-scale dimensions using commercial 3D printers.

With further increases in dimensions, particularly observed for t= 0.6, 0.8 and 1 mm, it becomes evident that while the net pressure continues to rise, the rate of increase

diminishes with larger dimensions. This trend can be explained by the diminishing clamping efficiency of the support structure as thickness increases while maintaining the same support thickness. This results in the inefficient higher-order modes becoming increasingly proximal to the efficient out-of-plane displacement modes as thickness grows (**SI-Figure S2.10b**). Consequently, multiple modes are activated, resulting in lower output pressure than anticipated.

To demonstrate the actuation capability and show the 3D printed transducer as an ultrasound actuator for distance measurement, a 40 kHz transducer was designed based on the guidelines obtained from previously described simulations and 3D printing (**SI-Figure S2.13**). This printed transducer was then actuated using a sinusoidal voltage signal at the same frequency. A commercial 40 kHz Murata ultrasound transducer was used as the receiver. The Time of Flight (ToF), as shown in **Figure 2.4e,** between the transmitted and received signals was utilised to calculate the measured distance between the actuator and the receiver. Measurements with distance below 40 mm were unreliable due to interference from the near field and electromagnetic interference, obscuring the first peak and potentially resulting in miscalculations. Additionally, distances above 200 mm could not be measured, as they exceeded the height limit of the printer used to set the distance between the actuator and the commercial sensor. The measured distances obtained from ToF using the 3D printed transducers exhibited excellent agreement with the actual distances within the range of 40 mm to 200 mm as can be seen in **Figure 2.4f**. This highlights the practicality and versatility of the 3D printed transducers, emphasising the ease with which they can be printed and fine-tuned for diverse applications that demand actuation.

2.3. CONCLUSIONS

By optimising particle size and transducer design, we demonstrated tunable actuation performance in 3D-printed piezoelectric composites. We designed the piezo ink through careful selection of particle size to balance the trade-off between high piezoelectric response and the printing fidelity arising from competing effects of Brownian recovery and gravitational settling. Our examination of particle sizes revealed that larger particles around 3 µm increase the d_{33} of the composite more than an order of magnitude than similar state-of-the-art direct ink writing piezo composites. The loss of the elastic recovery of the ink due to the increased size of particles was effectively addressed by an in-situ layer-by-layer curing of the UV-curable piezo ink. This enabled us to create free-form piezoelectric materials that can be co-cured with structural materials at room temperature to create ultrasound transducers with a tailorable frequency response.

Further, we studied the impact of scaling up transducer dimensions on membrane resonance behaviour to design millimetre-scale ultrasound transducers with a desired out-of-plane motion. We tested the printed transducers at around 80 kHz for the acoustic pressure generated through piezoelectric membrane vibration. The measurements revealed a significant increase in pressure with increasing transducer size, with an increase from (t, r) = (0.2,1.35) mm to (0.4,1.8) mm, resulting in a rise in mean output pressure from 0.21 to 0.63 Pa. Finally, we tuned the printed transducer to a frequency of 40 kHz and used it as a transmitter for precise and accurate distance measurement, highlighting the practical utility of our printed transducers.

In contrast to conventional silicon-based manufacturing, which requires microscale precision and high-temperature methods, our DIW-printed piezo composites using commercial 3D printers enable cost-effective mass printing of transducers into complex-shaped objects while ensuring robust bonding between the surfaces, opening up avenues in the field of multi-material 3D printing using functional materials. Thus, our printing technique provides a pathway to scalable and bio-compatible manufacturing of piezo-embedded intelligent structures with built-in sensing and actuation capabilities, with potential applications in the field of bio-medical devices and aerospace engineering.

2.4. MATERIALS AND METHODS

Ceramic synthesis

$K_{0.485}Na_{0.485}Li_{0.03}NbO_3$ (KNLN) ceramic powder was prepared through a conventional solid-state reaction with a two-step calcination procedure that has been previously studied[26]. Stoichiometric proportions of >99 % Na_2CO_3, K_2CO_3, Li_2CO_3, and Nb_2O_5 (Sigma Aldrich) were milled with 5 mm yttria-stabilised ZrO_2 balls in hexane for 3 hours at 200 rpm. The milled powders were air dried on a hot plate at 100°C for 1 hour, and the dried green powder was calcined at 1050 °C for 3 hours with a heating rate of 5 °C·min^{-1}. The calcined ceramic was milled with 5 mm balls in IPA for 3 hours at 200 rpm, followed by air dying and a second, longer calcination at 925 °C for 20 hours with a heating rate of 1 °C·min^{-1}. The calcined powder was ball milled in IPA for 15 minutes, air dried, sieved through a 90 µm sieve and then stored under vacuum. The particle morphology was analysed using a Scanning Electron Microscope, SEM (JEOL, JSM-7500F, Nieuw Vennep, the Netherlands). The particle size distribution of the milled powders was measured using Malvern Mastersizer 3000 on 0.1% weight/volume aqueous solution of the powders using sodium dodecyl sulphate solution as surfactant. The mean value of the distribution then represented the particle size of each type of powder.

Ink preparation

Piezoelectric ink: The synthesised ceramic powder was mixed with the UV-sensitive monomer Poly (ethylene glycol) diacrylate with Mn 250 (Sigma Aldrich) in varying volume fractions and combined in a planetary mixer (SpeedMixer DAC 150.1 FVZ) at 3500 rpm for 2 minutes in 30 s intervals with a 15 s break in between to prevent excessive heating of the components while high-speed mixing. Two photoinitiators (Irgacure 819, 184) were chosen to maximise the curing depth due to the high ceramic filler content to obtain a UV-curable piezoelectric ink. The photo-initiations are then added to the KNLN-PEGDA mixture in the ratio of 1% and 2 % wt. with respect to the weight of the monomer and mixed at 1000 rpm for 5 minutes to ensure homogenous distribution of the initiators.

Support ink: 8 wt.% of hydrophobic pyrogenic fumed silica (HDK 18) wrt. to monomer weight was mixed with PEGDA 250 in a planetary mixer (SpeedMixer DAC 150.1 FVZ) at 3500 rpm for 5 minutes. Then, 1 wt.% photoinitiator Irgacure 184 wrt. to monomer weight was added to the mixture and mixed at 1000 rpm for 2 minutes.

Rheological characterisation

The rheological properties of the inks were characterised using a rotational rheometer (Haake Mars III, Thermoscientific) with a 20 mm diameter serrated plate geometry using a gap height of 1 mm. Serrated plates prevent artefacts in measurements arising from wall slip, which has been studied to occur when highly loaded dispersions are subject to high localised deformation. Shear storage and loss moduli were determined as a function of shear strain via dynamic amplitude sweeps at a fixed frequency of 1 Hz with a stress sweep. The yield stress was measured via steady-state flow experiments with a sweep of shear stress and measuring. We used the point of change in slope of the log-log plot of shear stress vs strain to calculate the yield stress of the ink. The elastic recovery of the ink was measured using a time-dependent oscillation-rotation-oscillation (ORO) test. To simulate at-rest behaviour, an amplitude sweep was performed at low shear stress within the linear viscoelastic regime (LVR), followed by a high shear rate (10 s^{-1}) rotation to simulate the time scales and stresses experienced during printing. Subsequently, the recovery in elastic moduli over time was measured with the low amplitude oscillatory sweep.

Printing and curing

A commercial desktop printer (Ultimaker 2+) was modified by replacing the original print head with a custom-made ink extrusion system consisting of a 25 ml syringe holder and a mechanically driven syringe pump. The 3D models of the transducers were sliced in Cura with a print speed of 10 $mm \cdot s^{-1}$ using a nozzle with an inner nozzle diameter of 0.584 mm. The printed lines or parts were cured using an Omnicure S1500 (Lumen Dynamics) UV-lamp at 100% intensity at 20 cm for 2 seconds between each layer and 10 seconds for the final part.

Bridging ability of the ink

To assess the ability of the support ink to be able to resist deformation under its weight and form complex shapes, a triangular support structure was printed like the work done by Kleger et al., followed by printing spanning filaments across the support structure. To evaluate the sagging behaviour, the deflection of the filaments was imaged using a Keyence VR-5000 Optical Profilometer. The filaments' length and deflection were measured by analysing the image from the Profilometer using

ImageJ. Density of the support ink was measured to be 1.2 $g \cdot cc^{-1}$. The storage modulus of the ink after recovery obtained from the recovery test was used to calculate the theoretical deflection. The experimental deflection was compared to the calculated theoretical deflection calculated in SI section 5.

Poling

Depending on the application, either gold or carbon paste electrodes were applied. Gold electrodes were used for samples for LDV measurements to ensure a bright, reflective surface for the laser light. Gold electrodes (50-100nm) were sputtered on the top of the transducer through a 3D-printed shadow mask with a sputter coater for 2 minutes (QuorumQ300T, East Sussex, UK). Since the gold electrodes are very thin and fragile, conductive carbon paste was obtained from Dupont 7102 and applied using a paintbrush for applications where robust electrodes were required without the need for high reflectivity. To align the dipoles in the piezoelectric domains, the piezo-composites were poled in a silicon oil bath kept at 120 °C by applying a DC field of 10 $kV \cdot mm^{-1}$ for 5 min. The electric field was then turned off, and the samples were retrieved immediately without cooling under the field and cleaned.

Piezoelectric characterisation

The piezoelectric charge coefficient, d_{33} ($pC \cdot N^{-1}$) of the poled piezoelectric films were measured using a Berlincourt (PM 300, Piezo test, London, UK) piezometer with a static force of 10 N and a dynamic peak-to-peak sinusoidal excitation of 0.25 N at 110 Hz. The capacitance and dielectric loss were measured at 1 kHz and 1 V with an Agilent 4263B LCR meter (Santa Clara, CA, USA). The value of relative permittivity ε_{33}, measured under zero stress, was derived from the capacitance. The piezoelectric voltage constant, g_{33} ($mV.N^{-1}$) of the films were calculated using the ratio of d_{33}/ε_{33}.

Laser Doppler Vibrometry

A Polytec Laser Doppler Vibrometer MSA400 was used for the dynamic behaviour measurements. Signals were generated by the Polytec function generator and then amplified 40x (voltage gain) by a voltage amplifier (Delta Elektronica) to actuate the printed piezo transducer into vibration. The laser was generated by the MSA400

laser head and focused on the region of interest to read out the membrane's vibration signals, which will be subsequently decoded by a Polytec VD-09 Digital Velocity Decoder and transformed into digital velocity data.

Ultrasound pressure

Sinusoidal voltage signals were generated by a function generator (33500B, Agilent Technologies, Loveland Colorado, USA) and then amplified 40x (voltage gain) by a voltage amplifier to actuate the printed piezo transducer into vibration. A commercial M500 USB Ultrasound microphone was used to receive the ultrasound, and the reading was obtained from the software Batsoundlite. The microphone was mounted to an Ultimaker head, and the printed transducer was placed on the bed. The gantry system of the Ultimaker was used as a precise x, y, and z-control stage to ensure the centring of the transducer and height measurement.

Distance measurement

A 3D printed transducer, resonating primarily at 40kHz, was fabricated and poled using the previously described method. Sinusoidal voltage signals were generated by a function generator (33500B, Agilent Technologies, USA) and amplified by 40x using a voltage amplifier (Delta Elektronica) to drive the printed piezo transducer into vibration. A commercial 40 kHz Murata ultrasound transducer received the ultrasound signals, and readings were captured using an oscilloscope (Picoscope 5442D series). The receiver was attached to the head of a Prusa MK3 3D printer, while the printed transducer was positioned on the bed. The Prusa gantry system provided precise x, y, and z-control to ensure transducer alignment and height consistency. Continuous measurements were conducted using the Picoscope, and the input to the printed transducer was toggled manually to create a long pulse. The receiver output signal was amplified 40x and recorded through the oscilloscope. The amplitude of the received signal takes some time to reach a stable level, and the first few waves have an amplitude lower than that of the electromagnetic noise. This makes it challenging to measure the time of flight using the first peaks; to combat this, we observed that at a distance of 100 mm, the first trough with amplitude above the noise level corresponded to the fourth trough of the input signal. All other time of flight measurements were made consistently between the first trough of the received signal with amplitude above noise amplitude and the fourth trough of the transmitter input signal.

2.5. SUPPORTING INFORMATION:

2.A.1. MORPHOLOGY OF KNLN PARTICLES AND PARTICLE DISTRIBUTION IN COMPOSITES

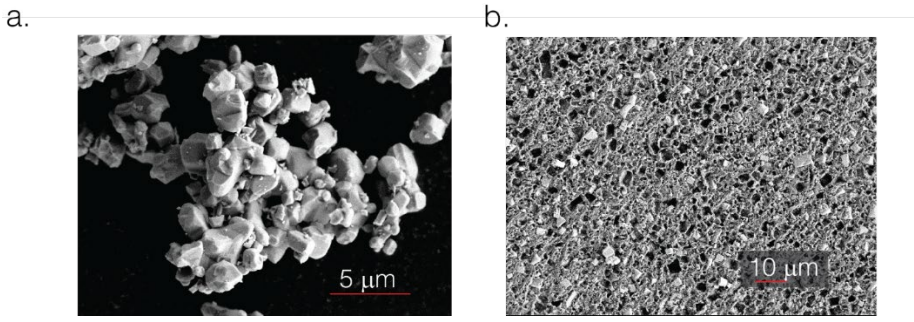

Figure S2.1: Morphology of the a) synthesized particles and b) the particle dispersion in the KNLN-PEGDA composite observed via Scanning electron microscopy (SEM)

The morphology of the synthesized particles was analysed using a Scanning Electron Microscope (SEM) and is shown in **Figure S2.1a**. Further, the morphology of the particle dispersion in PEGDA was studied using SEM of a cracked cross-section surface as shown in **Figure S2.1b**. Visually, from the SEM image, the presence of both stuck and detached particles on fracture with a clear outline of the cuboidal KNLN particles can be seen. We can observe that from the SEM image that the KNLN particles were randomly distributed throughout the PEGDA polymer matrix.

2.A.2. STABILITY AND RECOVERY BEHAVIOUR OF THE PIEZO-COMPOSITE

The recovery behaviour of the piezo-composite depends on the ability of the suspension to regain its randomly oriented structure on the removal of shear stress. This depends on the ratio of the gravitational forces to the Brownian forces acting on the particles from being suspended in the medium and is given by Equation **S1** [21]

$$\frac{Grav}{Brownian} = \frac{a^4 \Delta\rho g}{k_B T} \qquad (S1)$$

where a is the radius of the particle or clump of particles,
$\Delta\rho$ is the density difference between the particle and the liquid medium,
g= 9.8 m·s^{-2} is the acceleration due to gravity,
k_B=1.38×10^{-23} J·K^{-1} is the Boltzmann constant and,
T= Temperature in K

Using KNLN density of 4510 kg.m^{-3} and PEGDA density of 1100 kg.m^{-3} and room temperature of 23 °C:

Particle size (µm)	Gravitational to Brownian forces ratio
0.6	1.0
0.87	**4.6**
1	8.2
3.01	**670**
10	81800

Table S2.1: Effect of particle size on the ratio of gravitational to Brownian forces.

From **Table S2.1**, the gravitational forces on the larger particle size (3.01 um) are more than two orders of magnitude higher than that of the smaller size (0.87 um) which is close to the ideal size of 0.6 um.

2.A.3. VOLUME FRACTION VS PRINTABILITY

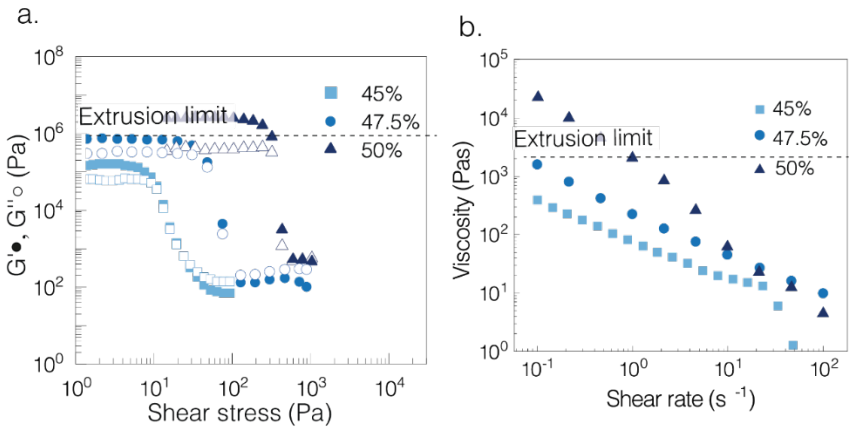

Figure S2.2: Rheological characterisation of KNLN inks (3.01 µm) with different volume fractions. (a) Storage and loss moduli (G' and G") plotted against shear stress for volume fractions of 45%, 47.5%, and 50%. (b) Viscosity versus shear rate for volume fractions of 45%, 47.5%, and 50%.

2.A.4. PROPERTIES OF CURED INKS

While printing the piezo layers and successively curing them between prints, we cured each layer for only 2 seconds, as the polymer reaction was quite rapid. After the final layer was printed, we performed a curing of 10 seconds for the fully printed part to ensure complete curing. The reaction is quite instantaneous due to the monomer being a short-chain reactive PEGDA with a high initiator concentration (3 wt.% of the polymer in total) and a powerful UV lamp, the Omnicure S1500 with a 200 W lamp.

We measured the Tg of cured base ink- PEGDA 250 using Digital scanning calorimetry (DSC) as shown in **Figure S2.3a**. We performed heat-cool-heat cycles from -70 °C to 150 °C. The first heat cycle is used to remove any thermal history in the material, and the first cooling and second heating cycles are shown in the Figures below. We repeated the DSC with slower heating/cooling rates (2°C /min) and longer isothermal holds between cycles and we found that the T_g of PEGDA 250 to be consistently between 50-85 °C both times, as seen in the Figures below, with the inflection point was calculated to be around 75 °C from the derivative of the graph.

Similarly, we performed oscillatory sweep tests on the piezo inks before and after curing as shown in **Figure S2.3b**. The ink before curing transitioned from elastic to viscous behaviour at around 50 Pa, indicated by the cross-over between the storage and loss moduli in the oscillatory shear stress sweep. The yield point for the cured ink was much higher at 2.1 kPa.

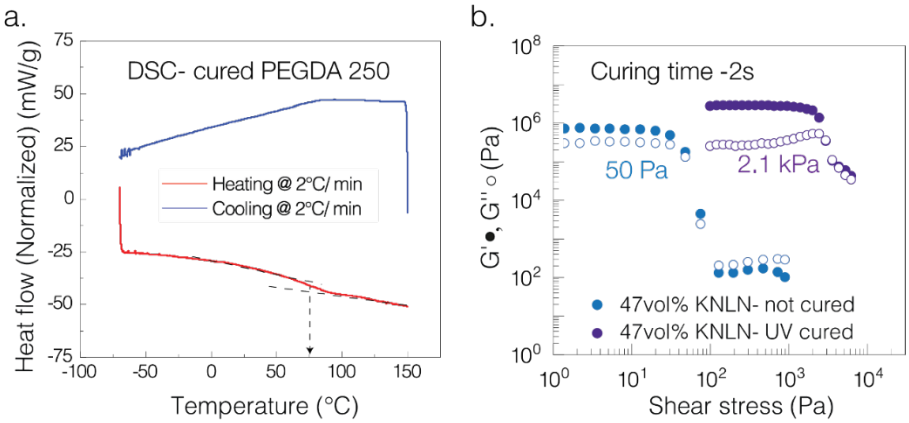

Figure S2.3: Properties of cured inks(a) Digital scanning calorimetry on the cured base ink after 2s of UV curing shows a stiff network with a Tg around 75°C (b) An increase in yield point was observed in the cross-over point between G' and G" for uncured versus UV-cured 47.5 vol% KNLN ink from 50 Pa to 2.1 kPa.

2.A.5. BRIDGING TEST

A bridging test was performed similar to the work done by Kleger et al. to analyse the extent of sagging in the printed filaments.[27]

The theoretical deflection using Euler-Bernoulli equations for a simply supported beam with a length *L* and diameter *D*, the maximum z-deflection is given by **Equation S2** as follows:

$$\delta z_{max} = \frac{c}{G}\frac{5}{12}\left(0.25\rho_{paste} g \frac{L^4}{D^2}\right) \quad \text{(S2)}$$

Where G is the Shear modulus, g is the gravitational acceleration constant and ρ_{paste} is the density of the piezo ink and c is a fitting parameter.

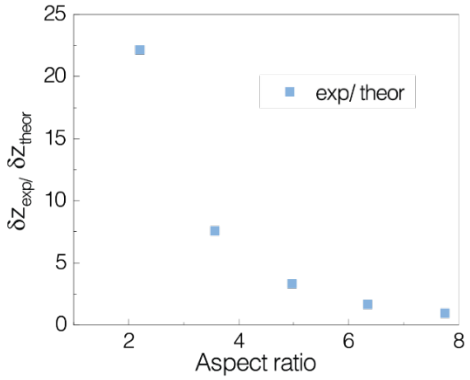

Figure S2.4: Ratio of experimentally measured z deflection vs theoretical prediction shows large variation for short spanning lengths due to the higher effects of shear-induced deformation in the shorter beams and eventually matching with the theoretical predictions for higher aspect ratios.

2.A.6. CALCULATION OF MECHANICAL, DIELECTRIC, AND PIEZOELECTRIC PROPERTIES

To model the transducers in COMSOL, the mechanical, dielectric, and piezoelectric properties of the piezo ink need to be calculated as input. Material properties of KNLN 47.5 vol% -PEGDA 250 used as input for simulations are as follows:

Density of KNLN filler: 4510 kg/m^3
Density of PEGDA: 1100kg/m3
Density of composite (47.5 vol%): 2725 kg/m^3

Input parameters of KNLN3 from Saito et al. (2006) Ferroelectrics [28]

Stiffness, E_f= 117*10^9; %[Pa]
Poisson's ratio, nu_f=0.3
d33 of KNLN, d33_f = 120*10^-12; %C/N [KNLN3]
Permittivity of KNLN, e_f = 400.
rho_f = 4.51; %g/cm^3

Input parameters of PEGDA 250 from Yao et al. (2019) AFM and Sigma Aldrich website

Stiffness, E_m= 2*10^9; %[Pa]
Poisson's ratio, nu_m=0.3
rho_m = 1.11; %g/cm3
Permittivity of PEGDA 250, e_f = 6.

Young's modulus of piezo-composite:

For a particle filled polymer, the Young's modulus, E (GPa) was derived using Hashin-Strikman bounds **Equation S3** [29]

$$E = \frac{1 + \zeta \eta v_f}{1 - \eta v_f} \qquad (S3)$$

Where ζ is the shape factor and since the KNLN particles are roughly cubic, $\zeta = 2$, v_f is the volume fraction of the particles (ϕ) and η is given by **Equation S4**:

$$\eta = \frac{\frac{E_p}{E_u} - 1}{\frac{E_p}{E_u} + \zeta} \qquad (S4)$$

Where E_p is the Young's modulus of KNLN=117 GPa[4] and E_u is the Young's modulus of PEGDA-250= 2 GPa

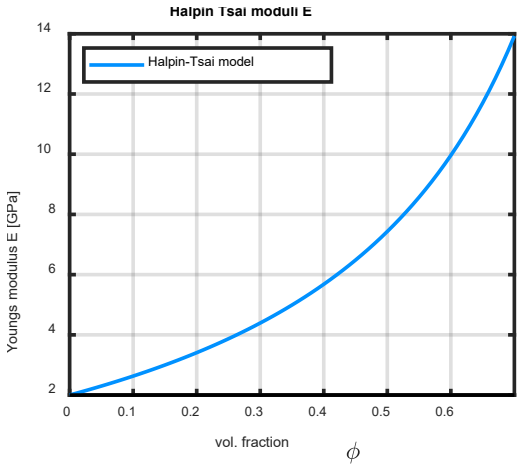

Figure S2.5: Analytically modelled Young's modulus of the KNLN-PEGDA 250 piezo-composite as a function of the volume fraction of the KNLN powder.

Relative dielectric permittivity ε_r, of composite

The dielectric and piezoelectric constants of the randomly dispersed, bi-phasic composites were predicted using Yamada's model [14] The dielectric constant of the composite is given by **Equation S4**:

$$\varepsilon = \varepsilon_1 \left(1 + \frac{n\varphi(\varepsilon_2 - \varepsilon_1)}{n\varepsilon_1 + (\varepsilon_2 - \varepsilon_1)(1 - \varphi)}\right) \quad (S4)$$

Where ε = dielectric constant of the composite

ε_1= dielectric constant of the matrix = 6

ε_2= dielectric constant of the filler= 400[28]

φ = volume fraction of the filler

n = shape parameter= 10

The dielectric constant ε of the composite is calculated using Equation S4 and the experimentally obtained values are compared with analytical values in **Figure S6**.

Similarly, the piezoelectric charge constant of the composite is given by **Equation S5**.

$$d_{33} = \varphi \alpha G d_{33_2} \quad (S5)$$

Where α = poling ratio of filler

d_{33_2}= piezoelectric charge coefficient of filler= 120 pC·N^{-1} [4]

G = local electric field coefficient and using parameter n, is as follows:

$$G = \frac{n\varepsilon}{n\varepsilon + (\varepsilon_2 - \varepsilon)}$$

The experimental measurements of the piezoelectric charge constant d_{33} in the composite closely align with the analytical values when assuming a poling ratio α of 0.5, as seen in **Figure S2.6**. This suggests that the poling conditions could potentially be further optimised to enhance the value of d_{33}. Alternatively, it is possible that defects induced during the ball milling process after calcination may result in mechanical pinned domains in the KNLN, hindering complete poling similar to the observed behaviour in cold-sintered KNN [30].

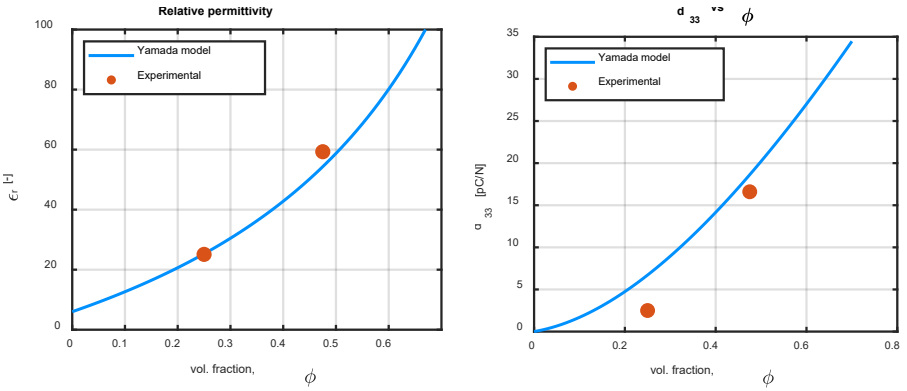

Figure S2.6: Dielectric constant ε vs Filler volume fraction ϕ and Piezoelectric charge constant d_{33} vs ϕ of the piezo ink calculated via Yamada model compared with experimentally obtained values.

Broadband dielectric spectroscopy (BDS) measurements were performed on the poled samples to study their dielectric behaviour over a range of frequencies. The **Figure S2.7** shows the real part of the dielectric permittivity (ε') and the loss factor (tan(δ)) at different frequencies. As observed, the losses at operating frequencies around the kHz range are approximately 0.1. The dielectric permittivity at 1 kHz from the BDS measurement is 59, which corresponds well to the measurement obtained from the LCR meter.

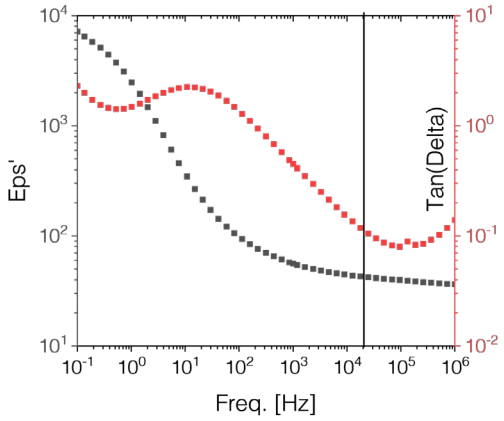

Figure S2.7: Dielectric constant ε and tan(delta) of the KNLN 47.5vol% PEGDA 250 composite at different frequencies. The vertical black line shows the operating frequency range (>20kHz).

2.A.7. COMSOL MODEL

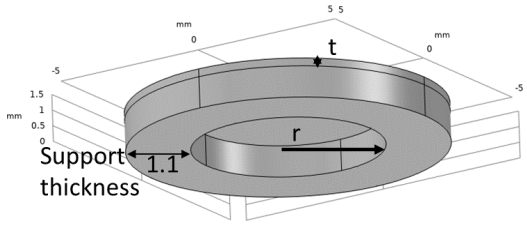

Figure S2.8: COMSOL model used to simulate the resonance and actuation behaviour.

A 3D model is created in COMSOL Multiphysics, consisting of a piezoelectric membrane with a thickness (t) and radius r+S where the support structure is designed as a hollow cylinder with a radius (r) and a thickness (S) of 1.1mm, as shown in **Figure S2.8** The bottom boundary of the support structure is mechanically clamped to simulate the experimental conditions where it is attached to a copper tape. An electric field is applied across the piezo membrane. The mechanical, dielectric, and piezoelectric properties of the piezo-composite which were determined using the analytical methods were incorporated into the model. and with the properties of the base polymer. Frequency sweeps were performed and the eigen modes and the corresponding eigenfrequencies for varying dimensions were determined.

2.A.8. MEASUREMENT OF RESONANT FREQUENCY OF TRANSDUCERS

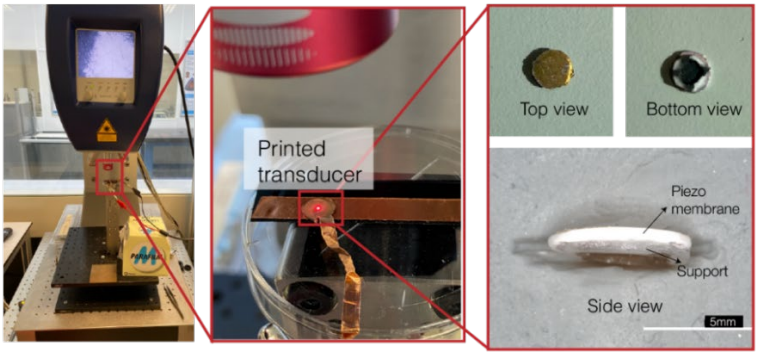

Figure S2.9: Measurement of the resonant frequency of the transducers using Laser Doppler Vibrometry. A Polytec Laser Doppler Vibrometer MSA400 was used for the dynamic behaviour measurements. Gold electrode was sputtered on the top of the transducer to ensure that the electrode surface was also reflective for the laser measurements, as shown in the top view. Conductive carbon paste was used on the bottom for robust electrodes as shown in the bottom view. The side view of the transducer shows the different layers, including the piezo membrane and the support structure cavity.

2.A.9. EFFECT OF CLAMPING SUPPORT THICKNESS ON RESONANT FREQUENCY OF TRANSDUCERS

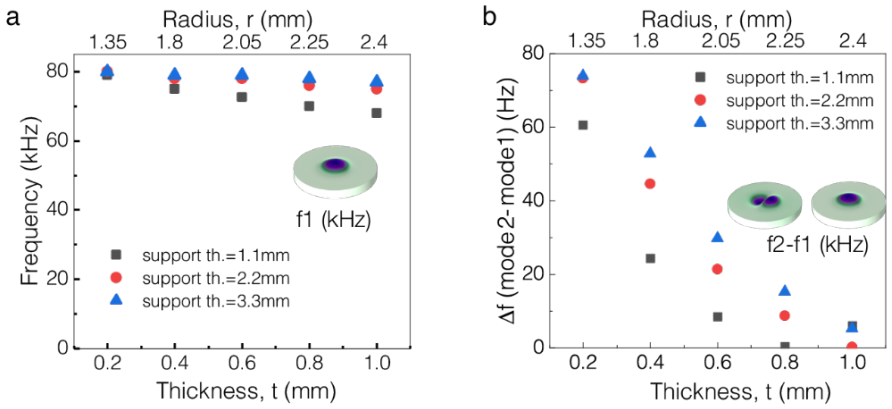

Figure S2.10: Effect of clamping support thickness on the resonant frequency of the transducers with different thickness and radii (a) Effect of support thickness on first resonant frequency of transducers (f1) with different thickness of the membrane (b) Difference between the resonant frequency of second mode (f2) and first mode (f1) for different thickness and the effect of support thickness on this difference in frequencies (f2-f1).

Here, we study the impact of the clamping structure on the resonant frequency of the transducers by varying the support thickness and analysing the resulting frequency using COMSOL simulations. As mentioned before, specific combinations of thickness and radius (t, r) were selected to maintain a nearly constant frequency, ensuring that frequency variations did not affect the output pressure.

In **Figure S2.10a,** the effect of support thickness on the first mode resonant frequency, f1 of the selected transducers is depicted. The findings revealed that for a support thickness of 1x (1.1 mm), an increase in membrane thickness led to a decrease in resonant frequency. However, doubling or tripling the support thickness, indicated by the data points at 2.2 mm and 3.3 mm, respectively, resulted in sustained high resonant frequencies without decline. This observation indicates that when the transducer resonates with a relatively small support structure (1.1 mm) compared to its thickness (1 mm), the resonant frequency decreases, suggesting insufficient stiffness or imperfect clamping of the support structure. This effect is particularly prominent in thicker transducers due to the higher stiffness of the membrane compared to the clamping structure. The study aimed to mimic the imperfect clamping observed in the experimental setup where transducers are affixed with copper tape. Although the simulations assume perfect

bonding between the bottom surface and clamping, they offer insights into how structural stiffness can influence the resonant frequency.

Figure S2.10b illustrates the effect of membrane thickness on the difference between the second and first-mode resonant frequencies (f2-f1). The graph indicates that increasing membrane thickness (t) while maintaining a constant support thickness (1.1 mm) significantly reduces the difference between the frequencies of the two modes, as evident with the Δf for increasing t (black square points). The fundamental out-of-plane mode is the most efficient at generating sound due to the membrane acting as a monopole source. This shows that for larger thicknesses, the second mode, which is not very efficient at generating sound, becomes activated at lower frequencies, closer to the fundamental out-of-plane mode. Consequently, there is reduced efficiency in sound generation. However, the difference (f2-f1) also depends on the support thickness, with increasing support thickness and clamping efficiency resulting in a larger difference between the frequencies (f2-f1). This implies that thicker support structures are necessary for thicker membranes to efficiently allow sound generation by only activating the out-of-plane mode.

2.A.10. SOUND PRESSURE MEASUREMENT

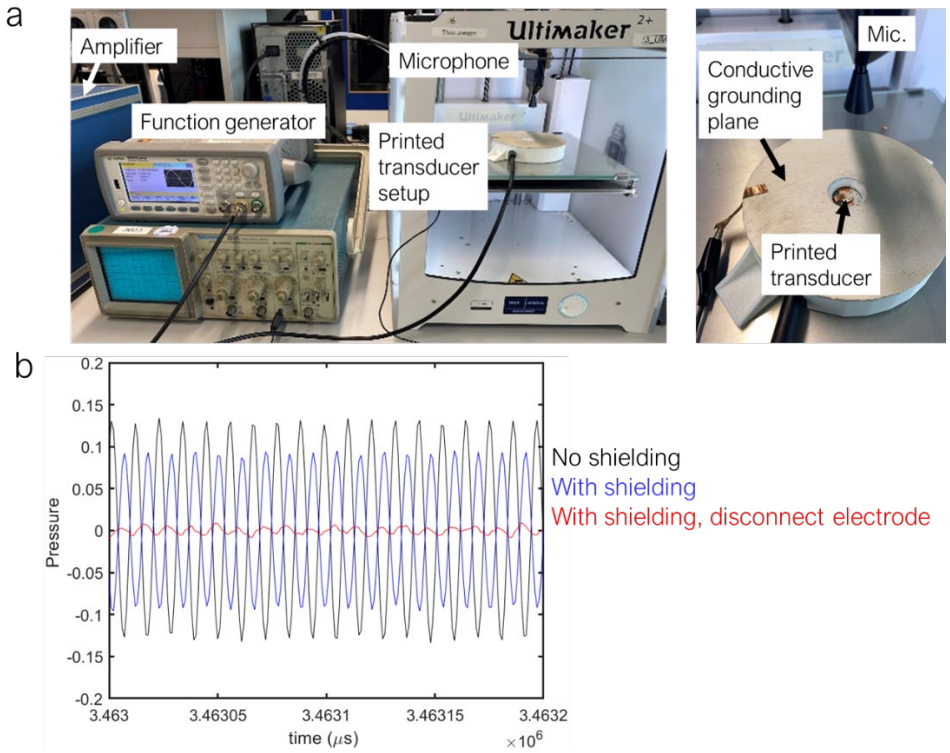

Figure S2.11: Sound pressure measurement setup and effect of electromagnetic shielding. (a) Setup for sound pressure measurement: An input voltage sine wave, with a frequency determined from LDV measurements, was generated by a function generator, amplified, and sent to the printed transducer. Sound pressure was measured by a microphone attached to the printer head. A conducting grounding plane made of a 3D printed casing, coated with conducting silver paste, reduced electromagnetic coupling between transducer wires and the microphone. (b) Effect of electromagnetic shielding: The graph shows output pressure with and without shielding. Shielding caused a slight drop in pressure. When voltage was ON, but electrodes were disconnected, the received signal was almost negligible (red), indicating that any electromagnetic coupling from the wires from the high input voltage was minimised and only acoustic pressure was being measured.

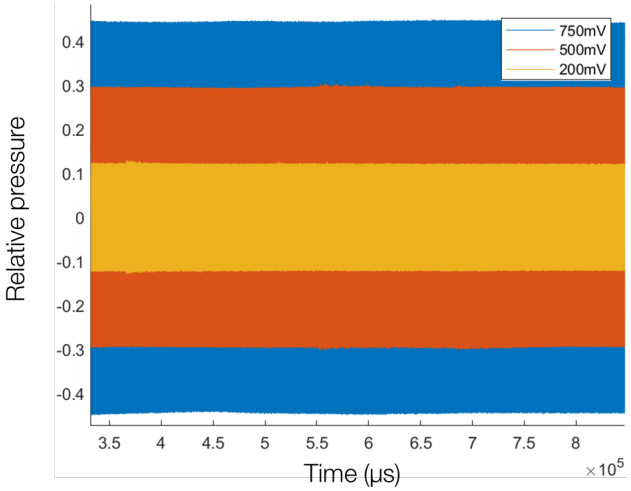

Figure S2.12: Calibration of the ultrasound microphone M500 using a reference Murata 40kHz transducer. The output pressure for different input voltages was measured and then used to calculate for the standard value of 10V rms.

Input voltage (mV)	Relative pressure reading from microphone- SPL	SPL/mV
200	0.12	6,00E-04
500	0.3	6,00E-04
750	0.45	6,00E-04
10000 (10V)	6 (Estimated)	6,00E-04

We utilised the M500 USB Ultrasound Microphone, which provided us with relative pressure values, which we then calibrated using a reference Murata 40 kHz ultrasound transducer with a known output sound pressure. The reference Murata transducer, positioned at a distance of 30 cm, has a documented SPL of 120 dB, corresponding to 20Pa at a 10V rms input.

As the M500 Ultrasound Microphone has a saturation limit, we were unable to measure the output of the 10V rms input directly. Consequently, we measured SPL values from the reference Murata transducer, positioned at a distance of 30 cm across various voltages from 200 to 750 mV, which we observed increased linearly as shown in **Figure S2.12**. Then, we extrapolated the Y-axis values to estimate the SPL at 10 V-rms. For calibration, we then compared it to the absolute SPL values outlined in the microphone's datasheet. Our measurements of pressure, as indicated in the table, allowed us to extrapolate that the y-axis value at 10V rms

would be 6, corresponding to a pressure of 20 Pa according to the datasheet. Thus, the y-axis calibration was determined to be 3.33 Pa per unit.

2.A.11. DISTANCE MEASUREMENT

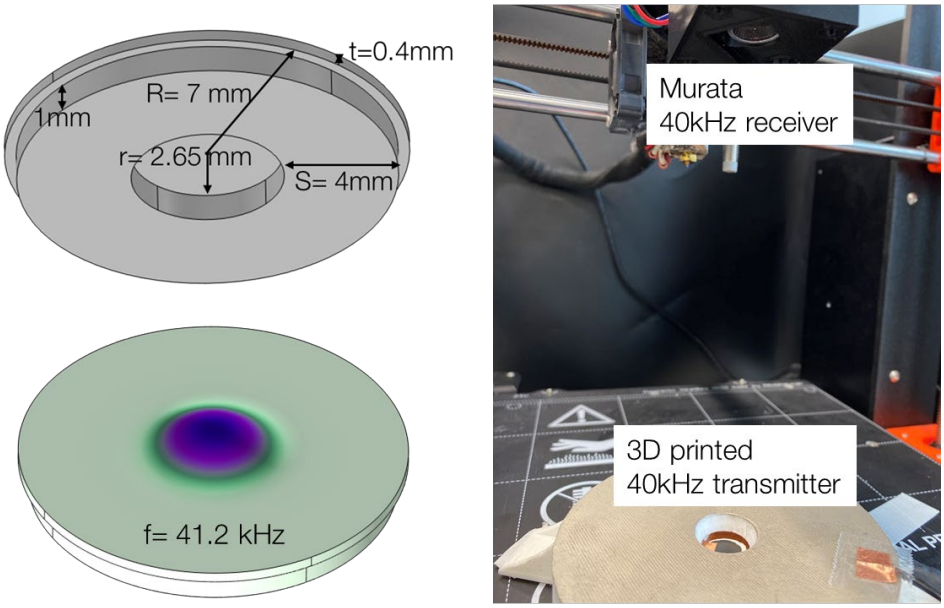

Figure S2.13: Design of a 40kHz printed transducer comprising a piezoelectric membrane with a thickness (t) of 0.4 mm and an inner radius (r) of 2.65 mm. The support thickness was selected to be 4 mm, and the total radius of the piezo membrane (R) was set at 7 mm. The fundamental mode frequency of this transducer was simulated to be 41kHz. Subsequently, it was manufactured and utilised as a transmitter with a commercial 40 kHz receiver, as depicted.

2.6. REFERENCES:

[1] K. Harrington, D. R. Large, G. Burnett, O. Georgiou, *Proc. - 10th Int. ACM Conf. Automot. User Interfaces Interact. Veh. Appl. AutomotiveUI 2018* **2018**, 11.

[2] J. Yan, X. Yang, X. Sun, Z. Chen, H. Liu, *IEEE Sens. J.* **2019**, *19*, 5895.

[3] G. Gibbs, H. Jia, I. Madani, *Transp. Res. Procedia* **2017**, *28*, 173.

[4] G.-L. Luo, Y. Kusano, D. A. Horsley, *J. Microelectromechanical Syst.* **2021**, *30*, 81.

[5] M. A. Skylar-Scott, J. Mueller, C. W. Visser, J. A. Lewis, *Nature* **2019**, *575*, 330.

[6] M. Wehner, R. L. Truby, D. J. Fitzgerald, B. Mosadegh, G. M. Whitesides, J. A. Lewis, R. J. Wood, *Nature* **2016**, *536*, 451.

[7] A. D. Valentine, T. A. Busbee, J. W. Boley, J. R. Raney, A. Chortos, A. Kotikian, J. D. Berrigan, M. F. Durstock, J. A. Lewis, *Adv. Mater.* **2017**, *29*, 1703817.

[8] J. T. Muth, D. M. Vogt, R. L. Truby, Y. Mengüç, D. B. Kolesky, R. J. Wood, J. A. Lewis, *Adv. Mater.* **2014**, *26*, 6307.

[9] Y. Zeng, L. Jiang, Y. Sun, Y. Yang, Y. Quan, S. Wei, G. Lu, R. Li, J. Rong, Y. Chen, Q. Zhou, *Micromachines* **2020**, *11*, 713.

[10] H. Lu, H. Cui, G. Lu, L. Jiang, R. Hensleigh, Y. Zeng, A. Rayes, M. K. Panduranga, M. Acharya, Z. Wang, A. Irimia, F. Wu, G. P. Carman, J. M. Morales, S. Putterman, L. W. Martin, Q. Zhou, X. (Rayne) Zheng, *Nat. Commun. 2023 141* **2023**, *14*, 1.

[11] J. E. Smay, J. Cesarano, B. A. Tuttle, J. A. Lewis, *J. Am. Ceram. Soc.* **2004**, *87*, 293.

[12] S. Bodkhe, G. Turcot, F. P. Gosselin, D. Therriault, *ACS Appl. Mater. Interfaces* **2017**, *9*, 20833.

[13] J. Holterman, P. Groen, *An Introduction to Piezoelectric Materials and Applications*, Stichting Applied Piezo, **2013**.

[14] T. Yamada, T. Ueda, T. Kitayama, *J. Appl. Phys.* **1982**, *53*, 4328.

[15] R. Tao, J. Shi, F. Granier, M. Moeini, A. Akbarzadeh, D. Therriault, *Appl. Mater. Today* **2022**, *29*, 101596.

[16] Z. M. Tsikriteas, R. A. Heylen, S. Jindal, E. Mancuso, Z. Li, H. Khanbareh, *Adv. Mater. Technol.* **2023**, *8*, 2202127.

[17] Y. Saito, H. Takao, T. Tani, T. Nonoyama, K. Takatori, T. Homma, T. Nagaya, M. Nakamura, *Nature* **2004**, *432*, 84.

[18] N. H. Gaukås, Q. S. Huynh, A. A. Pratap, M. A. Einarsrud, T. Grande, R. M. D. Holsinger, J. Glaum, *ACS Appl. Bio Mater.* **2020**, *3*, 8714.

[19] D. B. Deutz, N. T. Mascarenhas, J. B. J. Schelen, D. M. de Leeuw, S. van der Zwaag, P. Groen, *Adv. Funct. Mater.* **2017**, *27*, 1700728.

[20] V. Stuber, D. Deutz, J. Bennett, D. Cannell, D. de Leeuw, S. van der Zwaag, P. Groen, *Energy Technol.* **2018**, DOI 10.1002/ente.201800419.

[21] R. G. Larson, *The Structure and Reology of Complex Fluids*, Oxford University Press, New York, **1999**.

[22] G. Tarì, J. M. F. Ferreira, A. T. Fonseca, O. Lyckfeldt, *J. Eur. Ceram. Soc.* **1998**, *18*, 249.
[23] V. L. Stuber, T. R. Mahon, S. van der Zwaag, P. Groen, *Mater. Res. Express* **2020**, *7*, 015703.
[24] C. M. Wang, J. N. Reddy, K. H. Lee, *Shear Deform. Beams Plates* **2000**, 11.
[25] Siemens, "Sound Fields: Free versus Diffuse Field, Near versus Far Field," Available https://community.sw.siemens.com/s/article/sound-fields-free-versus-diffuse-field-near-versus-far-field, **2020**.
[26] N. K. James, D. B. Deutz, R. K. Bose, S. van der Zwaag, P. Groen, *J. Am. Ceram. Soc.* **2016**, *99*, 3957.
[27] N. Kleger, M. Cihova, K. Masania, A. R. Studart, J. F. Löffler, *Adv. Mater.* **2019**, *31*, 1903783.
[28] Y. Saito, H. Takao, *Ferroelectrics* **2006**, *338*, 17.
[29] A. J. Kinloch, K. Masania, A. C. Taylor, S. Sprenger, D. Egan, *J. Mater. Sci.* **2008**, *43*, 1151.
[30] K. Tsuji, Z. Fan, S. H. Bang, S. Dursun, S. Trolier-McKinstry, C. A. Randall, *J. Eur. Ceram. Soc.* **2022**, *42*, 105.

3

TAILORABLE PIEZOELECTRICITY THROUGH ML-BASED INVERSE DESIGN AND 3D-PRINTING OF ARCHITECTED MATERIALS

In the development of active animate materials, electromechanical coupling is highly attractive to realize mechanoresponsive functionality. Piezoelectricity is the most utilized electromechanical phenomenon due to the wide availability of materials that display precise and reliable coupling. However, the inherent directionality of these materials is constrained by the symmetry of their crystal structure, which limits the choice of available properties in natural piezoelectric materials. A solution to alleviate this limitation could be to leverage geometry or architecture at the mesoscale. Here, we present an integrated framework for designing and 3D-printing piezoelectric truss metamaterials with customizable anisotropic responses. To explore the vast design space of truss metamaterials, we employ generative machine learning to optimize the topology and geometry of truss lattices and achieve target piezoelectric responses. Then, we develop an in-gel-3D printing method to fabricate polymer-ceramic piezoelectric truss metamaterial structures using a composite slurry of photo-curable resin and lead-free piezoelectric particles. The ML framework discovers designs exhibiting unconventional behaviours, including auxetic, unidirectional, and omnidirectional piezoelectricity, while the additive manufacturing technique ensures shaping freedom and precision in fabricating these metamaterials at small scales. Our results show an improvement of over 48% in the specific hydrostatic figure of merit in optimized metamaterials over bulk lead zirconate titanate (PZT). We successfully achieved metamaterials with higher transverse piezoelectric coupling coefficient than its longitudinal coefficient, which is a phenomenon that is rare in bulk materials. Our approach enables customizable piezoelectric responses and paves the way towards the development of a new generation of electro-active animate materials.

This chapter has been submitted as S. Sharma*, S.K. Ammu*, P.Thakolkaran, J. Jovanova, K. Masania, S. Kumar, “Tailorable piezoelectricity through ML-based inverse design and 3D-printing of architected materials”. (*equal contribution)

3.1. INTRODUCTION

Piezoelectric materials demonstrate a separation of positive and negative charge centres at the atomic scale in response to mechanical deformation, which facilitates the two-way coupling between mechanical and electrical energies. This makes them an indispensable component in a wide range of engineering applications across domains, such as biomedical[1–3], aerospace[4,5], electronics[6,7], building structures[8,9], and electro-chemistry[10]. The search for superior piezoelectric properties has been a topic of high interest among the scientific community. Yet, the progress has been primarily restricted to improving the performance of existing piezoelectric materials by either material synthesis-based methods[11–15] or macro-scale design and optimization methods[16–18]. With the advent of technologies such as micro and nanoelectromechanical systems (MEMS and NEMS) and micro-robotics, the need for exotic and tunable electromechanically responsive systems is pushing the limits of functionalities beyond what current materials can offer. The primary restricting factor for the range of piezoelectric response in conventional piezoelectric materials is their crystal symmetry, which dictates the directionality of electromechanical coupling.

The piezoelectric coupling correlates six mechanical stresses or strains to the three electric field components. This correlation is defined by the piezoelectric tensor which has 18 unique coefficients correlating the electrical and mechanical state variables. Commonly used piezoelectric materials such as dielectric ceramics, e.g., lead zirconate titanate (PZT), $BaTiO_3$ (BT), PMN-PT, and polymers, e.g., polyvinylidene fluoride (PVDF) have only five non-zero piezoelectric coefficients, due to their crystal symmetry. These coefficients have fixed signs (positive or negative) which cannot readily be flipped. This makes certain desirable functionalities in piezoelectric materials rare. For example, the phenomenon of negative piezoelectricity, capable of generating compression in response to a positive electric field, has only been observed in PVDF and its co-polymers[19]. In addition to the individual coefficients, several of their desirable combinations are unavailable in conventional materials, such as observing piezoelectric response only in a particular direction and eliminating the noise signal from the other directions [20,21]. Thus, realizing the full anisotropic design space of piezoelectric materials could be beneficial for several applications and warrants the development of an effective design and fabrication route.

While changing or designing the arrangement of ions in the material crystals may not be physically feasible to achieve tailorable properties, it is possible to design

the architecture of the material at a mesoscale. In this context, the concept of metamaterials, also known as architected materials, emerges as a promising way to design for tailored piezoelectric properties. Metamaterials are constructed by tessellations of periodic or aperiodic unit cells large enough to be manufacturable yet small enough to constitute a pseudo-homogeneous response at the macro scale. One notable class of these metamaterials is beam-based truss metamaterials (constructed by a spatial arrangement of connected struts), which have been shown to be extremely light-weight and mechanically strong[22–24].

The architecture of a truss metamaterial is defined by the combination of the geometry and topology of the unit cells, where the geometry means the position of the junctions or nodes of the struts, and topology is the connectivity of these nodes. While truss metamaterials have been vastly explored for exotic and tunable mechanical properties[23–29], the design and fabrication of piezoelectric metamaterials still remain challenging. Notably, Cui et al. have demonstrated the tailorable response of architected piezoelectric metamaterials and their applications in designing robotic metamaterials[30,31]. However, the design process has remained either ad-hoc or based on a simple parametrization of a small design space. The main challenge is that of inverse design, i.e., exploration of the infinitely large number of possible designs to discover the ones with desirable properties.

Although the inverse design problem has been tackled in mechanical metamaterials[22,23], for piezoelectric materials, it becomes more complicated due to multiphysics coupling and poling orientation dependence of piezoelectric properties. To solve this challenge, we propose a generative machine learning (ML) approach for designing the piezoelectric response in architected materials. We use two distinct descriptions of the truss metamaterials, where one provides diverse piezoelectric responses while the other facilitates a broad range of properties and better manufacturability. The design-property pairs of these truss metamaterials are used to train the ML framework, which can generate designs corresponding to desired properties. Having established the design framework, we further address the next major challenge in the development of piezoelectric metamaterials, which is their fabrication.

Additive manufacturing techniques, such as stereolithography (SLA), digital light processing (DLP), and fused filament deposition (FFF), offer great freedom in fabricating a broad range of topologies. Doing so with piezoelectric materials is challenging for several reasons, such as the requirement of high-temperature processing in ceramics and lower piezoelectricity in polymers, low mechanical

integrity due to their brittleness, and the requirement of poling post-manufacturing. Printing polymer-ceramic piezoelectric composites with a photo-curable resin ink infused with piezoelectric particles has been shown recently for manufacturing spinodoid topologies with bi-continuous features[32]. This approach requires high precision to manufacture slender structural members of low relative density metamaterials, such as those based on truss architectures. Moreover, their printing requires recoating of the printing ink for each layer due to the necessary high particle loading, which leads to excess material usage and a cost-intensive setup[30,32]. Another difficulty in achieving continuous SLA/ DLP printing with piezoelectric inks arises from the contrast in optical and rheological properties of the piezoelectric particles and photo-curable resins. Direct ink writing (DIW) offers a better approach for this purpose, where composite inks can be extruded to print shapes in 3D space[33]. This approach has been shown to be effective by Tao et al.[34] for printing piezoelectric materials with relatively simpler shapes. However, sustaining the accurate shape and ensuring connectivity becomes challenging when the whole structure cannot be printed continuously, such as the truss structures we propose.

To achieve this, we develop an in-gel 3D printing technique to enable the additive manufacturing of piezoelectric truss metamaterials. A photosensitive resin-based ink infused with piezoelectric nanoparticles is synthesized and used to extrude the desired shapes. With an optimized print path and rheology, the printing technique enables connectivity of the struts while the shape accuracy is preserved due to structural support provided by the gel. Our inverse design framework, combined with the developed 3D printing methodology, could successfully design and fabricate unique piezoelectric metamaterials with tunable piezoelectric response. For example, we designed metamaterial unit cells with maximized hydrostatic figure of merit, transverse piezoelectric coefficient higher than longitudinal, auxetic piezoelectric response, and selective piezoelectric coefficients.

3.2. RESULTS AND DISCUSSION

3.2.1. PIEZOELECTRIC TRUSS METAMATERIALS

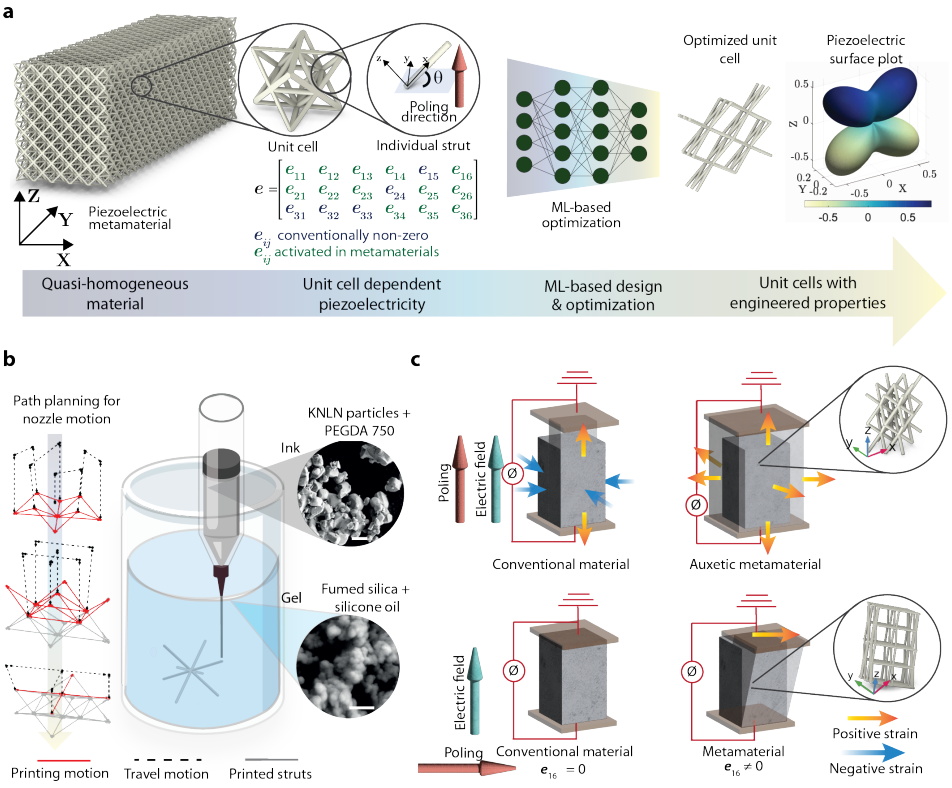

Figure 3.1. Concept of piezoelectric truss metamaterials for tailoring the electromechanical behaviour. (a) Illustration of a piezoelectric metamaterial made by tessellating octet unit cells in three orthogonal directions. The different levels of structural features are shown in the insets. These mesoscale features can be tuned to selectively activate different components of the piezoelectric property matrix, in contrast to the only five non-zero coefficients in most of the common piezoelectric materials. ML is then used to design unit cells with desired properties, represented by the piezoelectric surface plot on the right. (b) Path planning followed by in-gel printing of the designed metamaterials. The piezoelectric composite ink is made of KNLN particles and PEGDA 700 matrix, as shown in the inset (scale bar 2 μm). The ink is then extruded in a support gel made of fumed silica and silicone oil (scale bar 200 nm). (c) Examples of piezoelectric metamaterials made by the truss unit cells exhibiting behaviours not readily available in conventional materials. The first example (top) shows the auxetic behaviour of a truss metamaterial. While conventional materials, under an applied electric field in the poling direction, expand in the direction of the electric field and contract along the two normal directions, the metamaterial made of the auxetic unit cell expands in all three directions. The second example (bottom) shows a metamaterial with a non-zero e_{16} coefficient, exhibiting shear deformation in response to an electric field applied in direction 1.

The homogenized properties of truss metamaterials at the macro scale depend on the topology and the geometry of the unit cells. In the case of piezoelectric metamaterials, the orientation dependence of the piezoelectric property tensor of individual struts also becomes important. **Figure 3.1** demonstrates the concept of architected piezoelectric materials. The inclination of the individual struts activates multiple modes of piezoelectricity simultaneously, as demonstrated in **Figure 3.1a.**

We define a global coordinate system (X, Y, Z) and a local coordinate system for individual struts (x, y, z) where x-axis aligns with the length of the strut (Supporting Information **Figure S1**). The two-level orientation dependence of the piezoelectric tensor arises from the fact that the piezoelectric tensor is defined with reference to the poling direction, which is parallel to the global Z axis. As the orientation of the individual struts with respect to the poling direction can be different, the piezoelectric coefficients can have different values for individual struts, which contributes to the complexity of the design-property relationship.

The two most common forms of constitutive equations of piezoelectricity, namely strain-charge and stress-charge forms, are written as

$$\epsilon_{\{ij\}} = S_{\{ijkl\}^{E\sigma}_{\{kl\}}} + d_{\{ijk\}E_k} \tag{1}$$

$$D_i = d_{\{ijk\}\sigma_{\{jk\}}} + \kappa_{\{ik\}^{TE}_{k}}$$

and,

$$\sigma_{\{ij\}} = C_{\{ijkl\}^{E\epsilon}_{\{kl\}}} - e_{\{ijk\}^{TE}_{k}} \tag{2}$$

$$D_i = e_{\{ijk\}\epsilon_{\{jk\}}} + \kappa_{\{ik\}}E_k$$

Here ϵ_{ij} and σ_{ij} denote the mechanical strain and stress tensors, and the electric field and electric displacement vectors are designated as E_k and D_k. C_{ijkl}, e_{ijk}, d_{ijk} and κ_{ik} denote mechanical stiffness, piezoelectric coupling coefficients in stress charge and strain charge forms, and dielectric permittivity of the material. The indices i, j, k, $l \in \{1,2,3\}$, while the superscripts $(\cdot)^E$, $(\cdot)^\sigma$, and $(\cdot)^\epsilon$ indicate the properties measured at a constant electric field, stress, and strain, which are omitted hereafter for the sake of brevity. To concur with the finite element framework used for homogenization, the stress-charge form of piezoelectricity (**Equation 2**) is used. Theoretically, it has been shown that the piezoelectric tensor

can be tuned by controlling the direction of poling of the material[35]. We apply poling along the global Z axis, so the effective piezoelectric coefficient in the local (x,y,z) coordinate system of a beam, denoted by e' can be computed as (Equation 3)

$$e'_{pqr} = R_{pi}R_{qj}R_{rk}e^{\text{base}}_{ijk} \tag{3}$$

Here, e^{base}_{ijk} are the components of the piezoelectric tensor of the base material, $\mathbf{R} \in$ SO(3) is the rotation matrix (see **SI Equation 2**) containing the direction cosines of the local coordinate axes (x, y, z), with respect to global coordinate axes (X, Y, Z). Exploiting the symmetry of stress and strain components (e.g., $\sigma_{ij} = \sigma_{ji}$), The stress charge equation can be simplified and written in matrix form as (Equation 4)

$$\begin{bmatrix} \sigma_{11} \\ \sigma_{22} \\ \sigma_{33} \\ \sigma_{23} \\ \sigma_{31} \\ \sigma_{12} \\ D_1 \\ D_2 \\ D_3 \end{bmatrix} = \begin{bmatrix} C_{11} & C_{12} & C_{13} & C_{14} & C_{15} & C_{16} & -e_{11} & -e_{21} & -e_{31} \\ C_{21} & C_{22} & C_{23} & C_{24} & C_{25} & C_{26} & -e_{12} & -e_{22} & -e_{32} \\ C_{31} & C_{32} & C_{33} & C_{34} & C_{35} & C_{36} & -e_{13} & -e_{23} & -e_{33} \\ C_{41} & C_{42} & C_{43} & C_{44} & C_{45} & C_{46} & -e_{14} & -e_{24} & -e_{34} \\ C_{51} & C_{52} & C_{53} & C_{54} & C_{55} & C_{56} & -e_{15} & -e_{25} & -e_{35} \\ C_{61} & C_{62} & C_{63} & C_{64} & C_{65} & C_{66} & -e_{16} & -e_{26} & -e_{36} \\ e_{11} & e_{12} & e_{13} & e_{14} & e_{15} & e_{16} & \kappa_{11} & \kappa_{12} & \kappa_{13} \\ e_{21} & e_{22} & e_{23} & e_{24} & e_{25} & e_{26} & \kappa_{21} & \kappa_{22} & \kappa_{23} \\ e_{31} & e_{32} & e_{33} & e_{34} & e_{35} & e_{36} & \kappa_{31} & \kappa_{32} & \kappa_{33} \end{bmatrix} \begin{bmatrix} \varepsilon_{11} \\ \varepsilon_{22} \\ \varepsilon_{33} \\ 2\varepsilon_{23} \\ 2\varepsilon_{31} \\ 2\varepsilon_{12} \\ E_1 \\ E_2 \\ E_3 \end{bmatrix} \tag{4}$$

In the above equation, the 18 unique coefficients of the piezoelectric tensor are written in the form of a 3×8 piezoelectric matrix, which will be used hereafter to denote the piezoelectric property space. The conversion of piezoelectric coefficients from stress-charge to strain-charge and vice versa are shown in **SI Equation 5**. The effective electrical, mechanical, and electromechanical properties of a unit cell defined by its geometry and topology are computed using a finite element-based homogenization with periodic boundary conditions, as explained in the **SI Section 1**. However, a method to discover the geometry and topology of the unit cells corresponding to desired properties is needed to achieve a tailored piezoelectric response. Next, we develop an ML-based design methodology to achieve this.

3.2.2. ML-BASED OPTIMIZATION FOR TAILORED PIEZOELECTRICITY

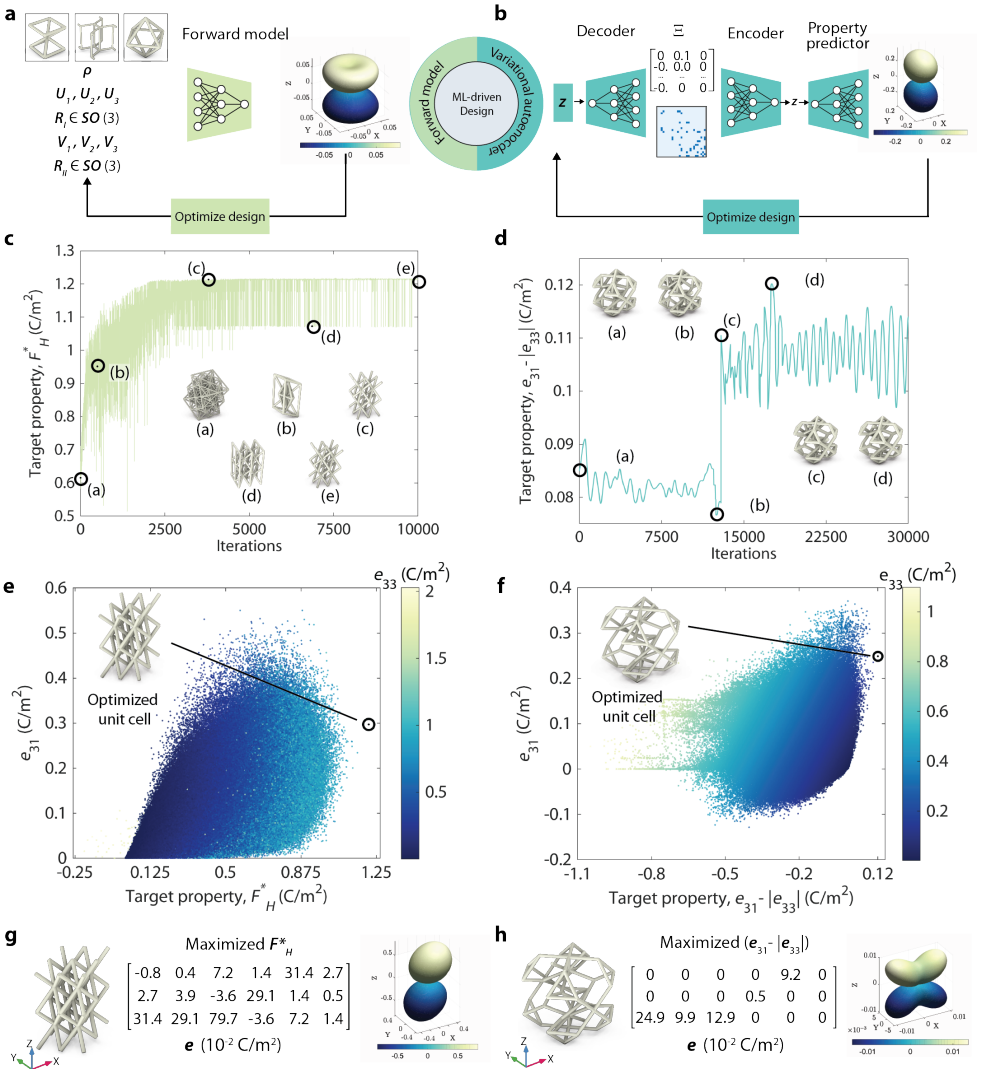

Figure 3.2. ML-based optimization of piezoelectric metamaterials. (a) The optimization framework employed for the design space I. A pre-trained forward neural network (NN) is used to perform gradient-based optimization. (b) The variational autoencoder (VAE) architecture employed to perform optimization in the lower-dimensional and continuous latent space for design space II. The additional encoding-decoding step is performed to ensure the validity of the predicted designs. The trace followed during the optimization, and different designs traversed during the path for (c) Dataset I and (d) Dataset II. (e) The e_{31} vs.target property F_H^* for dataset I, and (f) the e_{31} vs.target property ($e_{31} - |e_{33}|$) landscape for dataset II. In both cases, the achieved optimized lattices, marked by the black circles, lie beyond the dataset and demonstrate the extrapolatory capability of the optimization framework. (g) An example

optimized unit cell is shown, where the hydrostatic figure of merit F_H^* is maximized. (h) An example optimized lattice with the optimization objective to maximize ($e_{31} - |e_{33}|$).

Truss metamaterials offer great tunability of physical properties due to virtually infinite possible topologies and geometries. This comes at the cost of higher complexity in the design space and makes design and optimization difficult. The parameterization of these truss metamaterials is often discrete and high-dimensional. The complexity is further enhanced by the thin features, which makes traditional optimization methods computationally expensive to implement for inverse designing to achieve desired properties. We explore the vast and highly complex design space of truss metamaterials and their respective piezoelectric properties by selecting two fundamentally different design spaces, each with its own advantages. These design spaces were originally developed for mechanical metamaterials and were used to train inverse design models for designing elastic properties[22,23]. We adapt these design spaces and develop the optimization framework for designing the piezoelectric behaviour of truss metamaterials. The first design space, based on geometric transformations, provides a broader range of piezoelectric responses and can activate all 18 piezoelectric coefficients. However, these geometric transformations lead to aspect ratios and rotations that are unfavourable for manufacturing. The second design space is restricted to a cubic symmetry and thus can only activate the five already non-zero coefficients of the base materials, with a broader range of values and improved manufacturability compared to the first design space. In the following, we present two different ML frameworks to suit the nature of the parameterizations and efficiently optimize in these design spaces.

Design space I: The first design space, introduced by Bastek et al.[22] which was originally inspired by Zok et al.[36] is based on the superposition of a small set of elementary unit cells, which are subsequently stretched and rotated twice to get the final unit cell. Each unit cell is described by the following design parameters: *(i)* three elementary unit cells $L_1, L_2, L_3 \in \{1, \dots, 7\}$ chosen out of 7 options, *(ii)* their respective tessellations $t_1, t_2, t_3 \in \{1,2\}$ (i.e., each cell tessellated as $1 \times 1 \times 1$ or $2 \times 2 \times 2$) following which they are superposed, *(iii)* the eigenvalues $U_1, U_2, U_3 > 0$ of the first affine stretch tensor $\mathbf{U} = \mathrm{diag}(U_1, U_2, U_3)$, *(iv)* the first rotation tensor $\mathbf{R}_I \in \mathrm{SO}(3)$, *(v)* the eigenvalues $V_1, V_2, V_3 > 0$ of the second affine stretch tensor $\mathbf{V} = \mathrm{diag}(V_1, V_2, V_3)$, *(vi)* the second rotation tensor $\mathbf{R}_{II} \in \mathrm{SO}(3)$, and lastly, *(vii)* the relative density ρ of the final unit cell achieved by choosing uniform diameter struts. The rotation tensors are defined by three unique parameters in axis-angle

representation. Thus each truss lattice is defined by the set of design parameters $\Theta = \{L_1, L_2, L_3, t_1, t_2, t_3, U_1, U_2, U_3, \mathbf{R}_I, V_1, V_2, V_3, \mathbf{R}_{II}, \rho\}$. Three example unit cells generated using this parametrization and their corresponding parameters are shown in **Figure S3a**. Using this approach, one can obtain 262 unique topologies and virtually infinite designs. We used a set of $3{,}000{,}000$ unit cell designs generated with this parametrization and performed numerical homogenization to obtain the pairs of unit cell designs and piezoelectric properties. Due to the rotation and stretching, we observe that all 18 components of the effective piezoelectric matrix $\mathbf{e}$ are activated. Further, we note that certain components correlate highly with others (see Section 3 of the Supporting Information).

We train a forward model $\mathcal{F}_\omega: \Theta \rightarrow \mathbf{e}$ based on a neural network (NN) that maps both geometric and topological design parameters Θ of the truss lattices to the effective piezoelectric matrix $\mathbf{e}$. Here, ω denotes the trainable parameters (weights and biases) of the NN architecture. We use a multi-layer perceptron (MLP) architecture for the NN; see Supporting Information Section 2 for details. In Supporting Information **Figure S2a**, we illustrate the prediction performance of the forward model with parity plots.

Once trained, the forward model can be used as a surrogate structure-property map for design optimizations, as shown in **Figure3.2a**. Here, we demonstrate this capability by designing a truss metamaterial with maximal hydrostatic figure of merit F_H,

$$F_H[\mathbf{e}] = e_{31} + e_{32} + e_{33} \tag{5}$$

which quantifies the energy harvesting performance of a piezoelectric material under hydrostatic pressure, with higher being better. For converse piezoelectricity (actuation), F_H signifies the volumetric expansion under an electric field in direction 3. Since in most piezoelectric materials, e_{33} is positive while e_{31} and e_{32} are negative, very low magnitudes of F_H are observed, leading to poor performance. To achieve an improved F_H, we formalize the design optimization problem as (Equation 6):

$$\Theta^* \leftarrow \quad \arg\max_\Theta F_H^*[\mathbf{e}], \qquad \text{with} \quad \mathbf{e} = \mathcal{F}_\omega(\Theta) \quad \text{and}$$

$$F_H^*[\mathbf{e}] = F_H[\mathbf{e}] - \lambda_1\underbrace{((e_{31}-e_{32})^2+(e_{31}-e_{33})^2+(e_{32}-e_{33})^2)}_{\text{magnitude regularization}} - \lambda_2\underbrace{\left(\sum_{i=1}^{6} e_{1i}^2+\sum_{i=1}^{6} e_{2i}^2+\sum_{i=4}^{6} e_{3i}^2\right)}_{\text{shrinkage regularization}} \quad (6)$$

where Θ^* is the set of optimized design parameters. The second term with scaling hyperparameter $\lambda_1 > 0$ aids in regularizing the magnitudes of all three components so that we can achieve close-to-uniform volumetric expansion. The third term with scaling hyperparameter $\lambda_2 > 0$ serves as a shrinkage regularization to prevent distortions such as shear during actuation. To avoid extreme aspect ratios and improve the manufacturability of the optimized designs, we constrained the optimization process such that the stretch values $\mathbf{U}$ and $\mathbf{V}$ are scaled down by a factor of $\alpha \in (0,1]$. The problem in Equation 6 is solved numerically using gradient-based optimization, with Adam optimizer. All hyperparameters, training, and optimization protocols can be found in the SI Section 2.

Figure3.2c shows the trace followed by the optimization framework, along with example lattices for different checkpoints. The categorical parameters related to topology lead to fluctuations in the unit cell designs and, consequently, the target property. **Figure3.2e** shows the distribution of the dataset in the e_{31} vs. regularized figure of merit F_H^* landscape. The optimized lattice lies outside the dataset, demonstrating the extrapolatory capability of the optimization and ML framework. Additional examples of tailored piezoelectricity are presented in the SI Section 4, **Figure S6**, which demonstrate the unconventional behaviors of full anisotropy and unidirectionality of piezoelectricity.

Design space II: The second design space, introduced by Zheng et al.[23], is based on a more general approach of generating highly complex unit cells with cubic symmetry. Each unit cell is created with a fixed set of virtual nodes, which can be offset freely along specific degrees of freedom, and the nodes are activated by connecting them to other nodes. Although the generated unit cells are of orthotropic nature, a vast range of stiffness values and orthotropic anisotropy can be achieved. Analogously, the design space is virtually infinite geometrically with at least millions of unique topologies if not more. Each unit cell is constructed by designing the lattice within the octant of a unit cube, which is then mirrored to obtain the unit cell with cubic symmetry and periodic tilability. There are 27 virtual nodes in the octant, i.e., 8 vertex nodes $\{\mathbb{V}_1, \mathbb{V}_2, \mathbb{V}_3, \mathbb{V}_4, \mathbb{V}_5, \mathbb{V}_6, \mathbb{V}_7, \mathbb{V}_8\}$, 12 edge

nodes $\{E_1, E_2, E_3, E_4, E_5, E_6, E_7, E_8, E_9, E_{10}, E_{11}, E_{12}\}$, 6 face nodes $\{F_1, F_2, F_3, F_4, F_5, F_6\}$, and one body node $\{T_1\}$. While the vertex nodes remain fixed, the edge nodes, face nodes, and body node can move freely on the corresponding edge, face, and inside of the octant, respectively. These node offsets are represented vectorially as $\mathbf{x} \in \mathbb{R}^{27\times3}$. The connectivity is represented by a 27×27 adjacency matrix $\mathbf{A} \in \{0,1\}^{27\times27}$. For $i \neq j$, the entry $A_{ij} = 1$ if nodes i and j are connected by a strut, and $A_{ij} = 0$ otherwise. Diagonal entries follow the rule: $A_{ii} = 1$ if node i is part of the topology, and $A_{ii} = 0$ if it does not exist. A truss lattice is then uniquely defined by the graph $\Xi = (\mathbf{A}, \mathbf{x})$. **Figure S3b** shows three example unit cells generated with this parametrization. Similar to the first design space, we homogenized a set of 965,685 truss metamaterial designs and obtained their piezoelectric properties.

However, unlike the first design space, the graph-based representations are extremely discontinuous, high-dimensional, and combinatorial. To unify the discrete designs, the variational autoencoder (VAE) framework of Zheng et al.[23] is employed. The VAE consists of two neural networks. An *encoder* $\mathcal{E}_\phi$, with trainable parameters ϕ, maps the graph of a truss lattice Ξ to a smooth low-dimensional latent space $\mathbf{z} \in \mathbb{R}^d$ of d-dimensions, i.e., $\mathbf{z} = \mathcal{E}_\phi(\Xi)$. A *decoder* $\mathcal{D}_\zeta$ with trainable parameters ζ reconstructs the graph of the truss lattice from the latent vector, i.e., $\Xi = \mathcal{D}_\zeta(\mathbf{z})$. The NNs are trained such that the truss lattices input into the encoder are accurately reconstructed by the decoder, while modeling the latent space to closely follow a standard normal distribution. Given sufficient reconstruction accuracy over a representative dataset, the latent space serves as an informational bottleneck, providing a continuous and smooth, though abstract, vectorial representation of the design space. New designs can be generated by stochastically sampling the latent space via standard normal distribution and decoding into the graph representation, i.e., $\mathcal{D}_\zeta(\mathbf{z})$ with $\mathbf{z} \sim \mathcal{N}(\mathbf{0}, \mathbf{I})$. Simultaneously, a *property-predictor* neural network $\mathcal{P}_\psi: \mathbf{z} \rightarrow \mathbf{e}$ with trainable parameters ψ is trained to predict the effective piezoelectric matrix $\mathbf{e}$ from the latent representation. **Figure S2b** of the Supporting Information illustrates the prediction performance of the forward model with parity plots. The encoder, decoder, and property predictor are trained jointly, as detailed in Supporting Information Section 2, enabling the latent space to be learned in a manner that facilitates efficient structure-property map exploration.

The pre-trained VAE framework is then used to optimize within the latent space to discover truss lattices that achieve a tailored electromechanical response, as

shown in **Figure3.2b**. The optimization process starts with an initial guess $\mathbf{z}$ from the latent space, which is decoded into the corresponding unit cell architecture $\Xi = \mathcal{D}_\zeta(\mathbf{z})$. To ensure the validity of the architecture[23], it is re-encoded back into the latent space $\mathbf{z}' = \mathcal{E}_\phi(\Xi)$. The property predictor is used to estimate the effective piezoelectric matrix, i.e., $\mathbf{e} = \mathcal{P}_\psi(\mathbf{z}')$. The objective function is formulated in terms of $\mathbf{e}$. A gradient-based optimization algorithm is then employed to iteratively update the latent vector $\mathbf{z}$; the optimal $\mathbf{z}$ is then decoded into optimal truss lattice design. As an example, we aim to maximize piezoelectric response in transverse mode while minimizing the influence of longitudinal mode, i.e.,

$$\mathbf{z}^* \leftarrow \arg\max_{\mathbf{z}}(e_{31} - |e_{33}|), \qquad \text{with} \quad \mathbf{e} = \mathcal{P}_\psi(\mathbf{z}') \quad \text{and} \quad \mathbf{z}' = \mathcal{E}_\phi\left(\mathcal{D}_\zeta(\mathbf{z})\right).$$

Having such a piezoelectric response is advantageous in selectively activating transverse mode while minimizing the influence of longitudinal mode and thus providing a unidirectional sensor or actuator even under multi-directional loading.

The trace of the optimization in **Figure3.2d**, along with example lattices from checkpoints along the trace, shows the different designs and their properties traversed by the optimization algorithm in the process. **Figure3.2f** shows the training dataset properties in the e_{31} vs. target property ($e_{31} - |e_{33}|$) landscape. Similar to **Figure3.2e**, the optimized unit cell lies outside the bounds of the training dataset, showing an improvement of 18.42% compared to the best value of target property in the dataset. Details of the optimization and training protocols are presented in Supporting Information Section 2.

Figure3.2g and **Figure3.2h** show the optimized unit cells for the representative design problem from both the design spaces, their corresponding piezoelectric matrices, and piezoelectric surface plots. The spatial variation of the surface plots is such that if a vector is drawn from the center of the plot to any point on the surface, the length of the vector represents the magnitude of the longitudinal piezoelectric coefficient, $\tilde{e}(\boldsymbol{p})$ in the direction of that vector. Here, $\tilde{e}(\boldsymbol{p})$ is defined as the piezoelectric coefficient coupling axial stress in direction $\mathbf{p}$ to the electric field in direction $\mathbf{p}$. Along the direction $\mathbf{p} \in S^2$, where S^2 is a unit sphere in three-dimensional space, $\tilde{e}(\boldsymbol{p})$ evaluated as (Equation 8)

$$\tilde{e}(p) = \sum_{i,j,k=1}^{3} e_{ijk} p_i p_j p_k \tag{8}$$

While the first optimization example (**Figure3.2g**) shows a maximized F_H , the second example (**Figure3.2h**) shows a unidirectionality in electromechanical response, i.e., enhanced e_{31} and minimal e_{33}. In the former case, increased F_H and auxetic piezoelectric response provide higher energy harvesting and superior sensing capabilities due to the synergistic effect of transverse and longitudinal modes of operation, which are useful in underwater applications. In the latter case, isolating modes of operation in such a way is useful for transducers for a reduced effect of ambient acoustic and vibration noise, as well as in micro-robotics for specialized motion. Moreover, while e_{31}, and e_{32} are negative and e_{33} is positive for most of the conventional piezoelectric materials, in the truss metamaterials presented here, they are all positive, leading to auxetic piezoelectricity. This enables a synergistic interplay of these coefficients in multi-directional loading scenarios, unlike conventional piezoelectric materials, where the interplay is often destructive due to the opposing signs of these coefficients.

To complement the design methodologies and practical realization of truss metamaterials with tailored piezoelectricity, an efficient and accurate fabrication route is needed. Next, we present a custom technique for additively manufacturing these meta-materials.

3.2.3. IN-GEL DIRECT INK WRITING OF PIEZOELECTRIC METAMATERIALS

Additive manufacturing has recently driven innovation in metamaterials due to its versatility and material range. However, printing arbitrary shapes with piezoelectric materials, which are often brittle and polarization-dependent, presents challenges for 3D printing. The piezoelectric metamaterials designed here are 3D structures with varying feature sizes and inclinations. This proves challenging when relying solely on the rheology of the ink to create free standing structures. To address this, we employed a direct ink writing methodology for lead-free, 3% Li-substituted sodium potassium niobate $K_{0.485}Na_{0.485}Li_{0.03}NbO_3$ (KNLN), in combination with UV curable monomer poly-(ethylene glycol) diacrylate, PEGDA-700 (referred to as "piezo ink") printed embedded inside a supporting silicone matrix (referred to as "gel")

Filaments are printed in a single direction, ensuring directional homogeneity similar to simulated lattices and faster manufacturing without the need of a printed support structure. However, the extruder path must be optimized to avoid collisions and ensure end-connected struts. We used Fleury's algorithm- based approach

proposed by Weeks et al.[37], to optimize the path traversed by the extruder, avoiding collisions and minimizing travel motions.

Ink and gel design

The design of the piezoelectric and the support medium must satisfy certain key chemical and rheological requirements to enable the successful embedded printing of lattices. Similar to the requirements of the materials used for DIW in Ammu et al.[33], both the piezo ink and gel need to be shear-thinning yield stress materials, allowing material flow under applied pressure from the extruder. Additionally, the support gel must be thixotropic, enabling it to recover its viscoelastic behaviour after shear thinning. This ensures adequate support for the printed ink once the nozzle has moved past, allowing the gel to regain its elasticity and support the weight and shape of the printed ink.

To enable such embedded printing of lattices, we developed a chemically compatible and printable piezoelectric ceramic (KNLN)-polymer (PEGDA 700) composite ink and a silicone oil-based support matrix. KNLN-based inks were chosen for their high piezoelectric charge constants among lead-free piezoceramics and their biocompatibility. Stability and chemical compatibility between the ink and gel are crucial to prevent diffusion or reactions. A hydrophobic medium like silicone oil was chosen to prevent any diffusion of the hydrophilic PEGDA 700 monomer, which was observed in hydrophilic gels. The detailed manufacturing steps for the ink and gel are described in the Materials and Methods section.

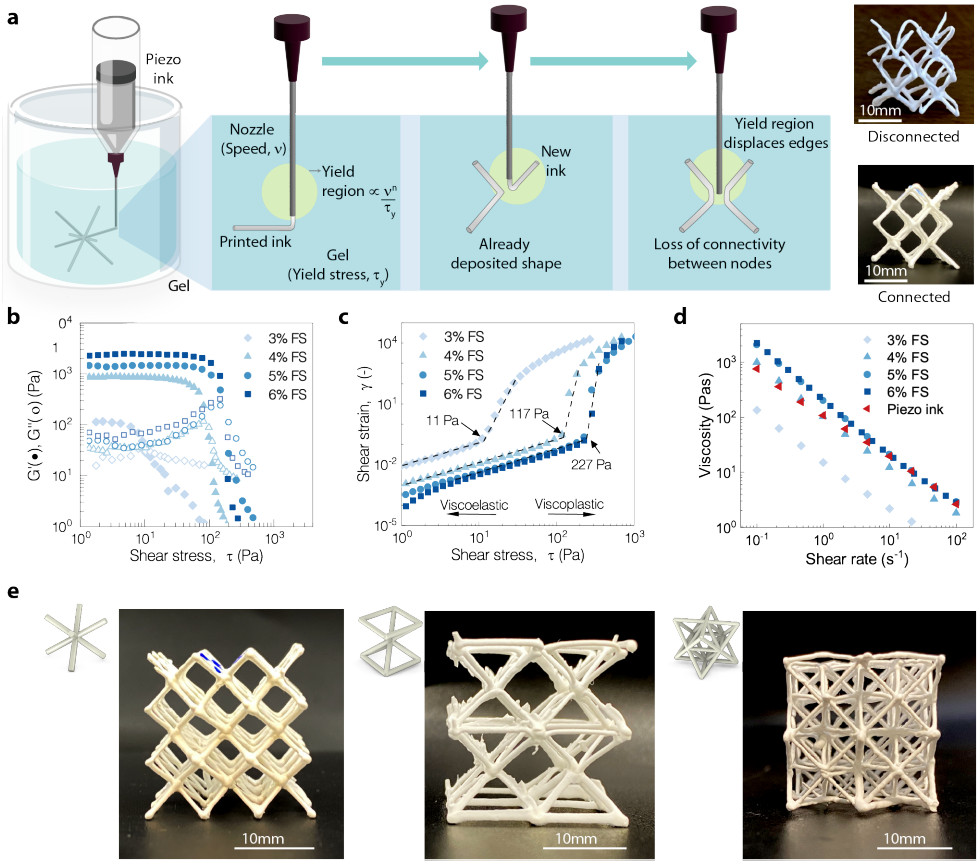

Figure 3.3: Embedded direct ink writing of piezoelectric metamaterials. (a) Schematic of in-gel direct ink writing process, and the optimization of ink rheology and printing parameters to ensure the connectivity at the nodes, (b) Oscillatory shear sweep on gels with varying fumed silica concentration showing the viscoelastic behaviour of the gels, (c) shear strain variation with applied shear stress for different volume fractions of fumed silica in the gel, and (d) varying viscosity of the gel with increasing shear stress for different volume fractions of fumed silica compared to the viscosity of the piezo ink showing viscosity matching in the shear rate around 0.1 to 0.7 s^{-1}.(e) various printed samples of lattices with the DIW techniques developed.

Ink design:

KNLN micro-particles with a particle size around 3.0 µm were chosen to maximize the volume fraction of the piezo inks and subsequent piezoelectric charge constants obtained from the composite. Using these particles, volume fractions in the range between 42 to 47% exhibit shear thinning behaviour along with the being able to be printed using our custom DIW setup. Below this volume fraction, the yield stress of the piezo ink is too low, causing either uncontrolled flow from the nozzle even when at rest or sedimentation of the particles, leading to nozzle clogging and

liquid phase migration. The low yield stress of the piezo ink leads to fragmentation and beading of the extruded ink due to the yield stress of the ink being lower than the surface tension of the gel, similar to what was observed by Pairam et al.[38]. On the other hand, if the piezo ink's elastic modulus and yield stress are too high, printed filaments may be dragged through the matrix by the nozzle, leading to poor connectivity at the nodes as shown schematically in **Figure 3.3a.**

Hence, a volume fraction closer to the lower end of the range, at 43 vol%, was chosen to maintain a high enough yield stress to allow stable extrusion while not being too viscous. This allows for designing a shear-thinning, thixotropic gel medium whose viscosity can be matched to that of the ink.

Gel design:

The gel was designed to have a high shear elastic modulus to sufficiently support the printed filament's weight and prevent sagging, which can occur due to the density mismatch between the ink and the support matrix, especially for ceramics like KNLN with a high density of 4.2 g·cc^{-1}. Fumed silica (FS) was chosen as the filler for the silicone gel preparation due to its ability to provide an elastic network structure with sharp shear thinning behaviour. Gels with less than 3% FS showed insufficient yield stress to be viscoelastic, leading to the investigation of gels with more than 3% FS as support media, as shown in **Figure 3.3b.**

The yield stress of the gel must be low enough to allow the nozzle to move through it freely and enable the gel to recover behind the nozzle. Printing inside a lower yield stress gel, such as 3% FS gel with a yield stress of 11 Pa, resulted in highly distorted and unconnected lattices, shown in **Figure 3.3a**. This issue arises because of the large size of stress field from the moving nozzle in a low yield stress gel which interferes with previously extruded ink. The size of the stress field is dependent on the Oldroyd number, defined as[39]

$$\mathrm{OD} = \frac{\tau_y \cdot d^n}{K \cdot U^n} \tag{9}$$

where τ_y is the yield stress, K is a constant determined by the matrix composition, n is a flow behaviour index, d is the nozzle diameter, and U is the print speed.

The objective was to maximize the Oldroyd number and subsequently minimize the stress field around the nozzle. Increasing the volume fraction of FS in the gel resulted in stiffer gels, as evidenced by the increase in yield stress of the gels from 11 to 221 Pa (**Figure 3.3c**), leading to improved shaping fidelity of the piezo ink. However, excessively high yield stress in the gel can cause static crevices that do

not collapse or self-heal, resulting in print distortions. The self-healing and collapse of crevices depend on printing depth and the rheological properties of the support matrix. Gels with more than 4% FS showed significant crevices and viscoplastic behaviour. Therefore, a gel with 4% FS, yielding a stress of 117 Pa, was chosen for its sufficient self-healing properties upon nozzle translation.

Printing speed design

For the chosen piezoelectric ink of 43 vol% and gel of 4 wt% FS, the print speed was used as a final control parameter to minimize the yield region. Viscosity vs. shear rates for both the gel and ink were measured at typical printing speeds, showing a match in the shear rate region between 0.1 $s^{-1}$and 0.7 s^{-1} as seen in **Figure 3.3d.**

The flow behaviour index *n* for these materials were then calculated by using Oswald-de Waele power law for shear-thinning fluids.

$$\tau = K\dot{\gamma}^{n} \tag{10}$$

Using *n* derived from the above equation, the range of printing speeds was determined based on the shear rate and nozzle diameter, found to be between 2 mm/min and 50 mm/min. Low printing speeds (2 mm/min) minimized the yield region but resulted in higher print times and potential sedimentation and clogging of the piezo ink. To mitigate this, printing was conducted at two speeds: the bulk of the lattice (95% of the strut length) was printed at a higher speed (50 mm/min) within the matched viscosity regime, while the remaining 5% near the edges was printed at a lower speed to ensure minimal disturbance of the printed lines. This strategy enabled relatively quick printing while ensuring well-connected and non-distorted lattices at the nodes. Multiple lattices with different unit cells were then printed, as depicted in **Figure 3.3e.**

3.2.4. TAILORED PIEZOELECTRICITY OF TRUSS METAMATERIALS

In this section, we demonstrate the directionality of the piezoelectric response in truss metamaterials by testing 3D-printed $3 \times 3 \times 3$ tesselations of BCC and octet unit cells. To show the architecture-driven electromechanical responses of these samples, we measured them in longitudinal and transverse modes. A standard Berlincourt d_{33}-meter was used to apply a harmonic force on the samples, and the generated voltage (ϕ) was recorded using a pico logger, as shown in **Figure 3.4a**. Multiple electromechanical phenomena, such as triboelectricity and flexoelectricity, can often co-exist in such systems and might influence accurate

piezoelectric characterization. To eliminate the possible influence of triboelectricity due to contact-separation and sliding of different surfaces, all the measurements were conducted while maintaining a static force larger than the applied dynamic force. Due to the macro scale size of the samples, the generated strain gradients are low, and thus the influence of flexoelectricity can be considered negligible[40]. With the robust measurement strategy, we turn to validate the directional response of BCC samples with FE simulations.

The amplitude of voltage in transverse and longitudinal modes is compared for the BCC sample in **Figure 3.4b**. While for the longitudinal mode, the force is applied to the electrodes, for measurements in the transverse mode, the samples are subjected to the harmonic excitation on the face normal to the direction 1. The normalized voltage response ($\phi/\phi_{\text{long}}^{\text{peak}}$) measured from experiments and that from FE simulations are plotted and found to be in good agreement. Here $\phi_{\text{long}}^{\text{peak}}$ is the peak voltage in the longitudinal mode. The ratio of the measured voltages in longitudinal and transverse modes is found to be ≈ 3.25 in both experiments and simulations. This shows the validity of the design approach as well as the developed printing technique in replicating ML-designed piezoelectric meta-materials. These measurements were performed at a forcing frequency of 110 Hz, which is the standard for characterizing bulk piezoelectric samples.

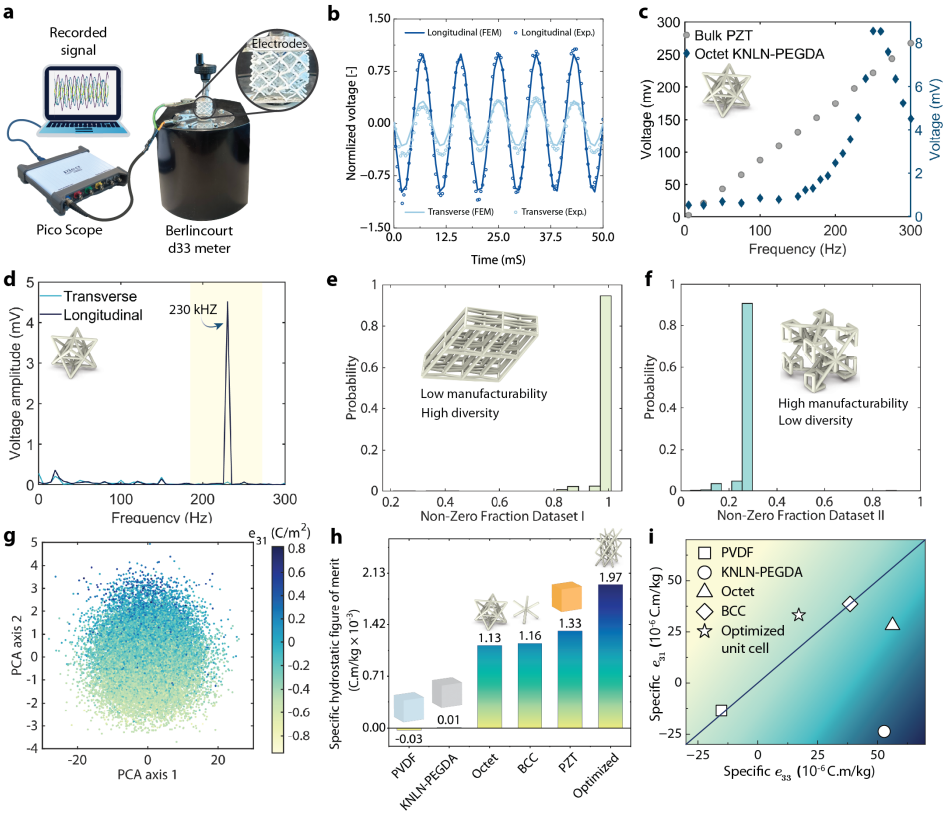

Figure 3.4. Evaluation of the tunable electromechanical response of piezoelectric truss metamaterials. (a) Schematic of the measurement setup used for recording the transient response of printed samples. The electrodes were fixed to samples at the top and bottom surfaces. The force was applied either in the longitudinal direction or in the transverse direction, depending on the mode of operation. (b) Comparison of the normalized voltage $\left(\phi/\phi_{\text{long}}^{\text{peak}}\right)$ observed from the experimental measurements of BCC lattice with the finite element simulations in transverse and longitudinal modes (c) The measured frequency vs voltage response of an octet metamaterial and a bulk PZT sample. The bulk PZT sample shows a linear increase in voltage, while for octet samples, a peak is observed at 250 Hz. (d) The frequency domain response of the octet samples under a harmonic force of 0.5 N at 230 Hz. The voltage peak at 230 Hz in longitudinal mode is found to be significantly higher than the transverse mode, as predicted by computational homogenization. (e-f) The comparison of the two design spaces utilized for optimization in terms of non-zero fraction, which is the ratio of number of non-zero components in the piezoelectric matrix to the total number of components. Design space I offers all 18 piezoelectric coefficients but lacks manufacturability due to extreme aspect ratios and skewed geometries. Design space II activates only five piezoelectric coefficients with a broader range and better manufacturability due to cubic symmetry. (g) PCA performed in the latent space of dataset II, where with the increasing values of principal component 2, the value of e_{31} increases. (h) PCA performed in the latent space of dataset II, where with the increasing values of principal component 2, the value of e_{31} increases. (i) *The e_{31} vs e_{32} plot for different piezoelectric materials shows that while most piezoelectric materials have e_{33} higher than e_{31} and lie below the 45slope line, the ML-optimzied unit cell is able to reverse this trend and has higher e_{31}.*

Due to lower resonant frequencies compared to bulk samples of similar dimensions, the piezoelectric response of piezoelectric truss metamaterials was

observed to be highly sensitive to the forcing frequency. The voltage responses of an octet sample and a standard bulk PZT sample were measured at different frequencies in the range of 5-300 Hz, as shown in **Figure 3.4c**. The PZT sample shows a linear increase in the voltage response with increasing forcing frequency, indicating that none of the resonance frequencies are close to the forcing frequencies. Thus, the equipment for measuring the piezoelectric coefficients of these samples is usually calibrated at these low frequencies for reliable estimates. For the octet sample, an exponential increase in voltage response with a peak at 250 Hz is observed, indicating mechanical resonance. This means that the harmonic force or impact measurements, commonly used for bulk piezoelectric samples, are not well suited for characterizing the piezoelectric coefficients of the truss metamaterials. Therefore, to avoid the influence of mechanical resonance on characterization, we restrict ourselves to evaluating only the transient response of truss metamaterials in this low-frequency regime.

We further demonstrate the directionality of piezoelectric response in metamaterials by measuring the voltage response of octet samples in transverse and longitudinal modes. The frequency domain voltage response of the octet sample under a dynamic load of 230 Hz is compared in transverse and longitudinal modes in **Figure 3.4d**. The voltage peaks at 230 Hz in longitudinal mode is found to be approximately 65 times the peak in transverse mode due to the high d_{33}/d_{31} ratio of the octet unit cells, in contrast to the base composite material where this ratio is approximately 2. This shows the effectiveness of the truss metamaterials in providing tailored piezoelectric response. An important factor to be considered for the physical realization of this concept is the compromise between the tunable piezoelectric properties and manufacturability constraints.

The two design spaces presented in this study provide different combinations of manufacturability and range of properties. Design space I can offer more diverse piezoelectric responses compared to design space II. **Figure 3.4e** shows the distribution of the fraction of non-zero coefficients of the piezoelectric matrix in design space I, which is defined as the ratio of number of non-zero piezoelectric coefficients in the piezoelectric matrix to the total number of coefficients. Most of the designs are found to have all 18 coefficients non-zero, indicated by a close to one probability distribution of the non-zero fraction of one. For design space II, most of the unit cells in the dataset are found to have a non-zero components fraction of 5/18, since only five of the 18 coefficients are non-zero, as shown in **Figure 3.4f**. While limited to only five coefficients, all the unit cells in design space II have a cubic symmetry, leading to improved manufacturability. As shown in Supporting

Information **Figure S5a**, the dataset from design space I shows a narrower range of coefficients e_{31} and e_{32}, restricted to only positive values. The distribution of e_{31} and e_{32} for dataset II in Supporting Information **Figure S5b** shows these coefficients ranging from negative to positive values. Thus, the trade-off between manufacturability and range of properties should be considered depending upon the manufacturing capabilities available and the intended application. These distinct features of the two design spaces stem from the different parameterizations used to construct them.

We explored the two design spaces for the influence of specific design parameters on the unit cell designs and their piezoelectric properties. **Figure 3.4g** shows the principal component analyses (PCA) conducted in the latent space of the VAE framework for design space II. Since the latent space was trained in conjunction with the property predictor NN, the latent space parameters are intertwined with the piezoelectric properties. A strong correlation between the principal component 2 and the piezoelectric coefficient e_{31} was observed. The principal component 1 has a weaker influence on e_{31}, while the geometry still evolves along principal axis 1, as shown in Supporting Information **Figure 7a-b,** along with the evolution of the unit cell designs. Supporting Information **Figure S7c** shows PCA for the parameter space of design space I. We found that the principal components of design space I do not have a direct correlation with the piezoelectric coefficient e_{31}. This is due to the discrete nature of the design space I and small changes in design parameters resulting in sudden jumps in piezoelectric properties, as was also observed during the optimization in **Figure3.2c**. We take one example of optimization performed in each design space and compare their piezoelectricity with bulk materials.

We compared the piezoelectric performance of the metamaterials for application-relevant metrics. The optimized lattice obtained by maximizing the hydrostatic figure of merit in design space I (Equation 6) outperforms the commonly used bulk materials, as well as the KNLN-PEGDA composite. The optimized truss metamaterial offers a lightweight alternative for energy harvesting, actuation and sensing applications under hydrostatic loads and uniform actuation, such as in underwater sensing applications. In applications where unidirectional sensing or actuation is required, the isolation of modes of piezoelectricity becomes crucial. We explored one such possibility, where higher transverse piezoelectricity is desired compared to longitudinal piezoelectricity, by solving the optimization problem in Equation 7. **Figure 3.4i** shows the comparison of the optimized lattice with the bulk materials in the normalized e_{33} vs e_{31} landscape. Most of the common bulk materials, as well as the base material, lie below the unit slope line since the

magnitude of e_{33} is higher than e_{31} for these materials, PVDF being an exception with a slightly higher value of e_{31}. The optimized lattice shows the highest value of normalized $e_{31} - |e_{33}|$ and lies beyond the unit slope line. This enables the pure transverse mode operation of piezoelectric materials even under mixed loading conditions, with potential applications in specialized motion in micro-robots, medical equipment, and unidirectional electromechanical transducers.

3.3. CONCLUSIONS

Considering that most of the common bulk piezoelectric materials are restricted to the same symmetry class, our ML-based approach to designing new metamaterials offers clear advantages. Specifically, we achieved a hydrostatic figure of merit for metamaterials higher than their bulk counterparts, and a significantly higher e_{31} values compared to e_{33}. The optimized properties of these metamaterials extend beyond the training design space, demonstrating the extrapolatory capabilities of our proposed ML framework.

Through optimization, we also discovered that designs constrained within cubic symmetry are limited to the standard five piezoelectric coefficients. Accessing additional coefficients requires skewed geometries or aspect ratios in the unit cells. Consequently, our strategy of exploring two design spaces maximizes both absolute performance and anisotropy or manufacturability. Our results show that truss metamaterials offer exceptional flexibility in tuning the piezoelectric response, activating all 18 coefficients, and enabling rare or unique combinations of coefficients not found in conventional materials. Principal Component Analysis of the latent space of design space II and design space I revealed differing behaviours. In design space II, the second principal component directly influenced the magnitude of e_{31}, while design space I exhibited no discernible trend.

In characterizing the response of 3D-printed octet metamaterials in longitudinal mode, we observed an exponential increase in the piezoelectric response at low frequencies, peaking in local resonance at 250 Hz. This finding suggests that standard characterization frequencies and methods for bulk piezoelectric materials may not be suitable for lattice structures. We propose that future studies further explore the frequency dependence of piezoelectric materials. Despite these considerations, lightweight lattice structures optimized using our ML framework outperform bulk materials in key metrics, such as specific hydrostatic performance or achieving dominant transverse piezoelectricity over longitudinal modes. Our developed optimization framework and 3D-printing technique provide a novel way to design piezoelectric materials, overcoming limitations in material and symmetry classes. These advancements enable the creation of multi-modal electromechanical devices with tailored behaviours, potentially useful in applications such as micro robotics and health monitoring devices. Our electromechanical testing also reveals the importance of considering structural

dynamics in individual structures and designing specific mechanical and electrical boundary conditions for lattice-based piezoelectric materials.

This work advances the field of piezoelectricity by demonstrating the potential to optimize piezoelectric performance through structural design, transcending the constraints of conventional bulk materials' symmetries. Our proposed 3D-printing technique, coupled with a graph-based path planning framework, offers enhanced shaping freedom and precision, paving the way for advanced piezoelectric composite materials. These developments open new possibilities for electromechanical systems with engineered physical and responsive behaviours.

3.4. MATERIALS AND METHODS

Numerical homogenization

The details of the FEA formulation for homogenization are provided in Supporting Information, Section 1. For the base material used in simulations, isotropic elastic properties are assumed with Young's modulus $E^{\text{base}} = 60.606$ GPa and Poisson's ratio $\nu = 0.3$. For the piezoelectric properties, $e_{31}^{\text{base}} = e_{32}^{\text{base}} = -6.62281$ C/m^2, $e_{33}^{\text{base}} = 23.2403$ C/m^2, and $e_{15}^{\text{base}} = e_{24}^{\text{base}} = 17.0345$ C/m^2 are considered, while the relative dielectric permittivity is $\kappa_{11} = \kappa_{22} = \kappa_{33} = 1433.6$.

ML protocols: Details of the ML training and optimization protocols are provided in Supporting Information, Section 2.

Ceramic synthesis

We synthesized the $K_{0.485}Na_{0.485}Li_{0.03}NbO_3$ (KNLN) ceramic powder prepared through a conventional solid-state reaction with a two-step calcination procedure that has been previously studied[41]. Stoichiometric proportions of >99 % Na_2CO_3, K_2CO_3, Li_2CO_3, and Nb_2O_5 (Sigma Aldrich) were milled with 5 mm yttria-stabilised ZrO_2 balls in hexane for 3 hours at 200 rpm. The milled powders were air dried on a hot plate at 100°C for 1 hour, and the dried green powder was calcined at 1050 °C for 3 hours with a heating rate of 5 °C·min^{-1}. The calcined ceramic was milled with 5 mm balls in IPA for 3 hours at 200 rpm, followed by air dying and a second, longer calcination at 925 °C for 20 hours with a heating rate of 1 °C·min^{-1}. The calcined powder was ball milled in IPA for 15 minutes, air dried, sieved through a 90µm sieve and then stored under vacuum. The particle morphology was analysed using a Scanning Electron Microscope, SEM (JEOL, JSM-7500F, Nieuw Vennep, the Netherlands). The particle size distribution of the milled powders was measured using Malvern Mastersizer 3000 on 0.1% weight/volume aqueous solution of the powders using sodium dodecyl sulphate solution as surfactant. The mean value of the distribution then represented the particle size of each type of powder.

Ink preparation

Piezoelectric ink: The synthesized ceramic powder was mixed with the UV-sensitive monomer poly(ethylene glycol) diacrylate with Mn 700 (Sigma Aldrich) in varying

volume fractions. This mixture was combined using a planetary mixer (SpeedMixer DAC 150.1 FVZ) at 3500 rpm for 2 minutes, with 30-second intervals and a 15-second break to prevent excessive heating. Two photoinitiators, Irgacure 819 and 184, were added to maximize curing depth due to the high ceramic filler content, creating a UV-curable piezoelectric ink. The photoinitiators were added to the KNLN-PEGDA mixture in ratios of 1% and 2% by weight relative to the monomer and mixed at 1000 rpm for 5 minutes to ensure homogeneous distribution.

Support gel: The gel is created by dispersing 4 wt.% of fumed silica (Sigma Aldrich S5130) in silicone oil. This mixture is processed in a planetary mixer (SpeedMixer DAC 150.1 FVZ) at 3500 rpm for 5 minutes to ensure thorough dispersion and uniformity.

Rheological characterisation

The rheological properties of the inks were characterised using a rotational rheometer (Haake Mars III, Thermoscientific) with a 20 mm diameter serrated plate geometry using a gap height of 1 mm. Serrated plates prevent artefacts in measurements arising from wall slip, which has been studied to occur when highly loaded dispersions are subject to high localised deformation. Shear storage and loss moduli were determined as a function of shear strain via dynamic amplitude sweeps at a fixed frequency of 1 Hz with a stress sweep. The yield stress was measured via steady-state flow experiments with a sweep of shear stress and measuring. We used the point of change in slope of the log-log plot of shear stress vs strain to calculate the yield stress of the ink. The viscosity vs shear rates was measured between shear rates from 0.1 to 100 s^{-1}.

Printing and curing

A commercial desktop printer (Ultimaker 2+) was modified by replacing the original print head with a custom-made ink extrusion system consisting of a 25ml syringe holder and a mechanically driven syringe pump. The inks loaded into syringes were attached with stainless steel nozzles of 1.5-inch length with an inner diameter of 0.5 mm and were used for printing. The printed lines or parts were cured using an Omnicure S1500 (Lumen Dynamics) UV-lamp at 100% intensity at 20 cm for 30 seconds for the final part.

Poling

The printed samples are first cleaned in a Hexane solution to wash away the silicone oil and facilitate better electrode adhesion. A corona poling setup is used to pole the sample with 5 kV as the bottom plate potential and 50 kV applied to the pin electrodes. The base plate is heated to 120 °C to allow for the reorientation of the dipoles in the samples. Samples are poled for 6 hours, after which they are cooled to room temperature with the electric field applied and used for measurements.

Piezoelectric characterisation

Aluminium metal electrodes were attached to the faces which were in the same direction as that of the poling direction (3) using a silver epoxy adhesive. The piezoelectric voltage was measured using a Berlincourt (PM 300, Piezo test, London, UK) piezometer with a static force of 2N and a dynamic peak-to-peak sinusoidal excitation ranging between 0.05 N and 0.5 N at 110 Hz. The output voltage was measuring using a Picoscope (5442D series)

Code availability and data availability

The link https://surfdrive.surf.nl/files/index.php/s/9psV3hcS7lGmNo8 contains the codes and data generated during the current study.

3.5. REFERENCES

[1] D. Kim, S. A. Han, J. H. Kim, J.-H. Lee, S.-W. Kim, S.-W. Lee, *Advanced Materials* **2020**, *32*, 1906989.

[2] B. Tandon, J. J. Blaker, S. H. Cartmell, *Acta biomaterialia* **2018**, *73*, 1.

[3] Q. Xu, X. Gao, S. Zhao, Y.-N. Liu, D. Zhang, K. Zhou, H. Khanbareh, W. Chen, Y. Zhang, C. Bowen, *Advanced Materials* **2021**, *33*, 2008452.

[4] H. Boukabache, C. Escriba, J.-Y. Fourniols, *Sensors* **2014**, *14*, 20543.

[5] H. Elahi, M. Eugeni, P. Gaudenzi, F. Qayyum, R. F. Swati, H. M. Khan, *Microsystem Technologies* **2018**, *24*, 3791.

[6] N. Jackson, L. Keeney, A. Mathewson, *Smart Materials and Structures* **2013**, *22*, 115033.

[7] S.-G. Kim, S. Priya, I. Kanno, *MRS bulletin* **2012**, *37*, 1039.

[8] K.-B. Kim, J. Y. Cho, H. Jabbar, J. H. Ahn, S. Do Hong, S. B. Woo, T. H. Sung, *Energy Conversion and Management* **2018**, *171*, 31.

[9] H. Yang, L. Wang, B. Zhou, Y. Wei, Q. Zhao, *International Journal of Pavement Research and Technology* **2018**, *11*, 168.

[10] W. Qian, W. Yang, Y. Zhang, C. R. Bowen, Y. Yang, *Nano-Micro Letters* **2020**, *12*, 1.

[11] X. Hu, X. Yan, L. Gong, F. Wang, Y. Xu, L. Feng, D. Zhang, Y. Jiang, *ACS applied materials & interfaces* **2019**, *11*, 7379.

[12] K. Shi, B. Chai, H. Zou, P. Shen, B. Sun, P. Jiang, Z. Shi, X. Huang, *Nano Energy* **2021**, *80*, 105515.

[13] M. Abbasipour, R. Khajavi, A. A. Yousefi, M. E. Yazdanshenas, F. Razaghian, A. Akbarzadeh, *Polymers for Advanced Technologies* **2019**, *30*, 279.

[14] J. A. Krishnaswamy, F. C. Buroni, F. Garcia-Sanchez, R. Melnik, L. Rodriguez-Tembleque, A. Saez, *Smart Materials and Structures* **2019**, *28*, 075032.

[15] Z. Chen, Z. Li, J. Qiu, T. Zhao, J. Ding, X. Jia, W. Zhu, J. Xu, *Journal of the European Ceramic Society* **2018**, *38*, 1349.

[16] C. Wang, J. Zhao, Q. Li, Y. Li, *Applied energy* **2018**, *229*, 18.

[17] B. V. De Almeida, D. C. Cunha, R. Pavanello, *Smart Materials and Structures* **2019**, *28*, 085030.

[18] G. H. Yoon, H. Choi, S. Hur, *Computer Methods in Applied Mechanics and Engineering* **2018**, *332*, 600.

[19] I. Katsouras, K. Asadi, M. Li, T. B. Van Driel, K. S. Kjaer, D. Zhao, T. Lenz, Y. Gu, P. W. Blom, D. Damjanovic, others, *Nature materials* **2016**, *15*, 78.

[20] Q. Xu, X. Zhao, X. Li, H. Deng, H. Yan, L. Yang, W. Di, H. Luo, N. Neumann, *Infrared Physics & Technology* **2016**, *76*, 111.

[21] N. Chong, H. Chan, C. Choy, *Sensors and Actuators A: Physical* **2002**, *96*, 231.

[22] J.-H. Bastek, S. Kumar, B. Telgen, R. N. Glaesener, D. M. Kochmann, *Proceedings of the National Academy of Sciences* **2022**, *119*, e2111505119.

[23] L. Zheng, K. Karapiperis, S. Kumar, D. M. Kochmann, *Nature Communications* **2023**, *14*, 7563.
[24] A. J. D. Shaikeea, H. Cui, M. O'Masta, X. R. Zheng, V. S. Deshpande, *Nature Materials* **2022**, *21*, 297.
[25] K. Bertoldi, V. Vitelli, J. Christensen, M. Van Hecke, *Nature Reviews Materials* **2017**, *2*, 1.
[26] X. Zheng, H. Lee, T. H. Weisgraber, M. Shusteff, J. DeOtte, E. B. Duoss, J. D. Kuntz, M. M. Biener, Q. Ge, J. A. Jackson, others, *Science* **2014**, *344*, 1373.
[27] A. Rafsanjani, A. Akbarzadeh, D. Pasini, *Advanced Materials* **2015**, *27*, 5931.
[28] D. Rocklin, S. Zhou, K. Sun, X. Mao, *Nature communications* **2017**, *8*, 1.
[29] K. K. Dudek, J. A. I. Martínez, G. Ulliac, M. Kadic, *Advanced Materials* **2022**, *34*, 2110115.
[30] H. Cui, R. Hensleigh, D. Yao, D. Maurya, P. Kumar, M. G. Kang, S. Priya, X. R. Zheng, *Nature materials* **2019**, *18*, 234.
[31] H. Cui, D. Yao, R. Hensleigh, H. Lu, A. Calderon, Z. Xu, S. Davaria, Z. Wang, P. Mercier, P. Tarazaga, others, *Science* **2022**, *376*, 1287.
[32] J. Shi, K. Ju, H. Chen, A. Mirabolghasemi, S. Akhtar, A. Sasmito, A. Akbarzadeh, *Nano Energy* **2024**, *123*, 109385.
[33] S. K. Ammu, X. Chen, D. G. Ulcay, S. Sharma, F. Alijani, P. G. Steeneken, P. Groen, K. Masania, *Advanced Materials Technologies* **2024**, 2400858.
[34] R. Tao, F. Granier, D. Therriault, *Additive Manufacturing* **2022**, *60*, 103243.
[35] S. Sharma, R. Kumar, M. Talha, R. Vaish, International Journal of Mechanics and Materials in Design **2021**, 17, 99.
[36] F. W. Zok, R. M. Latture, M. R. Begley, *Journal of the Mechanics and Physics of Solids* **2016**, *96*, 184.
[37] R. D. Weeks, R. L. Truby, S. G. Uzel, J. A. Lewis, *Advanced Materials* **2023**, *35*, 2206958.
[38] E. Pairam, J. Vallamkondu, V. Koning, B. C. van Zuiden, P. W. Ellis, M. A. Bates, V. Vitelli, A. Fernandez-Nieves, *Proceedings of the National Academy of Sciences* **2013**, *110*, 9295.
[39] A. K. Grosskopf, R. L. Truby, H. Kim, A. Perazzo, J. A. Lewis, H. A. Stone, *ACS applied materials & interfaces* **2018**, *10*, 23353.
[40] S. Sharma, C. Anitescu, T. Rabczuk, *Computers & Structures* **2025**, *308*, 107641.
[41] N. K. James, D. B. Deutz, R. K. Bose, S. van der Zwaag, P. Groen, *Journal of the American Ceramic Society* **2016**, *99*, 3957.

4

GROWTH, DISTRIBUTION, AND PHOTOSYNTHESIS OF *CHLAMYDOMONAS REINHARDTII* IN 3D HYDROGELS

Engineered living materials (ELMs) are a novel class of functional materials that typically feature spatial confinement of living components within an inert polymer matrix to recreate biological functions. Understanding the growth and spatial configuration of cellular populations within a matrix is crucial to predicting and improving their responsive potential and functionality. Here, we investigate the growth, spatial distribution, and photosynthetic productivity of eukaryotic microalga Chlamydomonas reinhardtii in three-dimensionally shaped hydrogels in dependence of geometry and size. The embedded C. reinhardtii cells photosynthesize and form confined cell clusters, which grow faster when located close to the ELM periphery due to favourable gas exchange and light conditions. Taking advantage of location-specific growth patterns, we successfully design and print photosynthetic ELMs with increased CO2 capturing rate, featuring high surface to volume ratio. This strategy to control cell growth for higher productivity of ELMs resembles the already established adaptations found in multicellular plant leaves.

This chapter has been published as J.-J. Oh, S. Ammu, V. D. Vriend, R. Kieffer, F. H. Kleiner, S. Balasubramanian, E. Karana, K. Masania, M.-E. Aubin-Tam, “Growth, Distribution, and Photosynthesis of Chlamydomonas Reinhardtii in 3D Hydrogels”. Adv. Mater. 2024, 36, 2305505.

4.1. INTRODUCTION

Engineered living materials (ELMs) integrate living organisms as active components within natural or synthetic matrices to create life-like functions[1] such as metabolite production, stimuli-responsiveness, programmable development and growth, and self-repair[2-4]. These bio-hybrid materials usually require that the living organisms grow and function properly while being spatially confined within an associative matrix. The matrix needs to provide a favourable environment for growth, while allowing sufficient mass transfer of gas and nutrients. For more predictable, highly functional ELMs with increased longevity, it is crucial to understand the cell growth within matrices, and to identify the environmental factors important for cells' productivity and function. Recent studies of bacteria and yeasts confined in hydrogels showed that cells formed non-motile spherical clusters primarily localized in the periphery of hydrogels[5, 6]. These observations suggest that simply increasing the total volume of ELMs would not necessarily lead to higher functionality/productivity.

Photosynthetic microorganisms can be integrated into polymeric matrices to form ELMs with plant-like qualities[7-17], allowing them to photosynthesize and thus to provide a localized O_2 source[12,15] and/or CO_2 sink. The high tolerance of many microalgae to abiotic stress factors such as temperature, pH or osmotic stress broaden the spectrum of potential applications for photosynthetic ELMs. Based on these properties, microalgal ELMs show great promise for generating bio-electricity[14], oxygenating mammalian tissues in biomedical applications[15], improving air and water quality[7,9,16], and granting photoresponsive/photoadaptive functions to materials. The current research on fabrication of microalgal ELMs has so far focused on formulation of hydrogel[10], viability of embedded cells[8, 10, 15], and O_2 production capacity in dependence of time[7, 9]. However, fundamental understanding on how microalgae cells spatially localize and grow within matrices is still in its infancy, which has been the major obstacle to predict and intensify the functionality of these photosynthetic ELMs.

Here, we investigate the growth, spatial distribution, and photosynthetic productivity of eukaryotic microalga *Chlamydomonas reinhardtii* within a mechanically stable 3D printed hydrogel-based ELM over time **(Figure 4.1)**. By regulating geometry and tuning hydrogel composition, we identify important factors that impact the spatial localization of embedded cells. Based on these factors, and inspired by plant leaves, we successfully adjust our gel architecture to accommodate the needs of the cells, allowing higher photosynthetic activity.

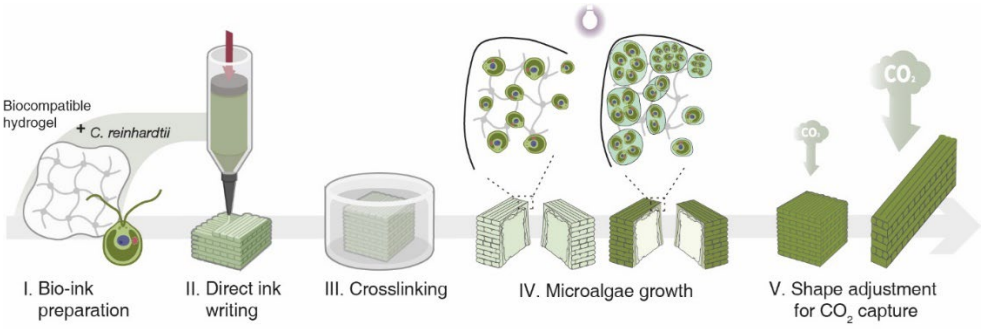

Figure 4.1. Schematic diagram exhibiting the individual steps from (I) biocompatible ink formulation containing eukaryotic microalga *Chlamydomonas reinhardtii*, (II) three-dimensional shaping of the ELM based on a direct ink writing method, (III) crosslinking for mechanical stability, (IV) characterization of cell growth and spatial distribution of microalgae in different light regimes, (V) spatial organization of ELMs for higher photosynthetic activity.

4.2. RESULTS AND DISCUSSION

4.2.1. SHAPING *C. REINHARDTII*-LADEN BIOPRINTS

Shaping of ELMs with 3D printing allows spatial arrangement of a bio-ink into favourable cell growth conditions, thereby increasing the ELM functionality in a manner that is difficult to achieve with moulding approaches[12,15]. *C. reinhardtii* cells mixed with κ-carrageenan, sodium alginate, agar, and cellulose-based thickener were 3D printed by direct extrusion and deposition in a layer-by-layer fashion. A similar ink composition enabled the printing of mycelium-based ELM structures that are not limited in height[18], as opposed to most alginate-based printing approaches[17, 19]. Ideally, the 3D printed matrix should exhibit enough resistance to capillarity- and gravity-driven physical deformation for self-support and should be sufficiently strong and stiff to maintain structural integrity while being manipulated after the printing process. Such manipulation was not possible with the original ink composition[18], which harnessed hyphal growth to introduce structural integrity to the hydrogel. We therefore first proceeded by developing an approach to mechanically strengthen the matrix through crosslinking.

Sodium alginate was included in the ink, aiming to achieve higher mechanical robustness, due to the ability of alginate to form a hydrogel when crosslinked with Ca^{2+} ions. We investigated whether Ca^{2+} diffusion into the alginate-containing prints (without algae) would lead to higher mechanical stiffness of ELMs (**Figure 4.2a**). The optimal crosslinking conditions were determined with a comparison of storage moduli (*G'*) of prints immersed into solutions with varying Ca^{2+} molarity (0.1 – 0.5 M) for different durations (5 and 60 mins). By immersing the prints for 5 mins at respective concentrations, the storage moduli were found to reach their maximal value at a concentration of 0.2 M Ca^{2+} (**Figure 4.2b**). Immersing prints for 5 and 60 mins into 0.2 M Ca^{2+} solution provided similar mechanical properties (**Figure 4.2c**). Thus, soaking prints into 0.2 M Ca^{2+} solution for 5 mins was set as the optimal crosslinking procedure, where the yield point significantly increased from 426 Pa to 6.1 kPa after crosslinking (**Figure 4.2d**). Although aging prints for two weeks without controlled Ca^{2+} crosslinking also results in an increased yield point, the yield point is lower (4.6 kPa) (**Figure 4.2e**). These results show the value of Ca^{2+} alginate crosslinking to achieve higher mechanical robustness within a short time **.**

A reproducible 'bio-ink' with a cell density of 6.67×10^5 cells/g within the alginate-containing ink was prepared to fabricate microalgal ELMs **(Figure S4.1)**. Embedded cells potentially affect the rheology of the ink and mechanical properties of prints[20-

[23]. Further, the embedded cells represent physical obstacles which may limit interaction between matrix components or interfere with crosslinking of components and vary the mechanical stability[24, 25]. To quantify the possible effects of cell embedding, the rheological behaviour of the bio-ink and the mechanical stability of crosslinked bioprints were investigated.

The rheological behaviour of the bio-ink was studied with focus on flow behaviour and recovery of viscoelasticity. The incorporation of *C. reinhardtii* into the ink did not considerably affect the flow behaviour. As shown in **Figure 4.2d**, ink with and without living cells both displayed shear-thinning behaviours and had both similar yield stress values (426 Pa without cells, 413 Pa with cells). The elastic recovery of the ink with and without algae after yield was measured using an oscillation-rotation and oscillation test. The rotational shear was applied to simulate the high extrusion force, whereas the oscillatory shear measurement was applied to quantify the storage modulus of the bio-ink before and after yield. After incorporating *C. reinhardtii* cells, the properties of viscoelasticity recovery were not changed (**Figure 4.2f**). Both prints showed instantaneous elastic recovery within seconds, meaning that filaments of both inks can prevent flow-induced distortion after the deposition. These results confirm that the bio-ink has similar rheological properties as the cell-free ink. At 0.03 wt.%, the low weight fraction of cells in bio-ink did not influence the yield stress (**Figure S4.1**).

Likewise, the mechanical stability was unaffected by the incorporation of living cells. Soaking the cell-containing bioprints in Ca^{2+} solution significantly increased the yield point from 413 Pa to 5.7 kPa (**Figure 4.2d**), which is similar to cell-free prints. In addition, aging of crosslinked bioprints for two weeks further increases the yield point to 12 kPa (**Figure 4.2g**). These observations inform us that the shaping and crosslinking approach is promising, and the microalgal ELMs demonstrate more mechanical robustness over time.

Complex geometries such as grid-like or hollow structures can enable increased functionality for ELMs[18, 26]. These features require shape fidelity of filaments over a supporting structure. To quantify the shape fidelity, the bridging capability of the *C. reinhardtii*-laden printed hydrogel was investigated[27]. A support structure with increasingly long spanning elements was printed, as shown in **Figure 4.2h**. The extent of sagging as a function of the length of the filament was determined by measuring z-deflection using optical profilometry[27]. The deflection of the printed filaments scales with the spanning length, as shown in **Figure 4.2i**. The filament

could be bridged up to 3.5 mm with less than 0.2 mm of tolerable sagging, suggesting complex geometries within a limited bridging length could be formed.

The achieved rheological properties and shape fidelity of the bio-ink enable the fabrication of various macroscopic 3D geometries of ELMs with complex features (**Figure 4.2j**). We printed open architectures which provide a 3D environment for the growth of algae throughout the hydrogel into functional materials benefiting from high surface area. The shaping capabilities of 3D printing can be exploited to manufacture geometries that match the functional requirements of specific scenarios. The yield stress of the ink is an important parameter in the shaping, and crosslinking the ELM after printing increased the yield stress by one order of magnitude. This allows difficult shapes such as the overhanging arms of the cactus structure.

Flat prints with small protrusions of less than 5 mm (for seaweed shape) were prepared without flow-induced distortion after extrusion. The high yield points of the crosslinked bio-ink enable standing shapes with hanging elements, as exemplified by the arms of the cactus and the floating leaves of succulent plants. Using a computational approach, the volume and surface area of the ELM structures were compared (**Figure 4.2k**). We note that the highly branched nature of the seaweed geometry demonstrates the highest surface to volume ratio, at almost 5.5 times higher than the cactus structure.

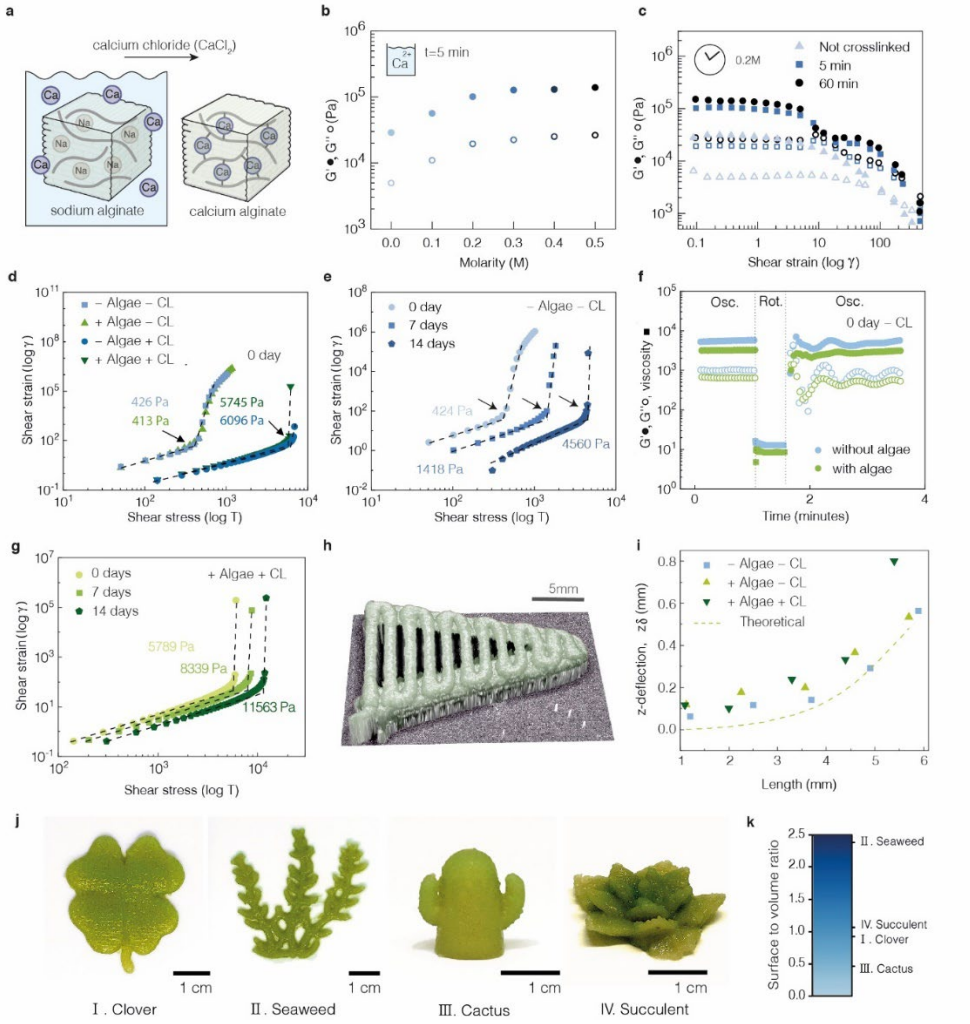

Figure 4.2. Rheological behaviour of *C. reinhardtii*-laden bioprints. (a) Schematics displaying the crosslinking of prints using calcium chloride for transition of sodium alginate to calcium alginate. (b) Effects of Ca^{2+} molarity on the storage (G') and loss moduli (G'') of the print without microalgae. (c) Influence of crosslinking time on the storage (G') and loss moduli (G'') of the print without microalgae as a function of oscillatory shear strain. (d) Flow behaviour of 0-day old prints depending on crosslinking and microalgae integration. (e) Flow behaviour changes of prints without microalgae nor crosslinking over 2 weeks. Black arrows with numerical values in (d) and (e) indicate the yield points above which physical deformation occurs. (f) Elastic recovery of prints (not crosslinked) depending on microalgae integration. (g) Yield stress of crosslinked cell-containing bioprints, 0, 7 and 14 days after printing and crosslinking. (h) Bridging ability of the C. reinhardtii-laden prints (not crosslinked). (i) Measured and calculated deflection (δ_{zmax}) of the bridging filaments as a function of their spanning length. (j) 3D microalgal ELMs in the shape of a cactus, clover, aloe, and seaweed, 14 days after incubation under autotrophic conditions. (k) Theoretical surface to volume ratio of microalgal ELMs. CL indicates Ca^{2+} crosslinking of hydrogel.

4.2.2. GROWTH OF EMBEDDED *C. REINHARDTII* INSIDE HYDROGELS

We chose a 1 cm^3 cube-shaped ELM as a model to characterise the growth of *C. reinhardtii* cells within hydrogels. The cubes were incubated under autotrophic conditions (i.e. without another carbon source than CO_2 from the atmosphere) and cell growth was monitored over time by visual inspection (**Figure 4.3a**). At day 0, bioprints displayed a white colour, mainly representing the raw Ca^{2+} crosslinked hydrogels. After 3 days of incubation, the surface of the bioprints started to display a faint green, indicating the growth of microalgae. Continuous growth over the following 14 days led to a darker green. After 14 days, no further change in colour was observed for the next 35 days (**Figure S4.2**). Examination of cross-sectional cuts of bioprints revealed that the growth of microalgae mostly occurred in a thin layer of 1-2 mm below the outer periphery of the cube (**Figure 4.3a**), in which most cells stay alive beyond 14 days (**Figure S4.3**). Confocal scanning microscopic imaging showed that *C. reinhardtii* cells were non-motile and form individual colonies within the hydrogel, and that each colony originates from a single cell rather than being the result of aggregation of cells (**Figure S4**). Light microscopic images revealed the presence of a thin membrane-like structure at the periphery of individual colonies, suggesting that cells entered the palmelloid stage[28] **(Figure 4.3b,c**; **Figure S4.5)**. In liquid culture, the palmelloid stage is formed in response to various stresses[29, 30]. *C. reinhardtii* were also found to be in a state consistent with palmelloids (no flagella, cluster formation) when embedded in other hydrogel systems[7, 17, 31, 32]. Cells within our hydrogel are likely to form clusters as a passive result of cell division within a confined environment, although we cannot exclude palmelloids being induced (partly) by other stress factors[28-30]. Printed 1 cm^3 cubes immersed in Tris minimal media also showed similar growth to those observed in air-exposed cubes, and individual colonies formed within the hydrogel (**Figure S4.6**). Interestingly, submerging the 14-day old ELM placed in air in Tris minimum medium induced the algae cells to flagellate, regain their motility, and populate the surrounding medium**.**

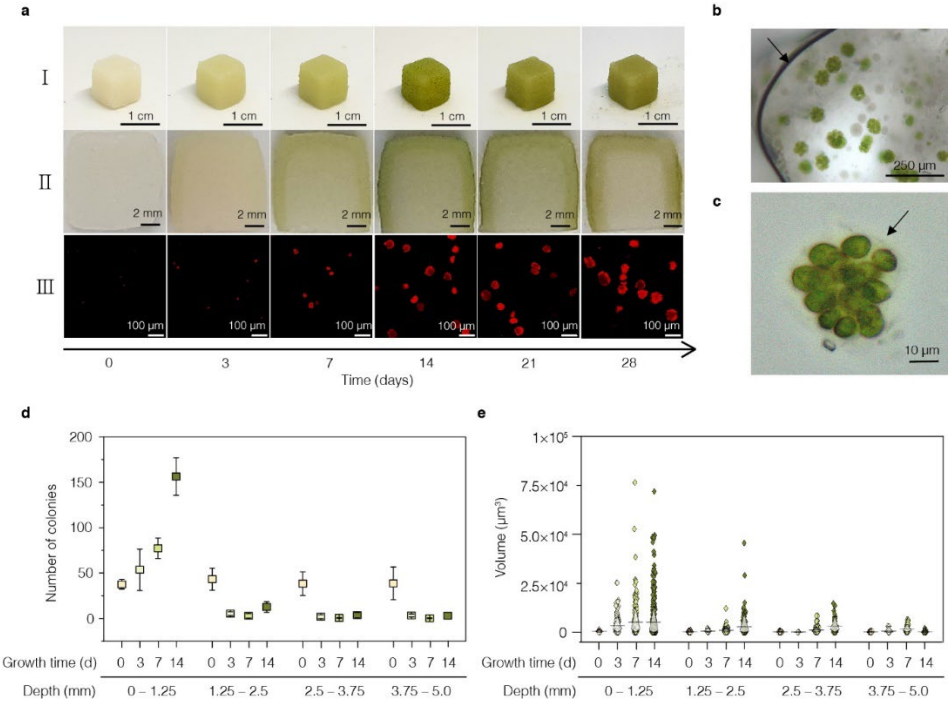

Figure 4.3. Growth and spatial distribution of embedded *C. reinhardtii* cells in cube-shaped ELMs (V = 1 cm³). (a) Time-series of ELM-maturation during 28 days under autotrophic conditions. Ⅰ. Macroscopic images of the ELMs. Ⅱ. Images of cross-sections of respective ELMs. Ⅲ. Confocal microscopic images showing chlorophyll autofluorescence of embedded cells approximately 100 µm below the surface of the ELM. (b) Light microscopic images of embedded cells around the outer periphery (black arrow) of a 14-day old cube, showing cells switched to the palmelloid life stage. (c) Light microscopic image of an individual cluster surrounded by a transparent extracellular matrix (black arrow). (d) The average number of colonies per 1.56 mm² area in relation to incubation time and distance to the cube surface (3 cubes per time point, whiskers extend to standard deviations). (e) Volume of colonies in relation to incubation time and distance to the cube surface. In (e), 3 cubes were used for the distributions, diamond boxes indicate 10 and 90 percentile values, and the horizontal lines in the middle indicate the mean.

The gradual decrease of 'greenness' towards the centre of the cube warranted further investigation of the location-specific growth of embedded *C. reinhardtii* cells (**Figure 4.3a**). The cube was divided into 4 zones ranging from topical periphery to the centre of the cube (Supporting Information). In each zone, the number of colonies was counted, and their volume was calculated assuming a spherical shape for the colonies. At day 0, an average of 40 colonies were counted in each zone (**Figure 4.3d**). Within three days, the number of colonies below 1.25 mm decreased to fewer than 12 and remained in this range until the end of the experiment. In contrast, the number of colonies within 1.25 mm from the surface

steadily increased, reaching 156 ± 20 at day 14. Simultaneously, with increasing depth, the volume of colonies decreased (**Figure 4.3e**). At day 0, the average calculated colony volume was approximately 358 μm^3, which represents a volume that would correspond to an individual *C. reinhardtii* cell[33]. In the periphery, the average volume of colonies increased gradually to 5,209 μm^3 within 14 days, while growth in the volume of colonies within increased depth was smaller. Notably, up to a depth of 3.75 mm, a few colonies were able to grow in volume at 14 days (**Figure 4.3e**). These results imply that the colonies close to the periphery tend to survive and grow as non-motile clusters while cells near the centre did not grow after three days, which is in correlation with the colour shift of the green cube periphery to the white cube centre.

4.2.3. EXPLORING THE LIMITING FACTORS FOR EMBEDDED *C. REINHARDTII* CELL GROWTH

To explore whether the reduced autotrophic growth of algae in the centre of the ELM cube is due to limited penetration of light and/or CO_2, ELM shapes with different thicknesses or improved gas exchange were tested and colony growth was examined. 2 mm thick plate-shaped ELMs containing cells were deposited on a solid plastic surface to prevent air transfer at the bottom (**Figure 4.4a**) and placed under LEDs mainly composed of blue (453 nm) and red (631 nm) light. A light sensor placed below the ELM-plate measured light transmission across 2 mm of ELM material. The measured light intensity was reduced from 6.7 $\mu mol \cdot m^{-2} \cdot s^{-1}$ to 2.5 $\mu mol \cdot m^{-2} \cdot s^{-1}$ at 453 nm, from 13.3 $\mu mol \cdot m^{-2} \cdot s^{-1}$ to 7.7 $\mu mol \cdot m^{-2} \cdot s^{-1}$ at 631 nm, accounting a 62 % and 43 % reduction, respectively (**Figure 4.4b**). *C. reinhardtii* was shown to be able to grow at similar light regimes in where a total intensity is sufficient for growth of *C. reinhardtii* cells[34]. After 14 days, light attenuation was increased to around 70 % and 50 %, respectively (**Figure S4.7**), likely from cell growth at the outer periphery. Despite sufficient light transmission to inner layers, no significant increase in colony volume and greenness was observed at a depth between 1.5 to 2 mm after 14 days (**Figure 4.4c**). This suggests that light availability is not the only limiting growth factor in this layer.

Besides light attenuation, cells located in deeper layers may also face limited CO_2 availability. To investigate the role of CO_2 availability on growth of embedded algae, hollow ELM-hemispheres ('igloo' shaped) of 2 mm thickness with variable medium composition were designed (**Figure 4.4d**). ELM-hemispheres showed similar light penetration properties as ELM-plates of same thickness (**Figure S4.7**). The ELM-hemispheres were placed on a plasticware with two rectangular shaped holes (area: 2 mm × 3 mm) that allowed gas to enter and exit the inner space of the hemisphere.

After 14 days of incubation, both the outer and inner surface displayed significant growth of colonies (**Figure 4.4e**). However, colonies located in the intermediate depth of 0.5 – 1 mm from the surface showed less increase in volume compared to the ones in peripheries. These findings indicate that improved gas exchange indeed improves cell proliferation. To test this further, the experiment was repeated with ELM-hemispheres of identical architecture but containing an additional carbon source (acetate) from the Tris-acetate-phosphorous (TAP) medium. Here, the intermediate depth also presents increased growth like the periphery, showing that increased carbon availability also allows cells to grow in deeper layers (**Figure 4e,f**).

We increased the thickness of the hemisphere to 4 mm to test how cells in lower layers will cope with increased light attenuation (**Figure 4.4g**). Despite the improved ambient CO_2 availability due to the hollow architecture and the hole allowing gas exchange, cell growth at the inner periphery was highly reduced compared to that at the outer periphery after 14 days of incubation (**Figure 4.4h,i**). Indeed, only ~20 % of initial light intensity at 453 nm (and ~50 % at 631 nm) can reach the inner space of a freshly printed 4 mm ELM-hemisphere (**Figure S4.7**), which may further decrease with increased cell growth at the outer periphery. Light attenuation also similarly affects growth in 4 mm thick ELM-hemispheres with an additional carbon source (**Figure S4.8**). Taken together, light permeability and CO_2 diffusion are key factors to consider in photosynthetic ELM designs, especially when microalgae are grown autotrophically.

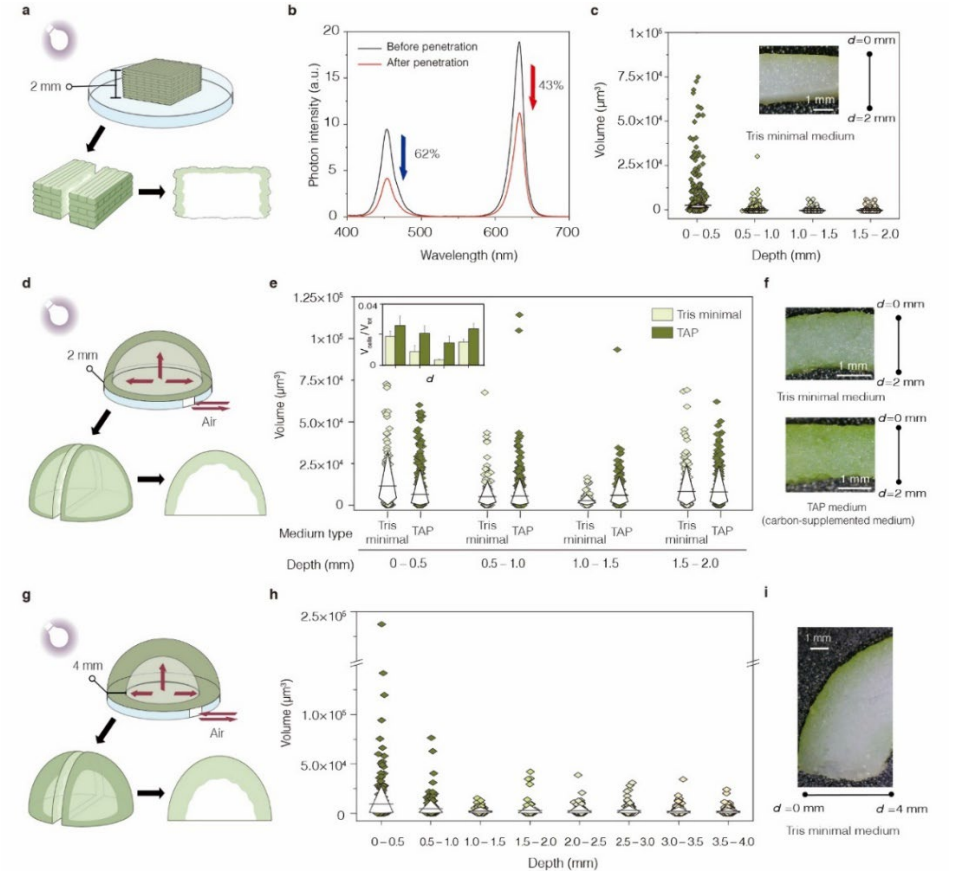

Figure 4.4. Exploring the limiting factors for growth of embedded *C. reinhardtii* cells in hydrogels. (a) Experimental design using 2 mm thick plate-shaped ELMs. (b) Light attenuation through a 2 mm thick plate shaped ELM containing algal cells at day 0. (c) Volume and spatial distribution of individual colonies in 2 mm thick ELM-plates with Tris minimal medium after 14 days, shown in relation to depth (*d*). A macroscopic image illustrates a typical cross-section used for measurements. (d) Experimental setup for 2 mm thick hollow ELM-hemispheres featuring a bottom opening for gas exchange. (e) Volume distribution of colonies in 2 mm thick hollow ELM-hemispheres after 14 days, analysed by depth and medium composition. Inset: average colony volume fraction (V_{cells}/V_{tot}) in Tris minimal (light green) or TAP (dark green). Error bars show standard deviations from three separate hemispheres. (f) Cross-section images of 2 mm thick hollow ELM-hemispheres incubated in Tris minimal (top) or TAP (bottom) medium for 14 days. (g) Experimental design for 4 mm thick hollow ELM-hemispheres (external radius: 10 mm, internal radius: 6 mm) with a bottom opening for gas exchange. (h) Volume distribution of colonies in 4 mm thick hollow ELM-hemispheres with Tris minimal medium after 14 days, shown by depth. (i) Cross-section image of a 4 mm thick hollow ELM-hemisphere after 14 days. In (c), (e), and (h), 3 samples were used for the distributions, with diamond boxes indicating 10–90 percentile values and horizontal lines showing the mean.

4.2.4. CO_2 CONSUMPTION PERFORMANCE OF PHOTOSYNTHETIC LIVING MATERIALS

The photosynthetic activity of microalgae embedded in ELMs can be indirectly monitored through consumption of ambient CO_2. The 1 cm^3 ELM-cubes were placed in a sealed glass container, illuminated with 12/12 h light/dark cycle at room temperature (~ 22 °C) while the CO_2 concentration within the container was measured in real-time for 5 days. The measured CO_2 concentration decreased during light exposure and increased during periods of darkness (**Figure 4.5a)**, implying that the embedded *C. reinhardtii* cells undergo photosynthesis and respiration while being illuminated, but mainly respiration while in darkness. Moreover, these measurements confirm that the cells endow photosynthetic capabilities to the ELM as a whole structure. Next, 3-, 7-, 14- and 42-day-old ELM-cubes were compared to test whether cell growth affects CO_2 consumption rate (**Figure 4.5b**). The 14-day-old cubes exhibited a statistically significant 2.7- and 1.2-fold higher CO_2 consumption performance than the 3-day-old and 7-day-old cubes ($p < 0.05$), respectively. Remarkably, 42-day old cubes still demonstrated photosynthetic activity. However, this longer incubation did not result in higher CO_2 capture performance, showing a similar level of CO_2 consumption rate compared to 3-day old cubes with lower cell numbers.

Since the colonies mostly grow at the periphery and cells in inner regions are less viable, a larger surface area might be helpful for the CO_2 consumption rate of ELMs. To test this, CO_2 consumption rate of three 14-day-old ELMs with different surface areas (hemisphere = 2.92 cm^2, cube = 5 cm^2, cuboid = 6.8 cm^2, excluding area facing the bottom) was measured while under 12 hours of illumination. The CO_2 consumption rate increases linearly with the exposed surface area of the ELM (**Figure 4.5c**), with average CO_2 consumption rates of 12.9 $ppm \cdot h^{-1}$ for the hemisphere, 23.3 $ppm \cdot h^{-1}$ for the cube, and 28.0 $ppm \cdot h^{-1}$ for the cuboid. The regression analysis revealed a high correlation between consumption rate and the ELM area with r^2 value of 0.96, showing that shapes with larger surface area are more beneficial for the photosynthetic activity of ELMs. Taken together, our data confirm our hypothesis that algal growth and metabolic activity in hydrogels can be modulated by the design of the ELM.

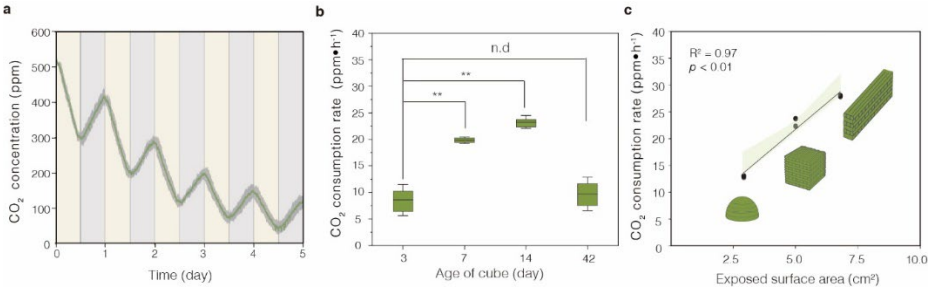

Figure 4.5. CO_2 consumption performance of photosynthetic living materials. (a) 5-day time-course of average CO_2 concentration in a closed system containing a 7-day-old ELM-cube. The dark green line indicates the average from triplicate results, while shaded regions indicate standard deviation. A beige background represents a light intensity of 20 µmol·m^{-2}·s^{-1}, while a grey background represents darkness. (b) Comparison of average CO_2 consumption rate of 3-, 7-, 14-, and 42-day-old cubes per hour during the first 12 hours of illumination (n = 3; the box represents 25th and 75th percentile values, horizontal lines in the middle indicate mean, and whiskers extend to standard deviation). One-way (single factor) ANOVA with post-hoc Tukey's HSD was used for statistical analysis; *n.d.* and ** indicate not significant and p < 0.01, respectively. (c) Relationship between the exposed surface area of differently shaped ELMs and average CO_2 consumption rate per hour (n = 3; shaded areas indicate a pointwise 95% confidence interval on the fitted values). The bioprints shaped as a hemisphere (r = 6.8 mm; exposed surface area = 2.91 cm^2), cube (10 mm × 10 mm × 10 mm; exposed surface area = 5 cm^2), and cuboid (4 mm × 25 mm × 10 mm; exposed surface area = 6.8 cm^2) were 14 days old at the start of the experiment.

4.2.5. DISCUSSION

Growth of cells within our microalgal ELMs showed a strong spatial dependence. Cells were found to dominate the outer periphery, especially when no additional carbon source (acetate) was provided. Limited gas diffusion and light attenuation caused reduced growth in deeper and/or central layers (depending on ELM architecture). The magnitude of light attenuation in deeper layers is dependent on the hydrogel thickness and is further attenuated by self-shading effects induced by colony growth in more mature ELMs. To better understand the geometrical parameters affecting microalgal growth, we prepared ELMs of different dimensions and shapes and found profound effects on *C. reinhardtii* cell growth and productivity. In his 1917 book, Thompson argued that physical forces play a critical role in shaping biological forms[35]. We also found that shapes with a higher surface area showed a higher CO_2 consumption rate, likely due to a higher number of cells exposed to favourable light and gas diffusion.

Interestingly, also in fungal and bacterial ELMs, functionality was found to be strongly linked to micro and/or macroscopic structure and composition. For example, modulating sphericity of embedded *E. coli* colonies through tuning mechanical stiffness of hydrogel matrices led to higher protein productivity[36]. Taking advantage of 3D printing, lattice-structured hydrogels had improved mass transfer of nutrients, which increased yield of desired metabolic products from embedded yeast[22]. And recent work on the 3D shaping of mycelium-laden hydrogels also highlighted how branching cells can benefit from porous scaffolds that facilitate hyphal growth and interconnection, leading to regenerative 3D ELMs[18, 37].

For photosynthetic ELMs, a thin, plant-leaf like architecture may be beneficial for homogenous cell growth and resulting higher productivity per fixed volume. In plant leaves, the primary site of photosynthesis, is the palisade parenchyma, which is located below the upper epidermis of the leaf, which highlights the importance of light availability even in thin photosynthetic structures. Furthermore, gas exchange is regulated by stomata pores at the lower epidermis of plants. In this work, 3D printing allows us to be flexible in realizing beneficial shapes. A first attempt to steer cell growth was our hollow ELM-hemispheres which feature a small, though unregulated opening for gas exchange which visibly improved cell growth in the inner layers. Growth was further increased with providing an acetate source incorporated in the ELM, which shows that photosynthetic growth of autotroph

ELMs would likely be even higher if CO_2 availability was further improved through features such as a porous architecture. However, improved gas exchange is in counterbalance with accelerated dehydration. This explains why the stomata in leaves open and close to improve gas exchange depending on plants' need whilst limiting dehydration. Leaves are also protected by a water-impenetrable wax-layer called cuticle, which is yet to be incorporated into our ELMs. Similar responsive additions to photosynthetic ELMs would likely benefit their longevity and photosynthetic productivity. Understanding microalgae growth within ELMs enables the development of fully controllable photosynthetic ELMs, which represent new solutions for oxygenating engineered tissues and organoids, and for energy pro

4.3. CONCLUSION

This work highlights that understanding the microbial response within 3D objects can help optimize ELM structures. A 3D printable hydrogel was developed whose structural integrity was further increased post-printing via crosslinking, allowing higher shaping. 3D mapping of microbial growth within ELMs is found to be key to identifying factors limiting cell growth, hence revealing ELM shape parameters (e.g., form, size) for improved ELM functionality. In photosynthetic ELMs, carbon source availability and light penetration are both found to be limiting growth. Shaping ELMs in thin leaf-like structures, thereby maximizing surface to volume ratio, reduces the parts of ELMs with lower cell growth. Those plant-inspired structures could lead to high efficiency of photosynthesis in terms of CO2 consumption and pave the way for new carbon capturing functional materials.

4.4. MATERIALS AND METHODS

Materials: Hutner's trace elements were purchased from Chlamydomonas Resource Center. Microcrystalline cellulose- and sodium carboxymethylcellulose-based thickener (MCG, VIVAPUR® MCG 811 PV) was provided by JRS Pharma. Other chemical reagents used in this study (tris base, acetic acid, ammonium chloride, magnesium sulphate heptahydrate, dipotassium phosphate, monopotassium phosphate, calcium chloride dihydrate, 37% hydrochloric acid solution, dried-powder of κ-carrageenan, sodium alginate from brown algae, and agar) were purchased from Sigma-Aldrich.

Strain and culture conditions: *C. reinhdardtii* CC-125 wild type mt(+) used in this study was obtained from Chlamydomonas Resource Center (USA). Microalgal cells were grown in a Tris minimal medium modified from previously[38], (Tris: 2.42 $g \cdot L^{-1}$, salts solution (NH_4Cl: 5 $g \cdot L^{-1}$, $MgSO_4 \cdot 7H_2O$: 4 $g \cdot L^{-1}$, and $CaCl_2 \cdot 2H_2O$: 2 $g \cdot L^{-1}$) 25 $mL \cdot L^{-1}$, phosphate solution (K_2HPO_4 288 $g \cdot L^{-1}$, KH_2PO_4 144 $g \cdot L^{-1}$) 375 $\mu L \cdot L^{-1}$, Hutner's trace elements 1 $mL \cdot L^{-1}$; pH adjusted to 7.0 with hydrochloric acid) for growth under autotrophic conditions, or in TAP (tris-acetate-phosphate) medium (identical to our Tris minimal medium except that the pH is adjusted to 7.0 with acetic acid) for growth under mixotrophic conditions. Liquid cultures with continuous air bubbling at room temperature (22 °C) were grown under a 12/12 light-dark cycle with an intensity of 20 $\mu mol \cdot m^{-2} \cdot s^{-1}$ using PAR30S LEDs (Philips, The Netherlands).

Bio-ink preparation: Hydrogel networks for bioprinting were formulated with either Tris minimal or TAP medium containing 1.5% (w/v) κ-carrageenan, 1.5% (w/v) sodium alginate, 1.5% (w/v) agar, and 3% (w/v) cellulose-based thickener. The thickener was dispersed into the media, mixed with a 1,000W Tristar MX-4828 hand blender at 16,000 rpm for 5 minutes, and rested for 15 minutes to ensure saturated swelling. Other hydrogel precursors were put individually with the following sequence: κ-carrageenan, sodium alginate, and agar. Each was mixed for 5 minutes and rested for 2 minutes, respectively. The resulting mixture with paste-like texture was autoclaved, conditioned at 30°C for two days, and finely fragmented into granules with the blender for 5 min. Living microalgal cells grown in liquid cultures were harvested using a centrifuge at 3,220 xg for 5 minutes. Cell pellets were resuspended in 100 µL of Tris minimal media and transferred into the hydrogel matrix for bio-ink fabrication just prior to printing, resulting in a final concentration

of 6.67 × 105 cells·g-1. The bio-ink was loaded to a 10-mL syringe and then degassed by centrifugation at 1,690 xg for 1 minute.

Three-dimensional printing of bio-ink: Three dimensional objects were fabricated with the following sequence: Computer-aided 3D (CAD) drawings, direct-ink writing, and Ca^{2+} crosslinking. The free online CAD program, TinkerCAD, was used to design 3D drawings of objects. Pre-designed patterns and geometries with .stl file format were sliced using the Cura slicer engine in Repetier-Host (Hot-World GmbH & Co. KG., Germany) to generate G-code commands compatible with a modified Geetech A10 Pro 3D printer. Theoretical calculation of surface and volume of designs were also conducted with .stl file formats in the python console of FreeCAD.

A three-dimensional printer was modified by changing the filament hot-end part to a piston-based syringe pump and holder. The 10-mL syringe loaded with bio-ink was connected with a MetcalTM 18-gauge dispensing tip and fixed into syringe holders. The printing speed of bio-ink and travel speed was 20 mm/s and 200 mm/s, respectively, and every single layer of bioprints was deposited with a height of 0.5 mm. The resulting bioprints were immersed within varying concentrations of CaCl2 solutions (0.1 M - 0.5 M) for 5 mins and 60 mins to crosslink polymers of hydrogels. After 3D printing, cell viability was checked with the fluorochrome SYTOX Green. The specific staining procedures are further described in the Supporting Information.

Bioprint incubation: The 3D bioprints were subjected to two incubation conditions: air exposure and immersion in Tris minimal media. Air-exposed bioprints were enclosed in petri dishes sealed with parafilm. For immersion, each cube was placed into 10 mL of Tris minimal media in 6-well plates. All bioprints were maintained under 20 $\mu mol \cdot m^{-2} \cdot s^{-1}$ at 12/12 h light/darkness interval using SQ100 LEDs (LUMERITM, The Netherlands, the number of red and blue LED in a 5:1 ratio).

Light intensity measurement: To measure light absorption of bioprints with and without cells, both a CCS100 spectrometer (Thorlabs, Germany) and a LI-190R Quantum Sensor (LI-COR Biosciences, USA) were used. The sensor was placed directly under the petri dish containing the bioprint (2 mm thick plate-shaped ELMs,

and 2 and 4 mm thick hollow ELM-hemispheres). Plastic plates without bioprints were used as blank.

Cell imaging and image analysis: C. reinhardtii encapsulated within hydrogel networks were imaged using both a light microscope (Frederiksen Scientific, Denmark) and a confocal microscope (Nikon confocal A1R/SIM, Japan). For confocal microscopy, a laser with wavelength of 561 nm was set to excite chlorophyll and emission was collected with a band-pass filter at 561 ± 71 nm. The resonant scanning mirror was chosen for fast acquisition of real-time imaging to prevent desiccation induced hydrogel deformation. The obtained images were analysed using the built-in functions of Fiji 2.9.0 to measure the size of cells or cell clusters. The detailed workflow of quantification using Fiji is given in the Supporting Information.

CO_2 measurement: Individual bioprint inside a 60 mm diameter petri dish sealed with parafilm were placed inside a closed CO_2 measurement system. They were maintained under 20 $\mu mol \cdot m^{-2} \cdot s^{-1}$ at 12/12 h light/dark cycle using Grow light LEDs (ABC-LED, The Netherlands, the number of red and blue LED in a 5:1 ratio). Information of the closed CO2 measurement system is provided in the Supporting Information.

Rheology test: The viscoelastic properties of hydrogel networks with and without microalgae were analysed using circle plate-shaped prints (diameter: 20 mm, and height 2 mm) loaded onto a strain- and stress-controlled rheometer (Thermo Scientific HAAKE MARS III). Serrated plates of 20 mm diameter were used to prevent wall slip during the measurements with a gap height of 1 mm. Storage (G') and loss moduli (G") were determined as a function of shear strain via oscillatory amplitude sweeps at a fixed frequency of 1 Hz with a sweep of strain (0.1 - 10000 %). The yield stress of the inks was determined by applying a stress-controlled deformation to the sample and measuring the resulting shear strain. The yield stress was measured using the tangent crossover method in the log-log plots. The elastic recovery of the ink was measured using a time dependent oscillation-rotation-oscillation test. To simulate at rest behaviour, amplitude sweep was performed at a low shear stress within the linear viscoelastic regime for 1 minute followed by a high shear rate rotation (10 s^{-1}) for 30 s to simulate the time scales and stresses applied during

printing. Subsequently, the recovery in elastic moduli over time was measured with the low amplitude oscillatory sweep for 2 minutes.

Bridging ability of ink: To assess the bridging ability, a triangular support structure was printed based on Kleger et al. [27], followed by printing 12 spanning filaments across the support structure with a gap of 1.5 mm between them. To evaluate the sagging behaviour, the deflection of the filaments was imaged using a VR-5000 Optical Profilometer (Keyence, Germany). The spanning length of the filaments was measured by analysing the image from the profilometer via Fiji. The storage modulus of the ink after recovery obtained from recovery test was used to calculate the theoretical deflection. The experimental deflection was compared to the calculated theoretical deflection and extrapolated using fit factors.

Statistical Analysis: Any pre-process was conducted for data presentation. Colony number (Figure 3d) in cube-shaped ELMs and CO_2 consumption data (Figure 5a, 5b) are shown as mean ± standard deviation. Average CO_2 consumption rates (in Figure 5b) were statistically analysed with one-way (single factor) ANOVA with post-hoc Tukey's HSD on the online statistical calculators https://astatsa.com

4.5. SUPPORTING INFORMATION

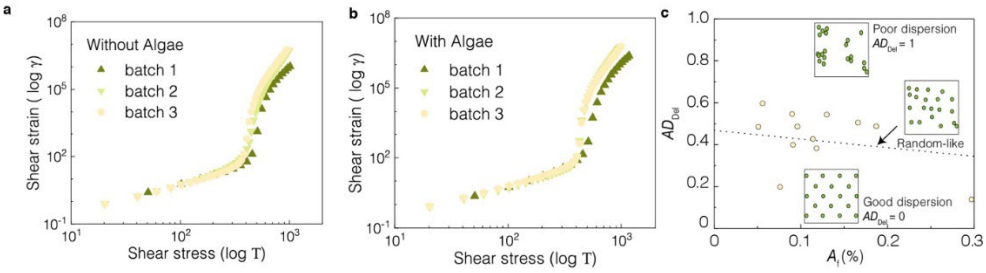

Figure S4.1. Ink preparation repeatability. Flow behaviour of three different ink batches depending on microalgae incorporation. Ink batches without microalgae (a) and with microalgae (b) indicate yield stress of 387.7 ± 26.7 and 396 ± 14.1 Pa, respectively, confirming high repeatability of preparation process. In addition, weight fraction of microalgal cell in bioink was estimated around 0.03%. c) Microalgae dispersion in bioprints, indicating that most samples showed a random-like to good dispersion[1]. Cells within cross-section of 0-day bioprints were imaged following Experimental Section 3 of the Supporting Information, and dispersion was evaluated following a previous study[1]. AD_{Del} indicates the area disorder of the Delaunay network, generated from microalgal cell positions within a cross-section of micrograph. A_f indicates the area fraction of the cross-section micrograph covered by microalgal cells.

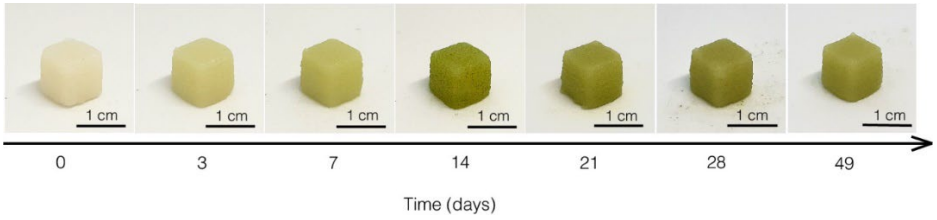

Figure S4.2. **Long-term macroscopic examination of cube-shaped ELMs** (V = 1 cm3). Time-series of ELM-maturation during 49 days under autotrophic conditions.

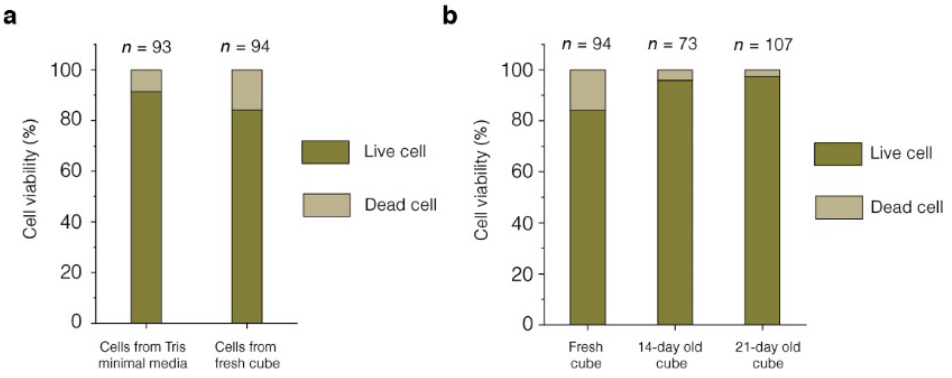

Figure S4.3. Cell viability. (a) Viability of *C. reinhardtii* cells grown in Tris minimal media for 7 days, and of *C. reinhardtii* cells subjected to the process of 3D printing and crosslinking in 0.2 M Ca^{2+} solution. (b) Viability of *C. reinhardtii* cells grown at outer periphery (within ~ 2 mm from cube surface). Viability measurements in a) and b) were conducted with SYTOX Green live/dead cells assays, as described in Experimental Section 2 of Supporting Information and *n* indicates the number of cells counted for each experiment.

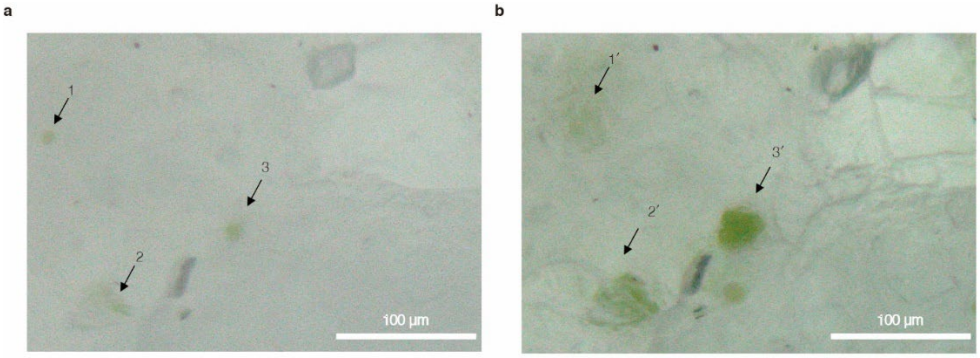

Figure S4.4. Formation of palmelloids in hydrogels. Time-lapse images of *C. reinhardtii* cells at the same position in (a) 0-day-old and (b) 3-day-old crosslinked hydrogels. Existing unicellular *C. reinhardtii* 1, 2, and 3 form a cell cluster of 1', 2', and 3' inside crosslinked hydrogels, respectively.

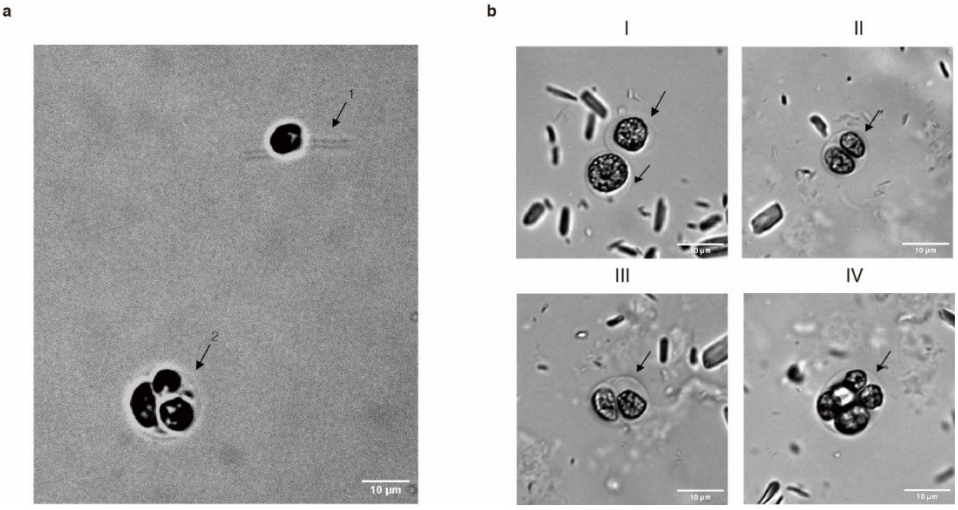

Figure S4.5. Palmelloid state of embedded *C. reinhardtii* cells. (a) Light microscopic images of *C. reinhardtii* CC125 cells in 14-day-old Tris minimal medium liquid culture, in which 1 points to a flagellated cell, and 2 indicates a membrane-like structure encasing cells in the palmelloid state. No flagella were observed in palmelloid state cells. (b) Light microscopic images of *C. reinhardtii* cells released from 7-day-old crosslinked hydrogels. Cross-sectional cuts were put in a 1.5 mL tube and were partially dissolved with 200 µL of 10 mM EDTA and gentle pipetting, as described in Experimental Section 2 of Supporting Information. Non-flagellated cells were encased in a single membrane-like structure, including single (I), double (II and III) or multiple cells (IV) per structure, respectively.

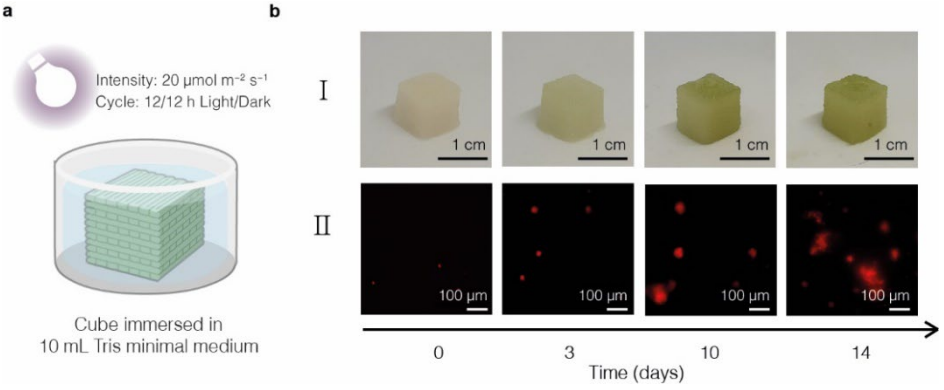

Figure S4.6. Growth of embedded *C. reinhardtii* cells in immersed cube-shaped ELMs (V = 1 cm^3). (**a**) Incubation conditions of immersed ELMs. (b) Time-series of ELM-maturation during 14 days under autotrophic conditions. Ⅰ. Macroscopic images of the ELMs. Ⅱ. Confocal microscopic images showing chlorophyll autofluorescence of embedded cells approximately 100 µm below the surface of the ELM.

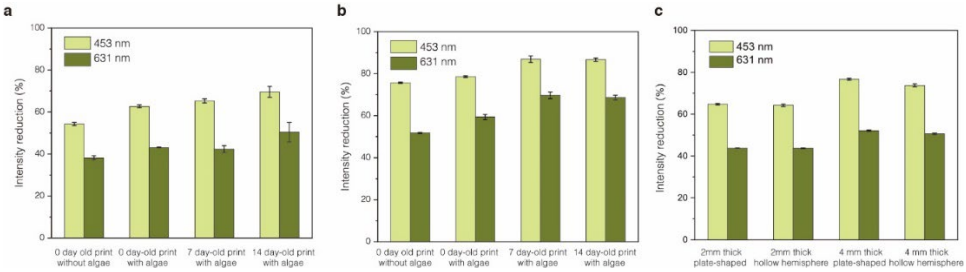

Figure S4.7. **Light attenuation by ELM matrix formulated with Tris minimal medium and shading effects of grown colonies at outer periphery**. (a) Light attenuation after penetration through a 2 mm thick plate-shaped prints depending on microalgae integration and growth time. (b) Light attenuation after penetration through a 4 mm thick plate-shaped prints depending on microalgae integration and growth time. (c) Light attenuation after penetration through a 0-day-old bioprints depending on thickness and shape.

4.A.1. ANALYSES OF BRIDGING

For a simply supported beam of length L and diameter D with uniform load w/L, the maximal z-deflection is expressed as[2]

$$\delta z_{max} = \frac{5wL^4}{384El}$$

where $l = \frac{\pi D^4}{64}$ is the cross-sectional momentum of inertia, and $E = (1 + 2v)G$ is the Young's modulus of the beam material. For an isotropic viscoelastic material, the Poisson's ratio v is taken as 0.5 and the shear modulus G is approximated by G_0. In the case of a spanning paste filament, the load is expressed as $w = \frac{D^2}{4}\pi\rho_{paste}g$, where g is the gravitational acceleration constant and ρ_{paste} is the density of the bioink (a hydrogel with a cell density of 6.67 × 10^5 cells/g)[2].

The maximum deflection of a spanning filament can hence be estimated by introducing the relations above into above equation to give the following equation.

$$\delta z_{max} = \frac{a}{G_0}\frac{5}{12}(0.25\rho_{paste}g\frac{L^4}{D^2})$$

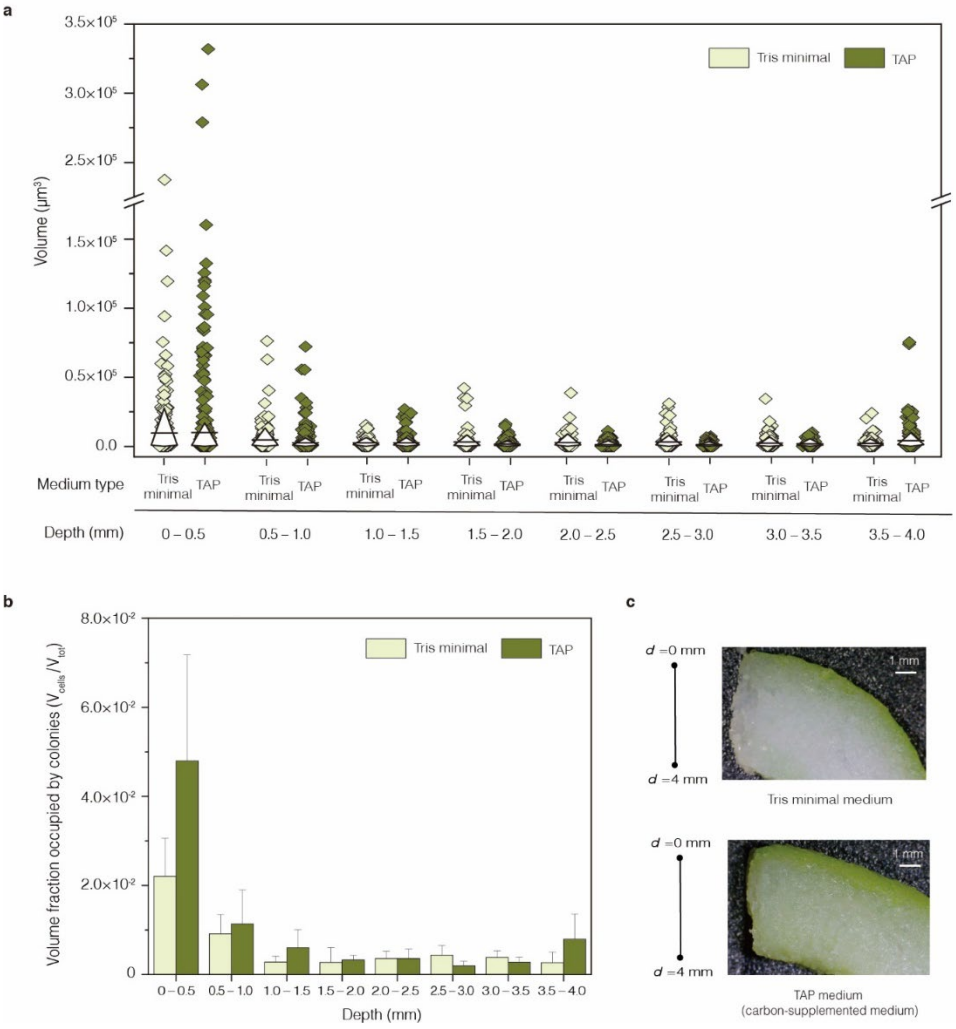

Figure S4.8. Location specific growth of microalgae within hollow ELM-hemispheres with 4 mm thickness after an incubation time of 14 days. (a) Volume distribution of individual colonies embedded in 4 mm thick hollow ELM-hemispheres formulated with Tris minimal medium or TAP medium in relation to depth (diamond boxes indicate 10 and 90 percentile values and horizontal lines in the middle indicate mean). (b) Average volume fraction occupied by colonies (V_{cells}/V_{tot}) in 4 mm thick ELM-hemispheres hydrogels in either Tris minimal medium (light green) or TAP medium (dark green), depending on depth. Error bars represent standard deviations from measurements of three separate hemispheres. (c) Macroscopic image of cross-section of 4 mm thick hollow ELM-hemisphere formulated with Tris minimal medium after an incubation time of 14 days.

4.A.2. SYTOX STAINING PROCEDURES FOR CELL VIABILITY MEASUREMENT

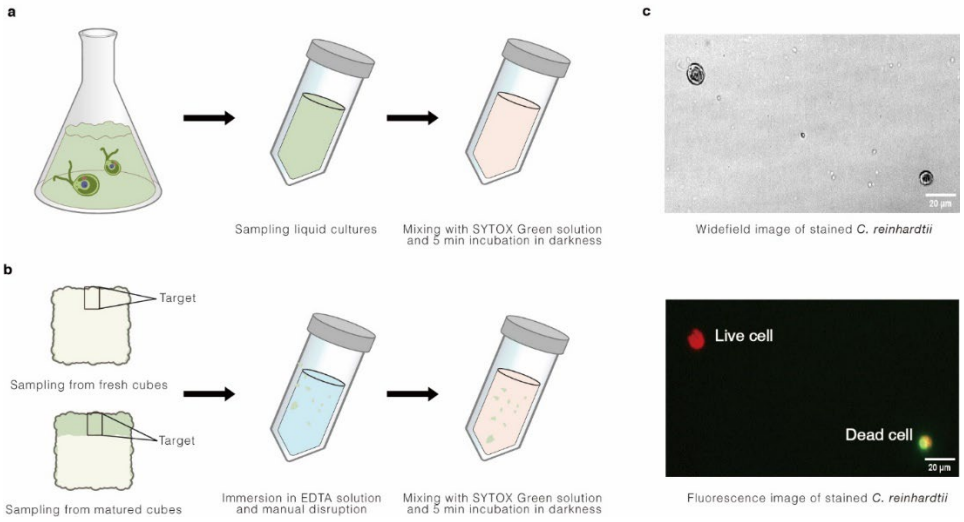

Figure S9. Method of SYTOX Green live/dead cell staining[3]. (a) Liquid culture was stained by direct application of 1 µL SYTOX Green (dissolved in 5 mM dimethyl sulfoxide) to 1 mL of liquid culture. SYTOX Green can bind nucleic acids, while it is unable to penetrate intact cell membranes. After an incubation period of 5 min in darkness, a sample can be investigated under a fluorescence microscope. (b) To stain cells in cube periphery, a 1 × 1 × 0.1 cm^3 cross-sectional cut from the periphery of cubes of different maturation stages was placed in a 1.5 mL tube. 200 µL of 10 mM EDTA was added to the tube and the sample partially dissolved by pipetting. After addition of 0.2 µL SYTOX Green solution, the sample was incubated for 5 min in darkness and was then investigated under a microscope. c) Microscopic widefield (top) and fluorescence (bottom) images of a stained liquid sample, showing both live and dead cell indicated by red chlorophyll autofluorescence, and a dead cell indicated by green SYTOX Green fluorescence. Excitation/Emission: Chlorophyll – 562/593 nm, SYTOX Green – 482/520 nm. Cells were imaged with an IX81 inverted microscope (Olympus, Japan).

4.A.3. ANALYSIS OF LOCATION SPECIFIC GROWTH OF EMBEDDED CELLS IN HYDROGEL BASED ON AUTOMATIC CONFOCAL MEASUREMENT AND BUILT-IN FUNCTIONS OF FIJI

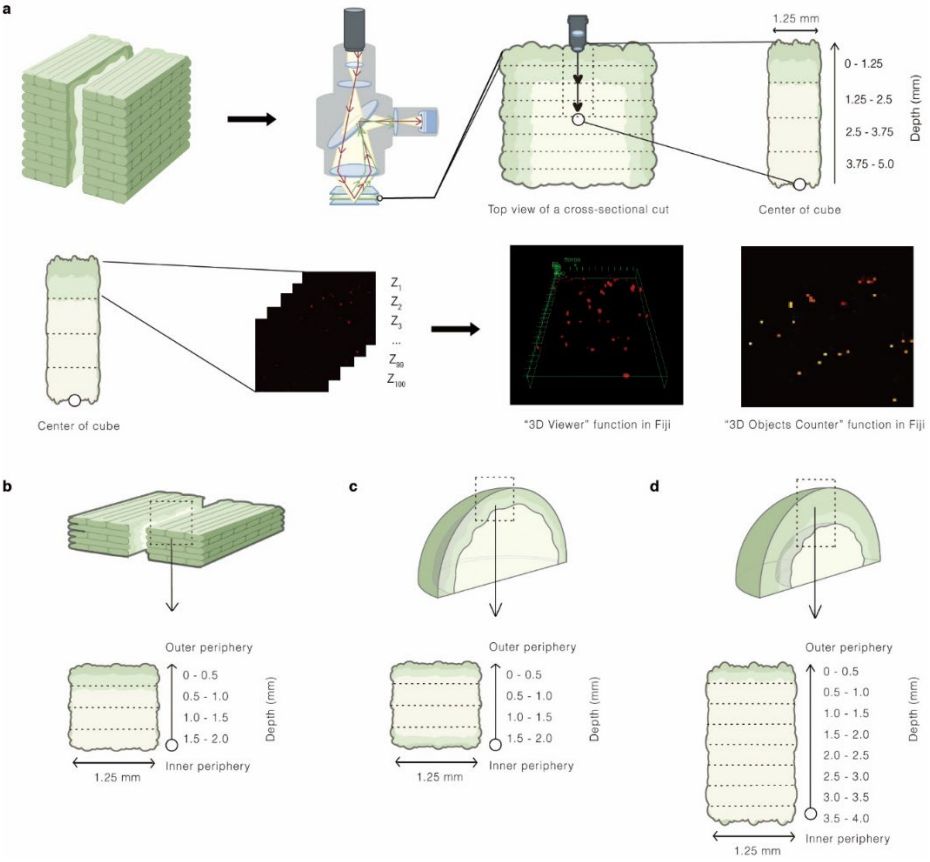

Figure S10. Method of cell imaging and image analysis for growth characterization of *C. reinhardtii* embedded in hydrogels. (a) A 1 × 1 × 0.1 cm^3 cross-sectional cut from a 1 cm^3 3D printed cube was virtually split. The 4 spots from the outer periphery to the centre of the cube contain four different depth zones. Automatic confocal laser microscopy image acquisition was conducted on 4 square spots. Each spot contains serial z-stack sectioning for up to 100 images at 1-µm intervals. Using the "3D viewer" built-in function of Fiji software[4], the embedded cells in each spot can be 3D imaged. Further, "3D Objects Counter" function with automatic threshold set-up can give the number and volume of colonies inside hydrogels. (b, c, and d) represents the method of obtaining cross-sectional cut from ELM plates with 2 mm thickness and hollow ELM-hemispheres with 2 mm and 4 mm thickness. Each spot contains serial z-stack sectioning for up to 50 images at 1-µm intervals.

4.A.4. METHOD FOR CO_2 MEASUREMENT IN REAL TIME

A closed CO_2 measurement system consisted of a glass container of 0.2 L volume, a SCD30 non-dispersive infrared sensor (Sensirion, Switzerland), and wireless charging coils for power supply. The SCD30 module features a dual-channel principle in which one channel is specific to carbon dioxide only and another for blank, allowing specific measures to carbon dioxide only. The module was calibrated prior to CO_2 measurement following the manufacturer's instructions. A 38 kHz modulated infrared light communication allowed the data transfer from the sensor to the computer through the glass container. A microcontroller board, Beetle Arduino, was used to control the sensor and transfer the infrared signal to a receiver. Outside the glass container, the plastic scaffold contains Grow LEDs and an infrared receiver demodulator, which was connected to a Mega Arduino to collect the data through a universal serial bus to a computer that used the open-source software CoolTerm 2.0.

4.6. REFERENCES:

[1] P. Gruber, J. Vincent, A.C.J. Vermeulen, T. Speck, Aspects of Life, in: B. Imhof, P. Gruber (Eds.), Built to Grow: Blending architecture and biology, Birkhäuser, Basel, **2016**.

[2] P. Q. Nguyen, N. M. D. Courchesne, A. Duraj-Thatte, P. Praveschotinunt, N. S. Joshi, *Adv. Mater.* **2018**, *30*, 1704847.

[3] A. Rodrigo-Navarro, S. Sankaran, M. J., Dalby, A. del Campo, M. Salmeron-Sanchez, *Nat. Rev. Mater.* **2021**, *6*, 1175.

[4] W. V. Srubar III, *Trends Biotechnol.* **2021**, *39*, 574.

[5] B. Pabst, B. Pitts, E. Lauchnor, P. S. Stewart, *Antimicrob. Agents Chemother.* **2016**, *60*, 6294.

[6] H. Priks, T. Butelmann, A. Illarionov, T. G. Johnston, C. Fellin, T. Tamm, A. Nelson, R. Kumar, P. J. Lahtvee, *ACS Appl. Bio Mater.* **2020**, *3*, 4273.

[7] S. Zhao, C. Guo, A. Kumarasena, F. G. Omenetto, D. L. Kaplan, *ACS Biomater. Sci. Eng.* **2019,** *5*, 4808.

[8] F. Krujatz, A. Lode, S. Brüggemeier, K. Schütz, J. Kramer, T. Bley, M. Gelinsky, J. Weber, *Eng. Life Sci.* **2015**, *15*, 678.

[9] A. Lode, F. Krujatz, S. Brüggemeier, M. Quade, K. Schütz, S. Knaack, J. Weber, T. Bley, M. Gelinsky, *Eng. Life Sci.* **2015**, *15*, 177.

[10] S. Malik, J. Hagopian, S. Mohite, C. Lintong, L. Stoffels, S. Giannakopoulos, R. Beckett, C. Leung, J. Ruiz, M. Cruz, B. Parker, *Global Chall.* **2020**, *4*, 1900064.

[11] C. Kwak, S. Y. Ryu, H. Park, S. Lim, J. Yang, J. Kim, J. H. Kim, J. Lee, *J. Colloid Interface Sci.* **2021**, *582*, 81.

[12] F. He, Y. Ou, J. Liu, Q. Huang, B. Tang, F. Xin, J. Zhang, M. Jiang, S. Chen, Z. Yu, *Small* **2022**, *18*, 2104820.

[13] V. Kumar, M. S. Vlaskin, A. V. Grigorenko, *Trends Biotechnol.* **2021,** *39*, 1243.

[14] X. Chen, J. M. Lawrence, L. T. Wey, L. Schertel, Q. Jing, S. Vignolini, C. J. Howe, S. Kar-Narayan, J. Z. Zhang, *Nat. Mater.* **2022**, *21*, 811.

[15] S. Maharjan, J. Alva, C. Cámara, A. G. Rubio, D. Hernández, C. Delavaux, E. Correa, M. D. Romo, D. Bonilla, M. L. Santiago, *Matter* **2021**, *4*, 217.

[16] D. Datta, E. L. Weiss, E.L., D. Wangpraseurt, E. Hild, S. Chen, J. W. Golden, S. S. Golden, J. K. Pokorski, *Nat. Commun.* **2023,** 14, 4742.

[17] S. Balasubramanian, K. Yu, A. S. Meyer, E. Karana, M. E. Aubin-Tam, *Adv. Funct. Mater.* **2021**, *31*, 2011162.

[18] S. Gantenbein, E. Colucci, J. Käch, E. Trachsel, F. B. Coulter, P. A. Rühs, K. Masania, A. R. Studart, *Nat. Mater.* **2023**, *22*, 128.

[19] S. Balasubramanian, M.-E. Aubin-Tam, A. S. Meyer, *ACS Synth. Biol.* **2019**, *8*, 1564.

[20] O. Jeon, Y. Bin Lee, H. Jeong, S. J. Lee, D. Wells, E. Alsberg, *Mater. Horiz.* **2019**, *6*, 1625.

[21] A. Lee, A. Hudson, D. Shiwarski, J. Tashman, T. Hinton, S. Yerneni, J. Bliley, P. Campbell, A. Feinberg, *Science* **2019**, *365*, 482.
[22] F. Qian, C. Zhu, J. M. Knipe, S. Ruelas, J. K. Stolaroff, J. R. DeOtte, E. B. Duoss, C. M. Spadaccini, C. A. Henard, M. T. Guarnieri, S. E. Baker, *Nano Lett.* **2019**, *19*, 5829.
[23] J. L. Fredricks, H. Iyer, R. McDonald, J. Hsu, A. M. Jimenez, E. Roumeli, *J. Polym. Sci.* **2021**, *59*, 2878.
[24] N. Diamantides, C. Dugopolski, E. Blahut, S. Kennedy, L. J. Bonassar, *Biofabrication* **2019**, *11*, 045016.
[25] D. Petta, A. R. Armiento, D. Grijpma, M. Alini, D. Eglin, M. D'Este, *Biofabrication* **2018**, *10*, 44104.
[26] D. Wangpraseurt, S. You, F. Azam, G. Jacucci, O. Gaidarenko, M. Hildebrand, M. Kühl, A. G. Smith, M. P. Davey, A. Smith, D. D. Deheyn, S. Chen, S. Vignolini, *Nat. Commun.* **2020**, *11*, 1748.
[27] N. Kleger, M. Cihova, K. Masania, A. R. Studart, J. F. Löffler, *Adv. Mater.* **2019**, *31*, 1903783.
[28] W. C. Ratcliff, M. D. Herron, K. Howell, J. T. Pentz, F. Rosenzweig, M. Travisano, *Nat. Commun.* **2013**, *4*, 2742.
[29] K. Iwasa, S. Murakami, *Physiol. Plant* **1968**, *21*, 1224.
[30] K. Iwasa, S. Murakami, *Physiol. Plantarum* **1969**, *22*, 43–50.
[31] T. Yoshitomi, S. Kaminaga, N. Sato, M. Toyoshima, T. Moriyama, K. Yoshimoto, *Plant Cell Physiol.* **2020**, *61*, 158.
[32] M. Al-Mossawi, H. Warren, P.J. Molino, P. Calvert, M. in het Panhuis, *Mater. Adv.* **2021**, *2*, 1369.
[33] M. Sandmann, A. Garz, and R. Menzel, *Botany* **2016**, *94*, 53.
[34] M. Vítová, K. Bišová, D. Umysová, M. Hlavová, S. Kawano, V. Zachleder, M. Čížková, *Planta* **2011**, *233*, 75.
[35] D. A. W. Thompson, *On Growth and Form,* Cambridge University Press, Cambridge, UK **1917**.
[36] S. Bhusari, S. Sankaran, A. Del Campo, *Adv. Sci.* **2022**, *9*, 2106026.
[37] A.R. Studart, and K. Masania, *Nat. Mater*. **2023**, *22*, 16.
[38] D.S. Gorman, and R.P. Levine, *Proc. Natl. Acad. Sci. USA* **1965**, 54, 1665-1669

5

THREE DIMENSIONAL-PRINTING OF LIVING, MECHANO-RESPONSIVE DINOFLAGELLATE INK

Embedding bioluminescent algae into engineered gels can enable the development of living, mechano-responsive materials. Here, we develop a 3D-printable bioink containing the dinoflagellate Pyrocystis pseudonoctiluca to fabricate living structures that respond to mechanical stimuli. By formulating alginate-based bioinks, we investigate how variations in alginate and cell culture concentrations influence rheological properties, printability, and mechanical stiffness. We identify a trade-off: while higher alginate concentrations enhance crosslinked stiffness, they also reduce printability, whereas increased cell culture concentrations improve cell density but alter ink rheology. To optimize formulation, we use yield stress as a key design parameter and propose a range of suitable values for 3D printing dinoflagellate bioinks. The printed and crosslinked geometries exhibit mechanoresponsive bioluminescence, with stiffer constructs emitting greater peak and total light intensities. Given that light emission is influenced by both shear stress and deformation rate, we highlight the need for further biophysical studies on dinoflagellate responses in viscoelastic environments. Our findings contribute to the development of functional bioluminescent materials, with potential applications in biosensing, stress visualization in structures, and soft robotic

This chapter is under preparation to be submitted as P. Srivastava, S. K. Ammu, S. Schyck, K. Masania, "3D Printing of tuneable dinoflagellate ink".

5.1. INTRODUCTION

The ability of living organisms to detect and respond to stimuli is crucial for their adaptability and survival. This inherent responsiveness presents an opportunity to develop engineered living materials (ELMs) that are not only sensitive but also require low energy to produce. Organisms such as algae and dinoflagellates are particularly robust, thriving in natural environments through processes like photosynthesis and demonstrating high sensitivity to mechanical stresses.[1]

Recent interest has grown in using these living organisms to create bio-hybrid materials for harnessing their functionalities[2,3]. This approach involves developing bio-inks that maintain cellular functions and viability while offering sufficient mechanical properties for 3D printing into complex structures. Recent work by Oh et al.[3] on 3D-printed *Chlamydomonas reinhardtii* examined how spatial constraints imposed by the 3D-printed hydrogel structure affect cell motility and photosynthesis at the interface. The study found that the cells tend to aggregate at the surface due to improved light availability and enhanced gas exchange, leading to increased CO_2 uptake with greater surface area. This highlights the benefits of creating complex 3D structures with engineered hydrogels to maximise performance.

There is a growing interest in using dinoflagellate species in ELMs, which can convert mechanical stress into bioluminescence, effectively functioning as living mechano-responsive materials[4,5]. Dinoflagellates are eukaryotic protists and among the fastest known mechanoresponsive systems, emitting light within 15 to 20 ms after experiencing mechanical shear stress on their cell walls[6]. Researchers have explored applications of this property; for e.g., Li et al.[4] explored the creation of biohybrid mechanoluminescent devices by encapsulating dinoflagellates into soft elastomeric chambers made of polydimethylsiloxane (PDMS). While these devices successfully emitted light in response to mechanical deformations and showed potential as mechanoluminescent sensors, the encapsulation method posed challenges, such as leakage risks, scalability issues, and difficulties in fabricating complex shapes.

To address these limitations, the researchers investigated ionically crosslinked alginate hydrogel as a matrix, known for its biocompatibility with cell cultures. This led to the development of highly responsive dinoflagellate inks capable of surviving with hydrophobic coatings. The resulting living composites demonstrated a lifespan

of approximately five months under harsh conditions, providing proof of concept for living mechano-responsive materials[5].

However, the effect of the hydrogel stiffness on the confinement and the ability of light production of the cells remains unexplored. In this study, we investigated the effects of 3D printing mechano-responsive engineered living inks containing the bioluminescent dinoflagellate *Pyrocystis noctiluca*. This non-motile marine phytoplankton was selected for its large cell size, which accommodates a high number of scintillons[7] responsible for bioluminescence. Additionally, *P. noctiluca* was chosen for its robustness, as demonstrated by previous research[4]

The study focused on tuning the mechanical properties of the hydrogel by varying alginate crosslinking concentrations and assessing their impact on the mechanical responsiveness of the dinoflagellates. Initially, the rheological properties of different ink formulations, along with the cell viability, were analysed. Subsequently, the study examined how variations in mechanical crosslinking and network rigidity influenced the light emission response to mechanical stimuli. The objective was to understand how these factors affect the performance and behaviour of the printed dinoflagellate inks, thereby providing deeper insights into how the surrounding medium influences the transfer of mechanical stress to the dinoflagellate cells and how cell confinement impacts the light produced in response to mechanical stress.

5.2. RESULTS AND DISCUSSION

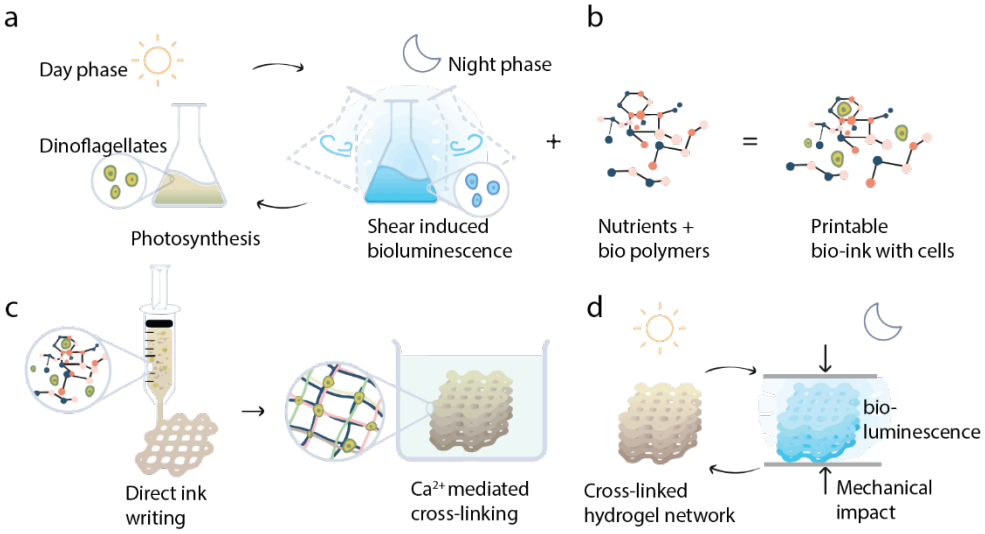

Figure 5.1: Schematic of the tuneable 3D printable ink with embedded dinoflagellate cells. (a) Cell cultures of dinoflagellates *P.noctiluca* exhibit photosynthesis during day phase and bioluminescence upon shear during night phase. (b) cells embedded inside hydrogels containing the required nutrients and printing aids (c) Crosslinking of alginate-based hydrogels using calcium chloride solution to form calcium crosslinks, enhancing mechanical stability (d) characterisation of spatial distribution and light emission from the inks under mechanical stress (illustration by Lipi Gupta).

To investigate the effect of hydrogel mechanical properties on dinoflagellate cell performance, ink formulations with varying concentrations of cross-linking agents were developed. Sodium alginate was chosen as both a rheology modifier and cross-linking agent due to its availability and widespread use in biomedical and food industries. The hydrogel base consisted of F2 medium combined with κ-carrageenan, sodium alginate, agar, and a cellulose-based thickener. Dinoflagellate cells from liquid cultures were then incorporated into this hydrogel and 3D printed using direct ink writing. This hydrogel formulation was inspired by Oh et al.[3], who successfully utilized a similar hydrogel to 3D print *Chlamydomonas reinhardtii* into spatially complex structures. Modifications were made to accommodate dinoflagellates, including the use of F2 medium. The objective was to engineer a 3D-printed matrix capable of resisting capillarity- and gravity-driven deformations, ensuring self-supporting structures while maintaining biocompatibility for the dinoflagellates.

Additionally, the amount of liquid cell culture integrated into the hydrogel affects both its rheological properties and the light emission of the living hydrogel. Since

the cells were present in a liquid culture, different amounts of liquid medium were added to the hydrogels (dilution) to simulate the effect of varying the cell culture concentration on the rheology. Together, this provides a base for tuning the hydrogel properties to optimise the light emission from the living hydrogel. The schematic **in Figure 5.1** encapsulates the workflow from the preparation of the bio-ink to the final application, highlighting the tunability of the system via alginate-based crosslinking to optimise both mechanical properties and bioluminescent responses.

5.2.1. EFFECT OF ALGINATE AND CELL CULTURE ON RHEOLOGICAL PROPERTIES OF DINOFLAGELLATE HYDROGELS

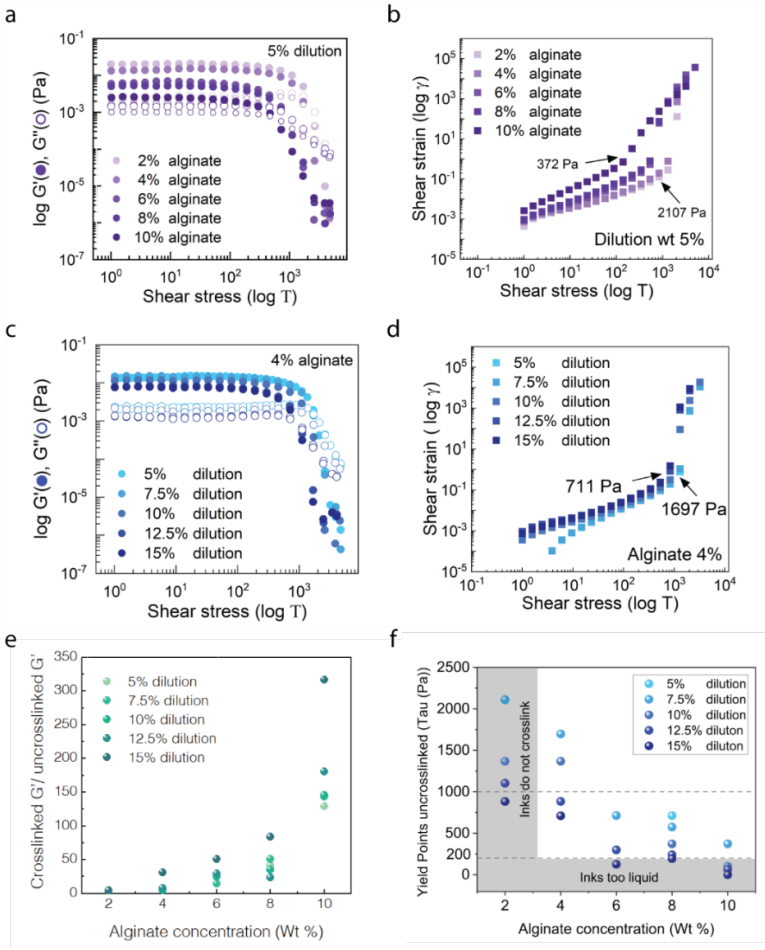

Figure 5.2. Rheological analysis of alginate-based hydrogels with varying alginate concentrations and dilution levels. (a) The storage modulus (G') decreases significantly as alginate concentration increases from 2% to 10%. (b) The shear strain increases, and the yield point decreases with higher alginate concentration, reflecting a transition toward a more fluid-like behaviour. (c) The effect of a higher concentration of cell culture dilutions for all the concentrations of alginate on the rheology of the inks was studied. For a constant 4% alginate concentration, a higher concentration of cell culture dilutions leads to a small decrease in G' (d). Similarly, increased dilution results in a reduced yield point. (e) The ratio of the storage modulus, G' of the crosslinked vs uncrosslinked inks shows no crosslinking at 2% alginate and a steady increase with alginate concentration and with dilution, highlighting the efficacy of crosslinking density on the mechanical strength. (f) Based on all the previous graphs, yield point analysis for different alginate and dilution concentrations shows that higher alginate concentrations result in stronger gels, while higher dilutions reduce the yield point, marking a transition to more liquid-like behaviour. The shaded area denotes conditions where hydrogels become too liquid to maintain structural integrity, emphasising the need for optimised alginate concentration and dilution to achieve desired mechanical properties.

The rheological properties of the bioinks were investigated to understand their suitability for direct ink writing, focusing on the effects of varying sodium alginate concentrations and the degree of dilution with cell culture medium. Dynamic amplitude sweeps were conducted to evaluate the storage modulus (G') and loss modulus (G''), to study the elastic versus viscous behaviour of the bioinks. The results demonstrated that increasing alginate concentration from 2% to 10 wt.% resulted in a significant decrease in G', indicating reduced elastic energy storage capacity, as shown in **Figure 5.2a**. This decrease in G' was attributed to the highly hydrophilic nature of the sodium alginate absorbing water from the autoclaving process, leading to swelling and a shift towards a more deformable structure under stress. Yield point analysis to study the stress required for the transition from elastic to plastic deformation, derived from the inflection point on the stress-strain curves, revealed that higher alginate concentrations led to lower yield points at lower stress levels, as depicted in **Figure 5.2b**.

Furthermore, the impact of varying the cell culture medium dilution at different alginate concentrations was examined. At a constant alginate concentration of 4%, it was observed that increasing dilution from 5% to 15 wt.% reduced G' as seen in **Figure 5.2c**, but the effect was less pronounced compared to changes in alginate concentration, suggesting that alginate plays a more significant role in determining the mechanical properties of the hydrogel. Similarly, shear strain increased with greater dilution, but the slope change in yield graphs was less steep compared to that with increasing alginate concentration (**Figure 5.2d**).

The minimum alginate concentration required for successful crosslinking with a 10% w/w or 1 M calcium chloride ($CaCl_2$) solution was also assessed. Due to the presence of competing sodium salts in the f2 medium used for the bioink, a sufficient concentration of calcium ions was necessary to achieve adequate crosslink density in the alginate-based bioink. As shown in **Figure 5.2e**, crosslinking was not observed in 2% alginate inks, but there was a power law increase in the crosslinked modulus (G') with higher alginate concentrations, indicating that more alginate facilitates greater crosslinking density.

Finally, the yield point was plotted against alginate concentration and dilution levels to identify suitable conditions for successful 3D bioprinting and cell culture as shown in **Figure 5.2f**. Inks with less than 2% alginate showed no crosslinking and were excluded. Inks with yield points above 1000 Pa were also eliminated due to the risk of cell damage, while those with yield points below 200 Pa exhibited poor structural recovery post-printing as shown in **Figure 5.3**. The optimal window was

identified as inks with yield points between 200 and 1000 Pa, which balanced adequate crosslinking with manageable yield points.

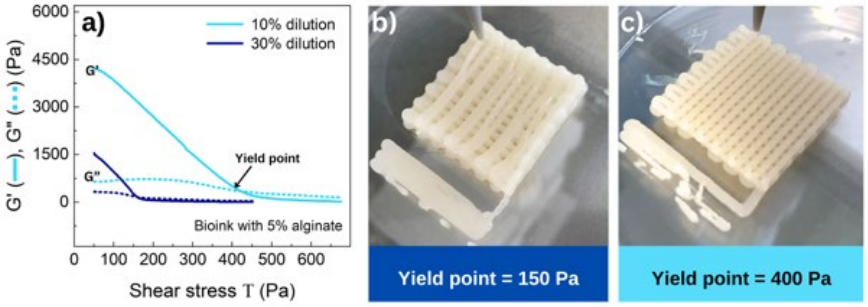

Figure 5.3. Effect of the ink yield point on structural recovery post printing defining the fidelity and complexity of printable shapes as can be seen in (a). With changing yield points, 3D printed grids exhibit changed structural integrity (b) and (c).

These results highlight the role of alginate concentration and dilution in determining the printability and mechanical integrity of bioinks. These insights provide tunability to the mechanical crosslinking of the hydrogels while maintaining printability and supporting cell viability. This optimisation was then used to study the impact of mechanical crosslinking on bioluminescence in dinoflagellates, particularly how light generation is affected by mechanical confinement and stiffness of the surrounding medium.

5.2.2. MECHANICAL TESTING OF DINO INKS

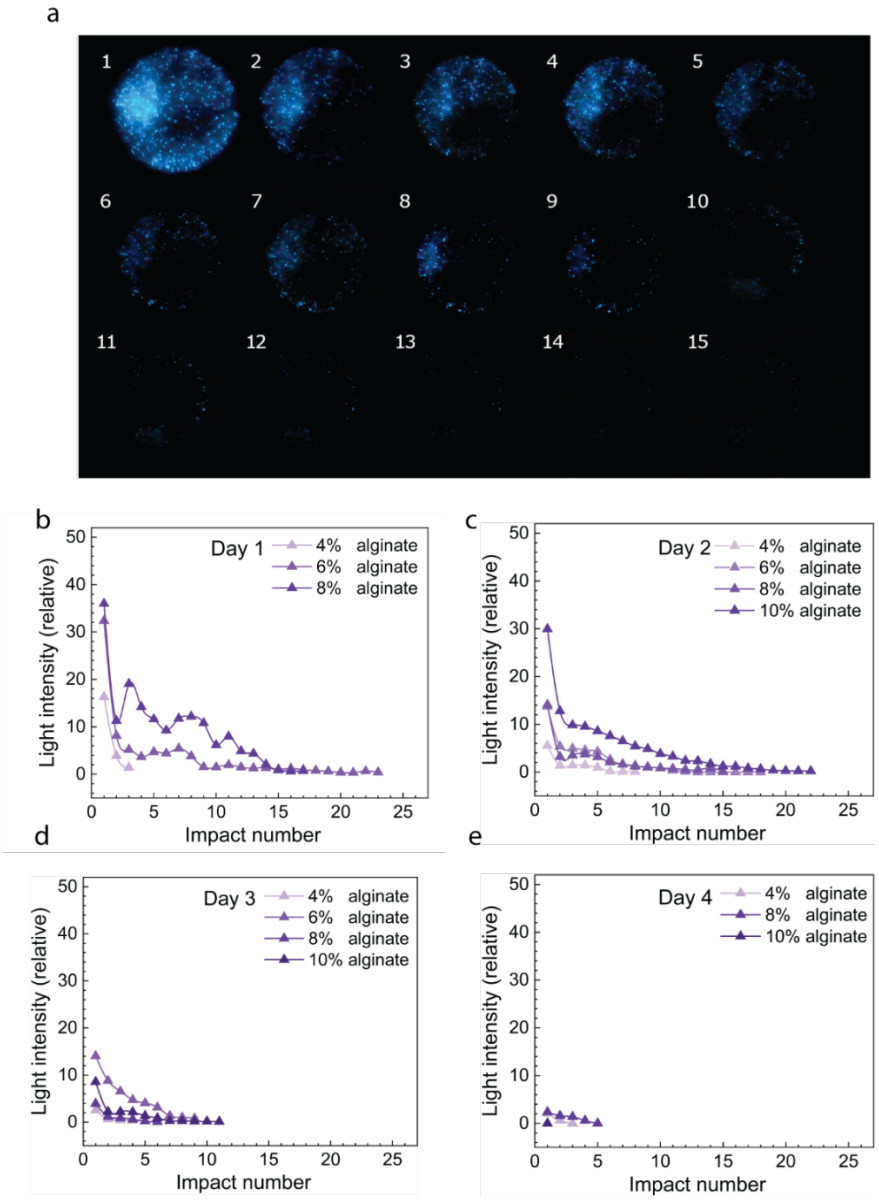

Figure 5.4: Mechano-luminescent response of the dinoflagellate inks with varying alginate concentrations over repeated mechanical impact: (a) Optical image of light emitted from successive impact on the crosslinked dinoflagellate sample placed under plexiglass and impacted with a weight (b) Average light intensity measured from the optical images (b-e) relative light intensity emitted by the dinoflagellates over multiple impact events for alginate concentrations of 4%, 6%, 8%, and 10%, measured across four consecutive days (Day 1 to Day 4)

To evaluate the effect of alginate concentration on the relative bioluminescence of dinoflagellate-embedded inks, uncrosslinked inks were poured into disc-shaped moulds and crosslinked using 1 M calcium chloride solutions. The resulting stiff, disc-shaped samples were placed in petri dishes and covered with a plexiglass plate. A marble (~95 g) was then dropped vertically from a height of approximately 11 cm onto the plexiglass at intervals of ~3 seconds, continuing until bioluminescence visibly ceased. The light emitted was captured with a camera placed at the bottom of the petri dish. **Figure 5.4a** shows the optical image of the sample upon mechanical impact. Each image corresponds to a successive single impact event, with decreasing light emission observed across subsequent impacts, reflecting the depletion of bioluminescent potential due to mechanical stimulation.

The light intensity from the optical image was processed using a Python script to obtain relative light intensity values. **Figure 5.4b-e** show the relative light intensity vs the successive impact number over different days of the sample. The intensity curves show a sharp initial decline in bioluminescence after the first few impacts, followed by a more gradual reduction, indicating a diminishing response to mechanical stress over time. Higher alginate concentrations tend to retain a slightly greater light intensity, suggesting that either the lower yield properties while printing led to better cell viability or mechanical confinement provided by the denser hydrogel matrix may help transfer the impact better, leading to a higher bioluminescent response for a longer duration.

5.3. CONCLUSIONS

3D printing of dinoflagellates into complex structures provides a way to create mechanoresponsive structures with low embodied energy. The goal of this study was to demonstrate the potential of 3D-printed mechano-responsive living inks containing the bioluminescent dinoflagellate species *Pyrocystis noctiluca* by tuning the mechanical properties of the hydrogel matrix through varying alginate concentrations, which in turn can influence the light emission response of the embedded dinoflagellates.

The rheological analysis revealed that higher alginate concentrations before crosslinking, when added to the hydrogel prior to autoclaving, lead to softer gels compared to the traditional knowledge of stiffer gels. This is due to the absorption of water from the autoclave. This leads to lower shear stress on the dinoflagellates while printing due to the reduction in yield point and viscosity of the gels before cross-linking. After cross-linking, the higher alginate gels led to stronger, more resilient hydrogels, which in turn facilitated better mechanical confinement of the dinoflagellate cells. This improved confinement appears to enhance the transfer of mechanical stress to the cells, resulting in a more sustained bioluminescent response. This insight could be interesting as it provides a method to simultaneously create soft gels for printing yet stiff gels after cross-linking.

Further, this work underscores the importance of optimising the mechanical properties of the hydrogel matrix to balance printability with the functional responsiveness of the living material. Inks with higher alginate content seemed to provide a more sustained bio-luminescent response with successive impacts over longer periods of time. Further studies need to be done to better understand the mechanism behind this. However, initial results suggest that by fine-tuning these parameters, it is possible to create living bio-hybrid materials with enhanced mechanoluminescent properties, paving the way for innovative applications in sensing, bioengineering, and responsive material systems.

5.4. MATERIALS AND METHODS

Bio ink preparation :

The ink was formulated based on the following concertation:

Component	Weight (in grams)
Guillard's F/2 medium minus silicate	100
Vivapure (cellulose-based thickener)	3
k-carrageenan	1.5
Sodium alginate	2-10
Agar agar	1.5

The bioink was prepared by first thoroughly cleaning a 400 mL conical flask with tap water and soap, rinsing it with distilled water, and using acetone as needed to remove any surfactant residues. Under sterile conditions in a biosafety cabinet, 100 g of Guillard's F/2 medium minus silicate was transferred into the flask. This medium is a standard artificial seawater solution used for culturing marine microalgae and organisms that do not require silicates. The preparation involved sequentially adding 3 g of Vivapure (a cellulose-based thickener), 1.5 g of κ-carrageenan, 2-10 g of sodium alginate (depending on the experimental setup), and 1.5 g of agar-agar to the medium. After each addition, the mixture was thoroughly mixed at 3500 rpm for 5 minutes using a milk frother to ensure homogeneity. The flask was then weighed, labelled, and covered with a breathable cotton stopper and aluminium foil before sterilising it in an autoclave set to the 'agar' cycle at 60°C with the lowest exhaust setting. Post-sterilization, all equipment was sanitised with 70% ethanol and UV light, and the weight loss due to evaporation was recorded. The bioink was mixed to eliminate any clumping as it cooled to room temperature. Subsequently, 10 g portions of the bio ink were transferred into clean containers, and concentrated dinoflagellate cultures were incrementally added under sterile conditions. The containers were labelled and prepared for rheological testing, 3D bioprinting, or further experiments, ensuring a consistent and sterile bio ink matrix for studying the mechanical properties' effects on dinoflagellate cell behaviour.

Rheological Characterization

The rheological properties of the inks were evaluated using a rotational rheometer (Haake Mars III, Thermo Scientific) equipped with a serrated plate geometry of 20 mm diameter and a gap height of 1 mm. Dynamic amplitude sweeps were

performed at a constant frequency of 1 Hz with varying stress to determine the shear storage (G') and loss (G'') moduli as a function of shear stress. The yield stress of the ink was determined through steady-state flow experiments by sweeping the shear stress and measuring the strain response. The yield stress was calculated by identifying the point of inflection on the log-log plot of shear stress versus strain. Elastic recovery was assessed using a time-dependent oscillation-rotation-oscillation (ORO) test. To simulate the printing process, a low shear stress amplitude sweep was conducted within the linear viscoelastic regime (LVR), followed by a high shear rate (10 s^{-1}) rotation to replicate the time scales and stresses experienced during the printing process. The recovery of the elastic moduli over time was then monitored using a low-amplitude oscillatory sweep.

Printing

A commercial desktop 3D printer (Ultimaker 2+) was modified by replacing the original print head with a custom-designed ink extrusion system, which included a 25 ml syringe holder and a mechanically driven syringe pump. The 3D models of the prints were processed using Cura software, with a print speed set to 10 $mm \cdot s^{-1}$ and a nozzle with an inner diameter of 1.2 mm.

Mechanical impact testing

Non crosslinked inks were poured into 60 mm diameter petri dishes, and a 1 M or 10% (w/w) calcium chloride solution was carefully layered on top of the inks. After approximately 15 minutes, the stiffening discs were flipped and allowed to crosslink for 30-40 minutes. The resulting discs were ~5 cm in diameter and ~1 cm in height. Crosslinking caused contraction of the ink, resulting in undulating surfaces and shape deformities.

The mechanical impact testing setup consisted of the following components: (a) a DSLR camera connected to a computer via Bluetooth, positioned facing upwards; (b) a wooden board with a hole cut out, placed above the camera; (c) a 3D-printed slide mounted on an aluminium extrusion for controlled marble release; and (d) a dark enclosure created by covering the setup with dense black velvet cloth to ensure near-dark conditions.

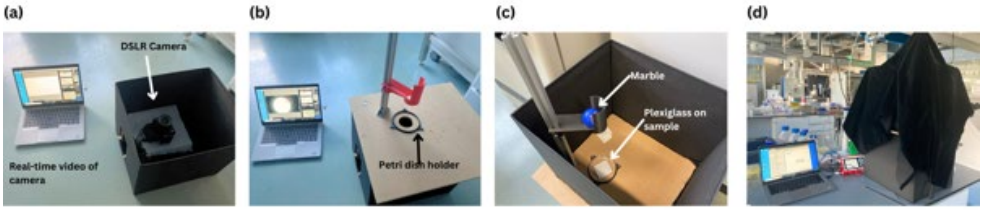

To perform testing, a crosslinked disc was placed in a petri dish covered with a square plexiglass plate. The petri dish was secured in a 3D-printed holder fixed to the wooden board. A 95-gram marble was released down the 3D-printed slide, rolling under gravity from a height of ~11 cm onto the plexiglass plate. This process was repeated at ~3-second intervals until the light emission from the sample visually diminished. The DSLR camera recorded videos of the light emission from the underside of the petri dish. A Python script was used to analyse the videos and quantify relative light intensity for each impact. The reported values represent relative, not absolute, light intensity.

5.5. REFERENCES

[1] "Studying Bioluminescent Blooms in the Arabian Sea | Lamont-Doherty Earth Observatory," available online https://lamont.columbia.edu/news/studying-bioluminescent-blooms-arabian-sea, **2024**.
[2] S. Balasubramanian, K. Yu, A. S. Meyer, E. Karana, M.-E. Aubin-Tam, *Adv. Funct. Mater.* **2021**, *31*, 2011162.
[3] J.-J. Oh, S. Ammu, V. D. Vriend, R. Kieffer, F. H. Kleiner, S. Balasubramanian, E. Karana, K. Masania, M.-E. Aubin-Tam, *Adv. Mater.* **2024**, *36*, 2305505.
[4] C. Li, Q. He, Y. Wang, Z. Wang, Z. Wang, R. Annapooranan, M. I. Latz, S. Cai, *Nat. Commun.* **2022**, *13*, 3914.
[5] C. Li, N. Schramma, Z. Wang, N. F. Qari, M. Jalaal, M. I. Latz, S. Cai, *Sci. Adv.* **2023**, *9*, eadi8643.
[6] B. Tesson, M. I. Latz, *Biophys. J.* **2015**, *108*, 1341.
[7] M. Valiadi, D. Iglesias-Rodriguez, *Microorganisms* **2013**, *1*, 3.
[8] R. Abka-khajouei, L. Tounsi, N. Shahabi, A. K. Patel, S. Abdelkafi, P. Michaud, *Mar. Drugs* **2022**, *20*, 364.

6

CONCLUSIONS AND OUTLOOK

6.1. CONCLUSIONS

It has become evident that technological advancement requires a fundamental shift in approach. Decades of rapid progress in high-performance materials and advanced computational systems have come at the cost of immense energy consumption. However, we increasingly realise that such a method of production and usage is unsustainable, and we need to radically change how build things if we wish to sustain or enhance our current way of life. Biological systems, in contrast, have developed efficient and adaptable systems. As discussed in Chapter 1, living systems share common features, illustrated in the **Figure 6.1**. While bio-inspired manufacturing holds promise, replicating the complexity of biological systems remains a significant challenge.

A central theme of this thesis is taking inspiration form bio-inspired principles **Figure 6.1** and using them to create materials and structures with transduction behaviour along with geometric complexity and integrative capabilities. Specifically, it investigates 3D printing of mechanoresponsive materials through two approaches: embedding synthetic materials like piezoelectric ceramics to mimic biological functions and incorporating living cells in hydrogels to create bio-hybrid, mechanoresponsive structures.

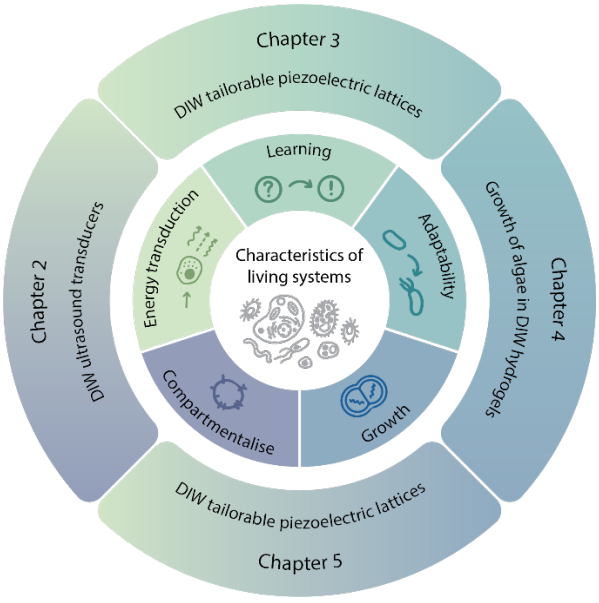

Figure 6.1 Overview of key characteristics of living systems and their connections to the thesis chapters, with colour gradients highlighting these relationships and illustrating how bio-inspired principles shape their development.

In **Chapter 2**, UV-curable piezoelectric ceramic-polymer composites were developed for Direct Ink Writing (DIW), along with structural inks. Inspired by energy transduction and compartmentalization in living systems (**Figure 6.1**), these formulations were optimized separately for performance while ensuring compatibility during co-curing. Lead-free KNLN piezo particles were synthesized with a size distribution around 3 µm to maximize volume fraction for strong piezoelectric response. This enabled dispersions with ~47.5% volume fraction in PEGDA 250 monomer. This led to the composites having d_{33} of 17 $pC \cdot N^{-1}$ and g_{33} of 32 $V \cdot m \cdot N^{-1}$, the highest $d_{33}*g_{33}$ piezoelectric constant compared to other DIW fabricated piezo composites, enabling tuneable actuation performance without the need for sintering post-printing. However, increased gravitational forces from the larger particle size prevented the recovery of the network structure post-shear thinning, leading to poor viscoelastic recovery. This was solved by in-situ UV curing of each layer, instantly increasing the yield point of the cured PEGDA matrix, allowing printed layers to support their own weight and subsequent layers.

Using COMSOL simulations, we optimized the dimensions of the support structure and piezo membrane to ensure the membrane vibrated in the first mode (out-of-plane bending vibrations), maximizing sound transmission efficiency. Transducers with varying dimensions were manufactured and analysed using Laser Doppler Vibrometry, confirming their mode shapes and frequencies matched the simulations. We studied the effect of transducer dimensions on the sound pressure generated using a commercial ultrasound microphone. Increasing dimensions enhanced sound pressure generation but further increases led to insufficient clamping and activation of mixed modes, resulting in lower incremental pressure increases. Thus, the clamping structure's dimensions need to be scaled appropriately, as demonstrated by the linear increase in slenderness. We highlighted the practical application of the printed transducer tuned to a 40 kHz operating frequency in distance measurement using time-of-flight, demonstrating the potential of these printed transducers for real-time applications.

Chapter 3 extends this methodology to designing and fabricating piezoelectric truss metamaterials with properties unavailable in bulk materials, such as maximizing longitudinal response while minimizing transverse output (e.g., in octet lattices). A generative machine learning framework has been used for the inverse design of lattice geometries adapted to specific performance.

To realize these computationally designed lattices, an embedded in-gel DIW method for UV-curable piezo composites was developed, allowing the fabrication

of thin, long structures without support materials. This technique achieved feature sizes as small as 5 mm, with the ink composition, gel rheology, tailored to support various lattice architectures. Further, printing path and printing speed were studied and optimised to minimise deformations in the printed parts providing an understanding of how both the ink and gel can be tuned to maximise performance.

Electro-mechanical testing of the lattices validated the experimental results against predictions, showing the predicted anisotropy in properties and confirming the viability of this approach. Overall, this research provides an integrated solution, from ML-based inverse design to additive manufacturing of engineered piezoelectric metamaterials building on the characteristics of energy transduction, learning and adaptability of living systems as shown in **Figure 6.1**. These advancements could pave the way for tailor-made piezoelectric transducers in biomedical and aerospace applications, overcoming the limitations of conventional materials and fabrication techniques.

Both DIW approaches in chapter 2 and 3 utilize quick UV curing in the range of a few seconds to a minute to achieve final properties, avoiding high-temperature post-processing typically required for mechanoresponsive materials. However, synthesizing piezoelectric ceramics still demands high-temperature processing (~1000°C), contributing to embodied energy costs—contrasting with biomaterials, which inherently possess lower embodied energy.

Chapter 4 investigates an engineered biocompatible ink for 3D printing *Chlamydomonas reinhardtii* (C. reinhardtii). The hydrogel was formulated to contain the essential nutrients for cell growth while ensuring favourable rheological properties to provide printability without damaging the cells. Additionally, the ink was designed to support its own weight under gravity and capillary forces and was crosslinked using $CaCl_2$ to yield highly robust 3D structures with living *C. reinhardtii* cells in them. This formulation allowed us to study shape-dependent effects on cell distribution and CO_2 absorption. Cells predominantly clustered at the periphery of the print lines, benefiting from greater gas exchange and light exposure, especially in the absence of an external carbon source (acetate). Various printed geometries were optimized for surface-to-volume ratios to enhance CO_2 capture. These findings provide fundamental insights into growth and adaptability (**Figure 6.1**) of 3D hydrogel-based photosynthetic living materials, laying the groundwork for engineered photosynthetic systems.

Chapter 5 applies these insights to fabricate mechanoresponsive, bioluminescent materials by embedding *P. Pseudonoctiluca* dinoflagellates within 3D-printed bio-

inks. Cultured dinoflagellates were formulated into alginate-based inks optimized for extrusion printing, cell viability, and mechanical robustness. Rheological investigations identified formulations balancing printability, structural integrity, and biocompatibility. Mechanoresponsive, bioluminescent structures were successfully fabricated, demonstrating that stiffer alginate matrices enhanced bioluminescence intensity, likely due to increased local stresses activating the dinoflagellates' mechano-transduction pathways. Fundamental questions remain regarding the interaction between viscoelastic matrices and cellular responses, particularly their influence on the luciferin-luciferase reaction kinetics. However, the chapter shows promise for tuning the performance of bioluminescent engineered living materials and opens up possibilities to understand the mechanism behind the tuning of light output.

6.2. OUTLOOK

This thesis highlights the potential of integrating synthetic and living materials through 3D printing to create mechano-responsive structures. The relative simplicity and material freedom provided by direct ink writing (DIW) enables the scalable fabrication of materials and structures that are conventionally difficult or energy-intensive to produce.

The first half of the thesis focusses on DIW of UV-curable piezo materials that can be co-cured with other materials and can be printed inside a gel. Printing inside a gel medium offers significantly greater design freedom by providing mechanical support, which alleviates some constraints of rheology and density on the functional ink. Additionally, the gel composition can serve as a tuning parameter, for example, by incorporating catalysts to accelerate reactions or modify material properties in situ. This can enable the fabrication of non-planar, conformable devices that bridge the gap between rigid electronics and conformable natural materials. This approach aligns with the broader evolution of electronics toward miniaturization, adaptability, and seamless integration with biological systems [1].

One key application of non-planar ultrasound arrays is in structural health monitoring for detecting impacts or fatigue in composite aircraft wings. More advanced implementations include integrating printed transducer arrays into drones or robotic systems, where strict space constraints demand compact, conformable designs. These systems could enable bio-inspired capabilities such as echolocation or a "spider-sense" for precision navigation and hazard detection. Apart from aerospace applications, non-planar ultrasound arrays have promising applications in wearable healthcare. Wearable ultrasound arrays can enable continuous blood pressure monitoring [2], at-home diagnostics, pregnancy monitoring[3], and targeted drug delivery[4] systems such as localized chemotherapy.

To realise such applications, improvements are needed in both fabrication and broader device design and testing. On the more immediate, fabrication side, DIW hardware advancements are crucial. The precision and efficiency of the process can be improved by optimizing extrusion control to prevent pressure buildup and ink instability, particularly for piezoelectric materials. Introducing multi-material pneumatic-controlled systems could offer better pressure regulation and materials flow along with simultaneously printing conducting, sensing and structural materials enabling more consistent printing of complex features[5]. Additionally, real-time ink mixing and UV-assisted curing could enhance print stability and

material properties, addressing current challenges related to ink sedimentation and polymerization control.

Beyond fabrication improvements, on the more fundamental design of these transducers, further studies could focus on optimizing printed ultrasound transducers through hierarchical material design. Simulating and printing gradient materials with improved acoustic impedance matching could enhance mechanical coupling factors[6], leading to better transduction efficiency as shown in **Figure 6.2**. Exploring the effects of different transducer shapes on sound emission could also provide valuable insights. While this study utilized circular membranes due to their ease of simulation and verification, future research could investigate more complex geometries capable of emitting sound with higher efficiency or tuning for higher bandwidth etc. depending on the application.

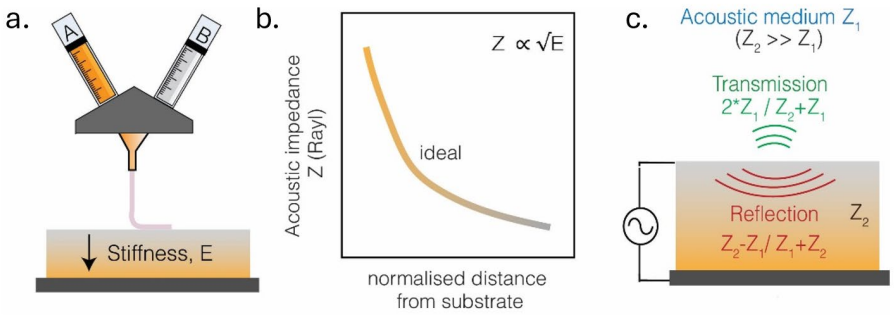

Figure 6.2: 3D printing acoustic gradients for improved coupling. (a) Multi-material printing of structures with stiffness gradients such that the top of the structure coupled with air has lowest stiffness and Z allowing for greater energy transfer while the bottom layer has high stiffness allowing greater mechanical energy transfer (k). (b) Ideal impedance gradient within the transducer achieved by tuning the stiffness of the printed composite. (c) Influence of acoustic impedance mismatch (Z_2 - Z_1) on the intensity of reflected and transmitted waves indicating importance of good acoustic coupling for high transmission efficiency.

At a broader level, scaling these technologies to create fully functional devices presents challenges that with researchers actively working on them parallelly. For instance, developing flexible and patterned electrodes that allow array connectivity while conforming to different shapes[7]. Other critical aspects include minimizing crosstalk between transducer arrays, optimizing signal processing, and extracting meaningful data. Deep learning models, similar to large language models, could assist with signal processing, enhancing accuracy and enabling real-time diagnostics. The challenging and the interesting part is to see how all these technologies come together to create functional devices of the future.

In the second half of the thesis, the focus is on the integration of living materials into engineered materials to achieve bio-hybrid materials, an area with significant potential but still relatively underexplored.

For the DIW of bioluminescent algae, this work highlights some of the control parameters that can be tuned for the development of mechanoresponsive, bioluminescent complex materials. However, the results shown are preliminary with variation arising due to the uneven surfaces of the disc-shaped samples, caused by ink shrinkage and uneven pouring during crosslinking, introduced variability in light emission measurements. Future work should address these limitations by adopting viscoelastic modelling to simulate dynamic deformation and investigate the role of strain rates on bioluminescence. Such simulations would offer deeper insights into why stiffer inks exhibit higher peak and total light emissions, potentially linked to enhanced local stresses within the matrix. Improved experimental designs, including controls for mechanical impacts and consistent testing within optimal bioluminescence windows, would strengthen the conclusions. Expanding the investigation into the biophysics of light emission by viscoelastic cells within viscoelastic materials could further unlock the potential of these living composites, paving the way for advanced applications in biosensing and soft robotics.

More broadly speaking, biological cells, such as dinoflagellates, can exhibit fast response rates comparable to synthetic materials. However, one of the primary challenges of using living materials is time. While synthetic materials require substantial energy for production, they are generally faster to fabricate compared to living materials, On the other hand, living materials typically requires weeks to grow. This in and of itself is not a limitation as once the technology is proven and scaled, parallelly growing can enable large quantities with relatively low energy.

However, another aspect of time is how long they function. Synthetic piezoelectric materials maintain stable performance for months and years and can function continuously for extended periods such as days or months. In contrast, biological materials often operate within specific timeframes, such as circadian rhythms, and require time to heal and replenish their functional potential. Enhancing their performance may involve tuning their engineered environments, such as optimizing nutrient composition in the surrounding gel, mechanical properties or introducing agents that accelerate growth and repair.

Another key challenge is maintaining cell viability. Living cells, such as algae and dinoflagellates, are highly sensitive and require a stable nutrient supply.

Encapsulation techniques using water-impermeable but gas-permeable membranes have been shown to sustain cell viability for months[8]. Further research is underway to develop effective nutrient delivery systems such as vasculature networks[9]. Addressing these together can enable hybrid systems where living cells can be combined with synthetic materials to create optimum performance properties.

Lastly, it would be interesting to see how materials perform in the combination of living and synthetic functional materials. The synthetic piezoelectric materials used in this thesis, KNLN, are biocompatible and can influence living materials by generating an electric potential in response to mechanical stress[10]. This electrical stimulation has the potential to trigger specific biological pathways in living systems. It would be interesting to explore how these materials perform when strategically combined, optimizing each for a specific function to achieve tailored properties for targeted applications.

REFERENCES:

[1] Y. Khan, A. Thielens, S. Muin, J. Ting, C. Baumbauer, A. C. Arias, *Adv. Mater.* **2020**, *32*, DOI 10.1002/adma.201905279.
[2] P. L. M. J. van Neer, L. C. J. M. Peters, R. G. F. A. Verbeek, B. Peeters, G. de Haas, L. Hörchens, L. Fillinger, T. Schrama, E. J. W. Merks-Swolfs, K. Gijsbertse, A. E. C. M. Saris, M. Mozaffarzadeh, J. M. Menssen, C. L. de Korte, J.-L. P. J. van der Steen, A. W. F. Volker, G. H. Gelinck, *Nat. Commun.* **2024**, *15*, 2802.
[3] "Pregnancy Monitoring Belt," available online https://humancentricwearables.holstcentre.com/projects/pregnancy-monitoring-belt/, **n.d.**
[4] L. J. Delaney, S. Isguven, J. R. Eisenbrey, N. J. Hickok, F. Forsberg, *Mater. Adv.* **2022**, *3*, 3023.
[5] S. G. M. Uzel, R. D. Weeks, M. Eriksson, D. Kokkinis, J. A. Lewis, *Adv. Mater. Technol.* **2022**, *7*, 2101710.
[6] C. Hou, Z. Li, C. Fei, Q. Lin, X. Luo, X. Wei, Y. Yang, Q. Lu, Y. Quan, G. Dong, Z. Chen, X. Lü, W. Bao, Y. Yang, *J. Materiomics* **2025**, 101049.
[7] H. Hu, X. Zhu, C. Wang, L. Zhang, X. Li, S. Lee, Z. Huang, R. Chen, Z. Chen, C. Wang, Y. Gu, Y. Chen, Y. Lei, T. Zhang, N. Kim, Y. Guo, Y. Teng, W. Zhou, Y. Li, A. Nomoto, S. Sternini, Q. Zhou, M. Pharr, F. L. di Scalea, S. Xu, *Sci. Adv.* **2018**, *4*, eaar3979.
[8] C. Li, N. Schramma, Z. Wang, N. F. Qari, M. Jalaal, M. I. Latz, S. Cai, *Sci. Adv.* **2023**, *9*, eadi8643.
[9] J. S. Miller, K. R. Stevens, M. T. Yang, B. M. Baker, D.-H. T. Nguyen, D. M. Cohen, E. Toro, A. A. Chen, P. A. Galie, X. Yu, R. Chaturvedi, S. N. Bhatia, C. S. Chen, *Nat. Mater.* **2012**, *11*, 768.
[10] T. Wang, W. Hu, Y. Hu, C. Yang, L. Li, J. Huang, B. Kim, Y. Gu, *Ceram. Int.* **2025**, *51*, 816.

CONTRIBUTIONS TO RESULTS

This thesis was made possible through the invaluable contributions of many individuals, listed below. I am sincerely grateful to everyone who played a role in shaping this collaborative work.

Chapter 2

This chapter was conceptualized and designed by S. Ammu (SA) and Dr K. Masania (KM). SA led the experimental execution, including materials synthesis, optimization of 3D-printing parameters, and fabrication of ultrasound transducers. SA performed Laser Doppler Vibrometry (LDV) measurements and COMSOL simulations with technical support from Dr X. Chen. Sound pressure measurements were conducted by SA in collaboration with D. Goulart. The original manuscript draft was written by SA and KM, and reviewed by Dr S. Sharma (SS), Dr F. Alijani, and Prof. P. Steenken

Chapter 3

This work was initiated by Dr. S. Kumar (SK), and Dr J. Jovanova (JJ) and SS, who developed the idea of machine learning-driven inverse design for piezoelectric lattices. P. Thakolkaran (PT) and SS developed the models and SS developed path planning strategies for 3D printing. SA and KM were involved in assessing 3D printing feasibility. SA was primarily responsible for the development of in-gel printing and the fabrication of the piezoelectric lattices, while testing setups and measurements were jointly designed and executed by SA and SS. The PCA analysis was performed by PT and SS. The original draft was co-written by SS,SA, KM and SK which was reviewed and edited by JJ.

Chapter 4

The research in this chapter originated from discussions between Dr Kunal Masania (KM), Dr Marie-Eve Aubin-Tam (ME), and Prof. Elvin Karana (EK). Vivian Vriend (VV) and Dr S. Balasubramanian conducted cell culturing. SA and VV performed rheological analysis of *C. reinhardtii*-laden bioinks to assess their 3D printability, bridgability, and mechanical stability via $CaCl_2$ crosslinking. Jeong-Joo Oh (JO) carried out the studies on the growth of embedded *C. reinhardtii* inside hydrogels, exploring the limiting factors for cell growth and CO_2 consumption, as well as the performance of photosynthetic living materials with the help of Dr R. Kieffer (RK), Dr

F. Kleiner (FK). The original draft was written by JO in collaboration with SA, RK, FK. The manuscript was edited by KM, ME, EK.

Chapter 5

The concept for this chapter was developed by KM with P. Srivastava (PS) and SA. PS was responsible for the culturing of dinoflagellates. while SA contributed to experimental design and data interpretation. SA and PS jointly investigated the rheological properties and printability of dinoflagellate-based bioinks. PS performed the impact tests with the help of SA. SA authored the original manuscript draft, which was reviewed and revised by Dr S. Schyck and KM.

ACKNOWLEDGEMENTS

First, I would like to express my deepest gratitude to my promotor and supervisor, Dr. Kunal Masania, for your constant support and guidance. Your optimism and creativity during brainstorming sessions were a constant source of inspiration, and your open, empathetic approach made even the toughest challenges feel manageable. Our impromptu coffee chats have not only helped spark ideas but also made this journey enjoyable. Your ambitious standards challenged me to reach higher, and your meticulous eye for detail elevated this work in ways I couldn't have achieved alone.

To my second promotor, Prof. Clemens Dransfeld, thank you for your invaluable insights and the clarity you brought to this project. Your practical advice and ability to zoom out to the bigger picture shaped not just my PhD but also how I approach problems as a researcher.

I am deeply honoured to have Professors Chris Bowen, Anastasiia O. Krushynska, Rinze Benedictus, and Dr. Andres Hunt on my defence committee. Thank you for dedicating your time to review my thesis and offer feedback—I am eager to engage with your perspectives during our discussion.

A special thanks to Prof. Pim Groen, who was the first promotor I started this journey with. Although he is no longer here to see the completion of this work, his influence on my development as a researcher is profound and enduring. His enthusiasm, compassion, and hands-on approach to both science and supervision are qualities that are truly contagious. The smart materials group was a proof of that! Thank you, Prof. Sybrand van der Zwaag, for stepping in guiding me through the tough time when Pim passed away. Your ability to take composed and decisive actions during challenges is inspiring.

Collaboration with many highly talented researchers has been one of the most rewarding parts of this thesis. I would like to acknowledge Prof. Peter Steeneken and Dr. Farbod Alijani from PME for our fantastic collaborations on the ultrasound and graphene projects. Your constructive and timely feedback greatly improved the quality of the work, and it was a pleasure to collaborate with you. A special thanks to Dr. Xianfeng (Vincent) Chen for your patience with LDV, COMSOL, and the many PhD wisdom sessions over tea breaks which have helped me immensely.

I am grateful to Dr. Marie-Eve Taubim for the wonderful collaboration on the algae project. Thanks to Dr. Jeong-Joo Oh for making the collaborative work such an enjoyable experience—working with you has been a pleasure.

Thanks to Dr. Jovana Jovanova and Dr. Sid Kumar from 3ME for your collaboration on the piezo lattice project. Your patience and hands-on spirit kept the project alive through all its twists and turns. A special thanks to Dr. Saurav Sharma for your immense help with this project and the thesis as a whole; our discussions on piezo topics were enlightening and helped clarify many details. Thanks, Kevin for being the OG in-gel printing guy in the lab and setting up the groundwork. Thanks, Derin, for all the long days and evenings we spent in getting the sound pressure measurements to work. Thanks, Poorva for collaborating on the really fun dinoflagellate project.

To the entire SML group- Caroline, Mu, Natalia, Deniz, Linde, Kevin, Harold, Guille, Momo, Poorva, Sarah, and everyone else—thank you for making the lab a place of growth and support. A special shout-out to Caroline for being my accountability partner—going through this journey alongside you, with shared experiences, was incredibly motivating. Thanks Mu, Natalia and Deniz for being my paranymphs! Beyond SML, I'm grateful to Vincent, Tadhg, Anton, Hugo, Silvia, Simona, and Stefano, for all the wonderful times we spent together, both inside and outside of TU Delft.

A huge thanks to Shanta for your countless acts of support; my journey would have been much more challenging without your help. I also want to acknowledge the support staff, including the new secretaries, and the technicians Dave, Alexander, Pietro, and Caitlin, for the countless acts of support that kept enabled me to keep moving forward with thesis.

Finally, my deepest thanks go to my family. Without your understanding, encouragement, and unwavering support, none of this would have been possible. Your belief in me kept me going, and I am forever grateful.

CV

Work Experience

Materials Scientist, Qlayers, Delft, Netherlands
Since Oct 2024

PhD Candidate, Shaping Matter Lab, AE, TU Delft, Netherlands
Jul 2020– Jul 2024

Researcher, Novel Aerospace Materials, AE, TU Delft, Netherlands
Oct 2018 – Jun 2020

Summer Research Intern, Holst Centre - TNO, Eindhoven, Netherlands
May 2017 – Oct 2017

Product Designer, Sickle Innovations, Indian Institute of Science, India
Oct 2015 – May 2016

Parts Quality Executive, Honda Motorcycles and Scooter India Pvt Ltd., India
Jul 2014 – Oct 2015

Education

M.Sc. Aerospace Engineering – Structures and Materials
Sep 2016 – Aug 2018
Delft University of Technology, Netherlands

Bachelor of Mechanical Engineering
Sep 2010 – May 2014
R.V. College of Engineering, India

Extracurricular Activities

Group workout instructor at X, TU Delft Sports Centre
Since Feb 2024

LIST OF PUBLICATIONS

1. **S. K. Ammu**, X. Chen, D. G. Ulcay, S. Sharma, F. Alijani, P. G. Steeneken, P. Groen, K. Masania, "3D Printing of Lead-Free Piezoelectric Ultrasound Transducers". *Adv. Mater. Technol.* 2024, 2400858. https://doi.org/10.1002/admt.202400858
2. S. Sharma*, **S.K. Ammu***, P.Thakolkaran, J. Jovanova, K. Masania, S. Kumar, "Tailorable piezoelectricity through ML-based inverse design and 3D-printing of architected materials", *submitted* . (*equal contribution)
3. J.-J. Oh, **S.K. Ammu**, V. D. Vriend, R. Kieffer, F. H. Kleiner, S. Balasubramanian, E. Karana, K. Masania, M.-E. Aubin-Tam, "Growth, Distribution, and Photosynthesis of *Chlamydomonas Reinhardtii* in 3D Hydrogels". *Adv. Mater.* 2024, 36, 2305505. https://doi.org/10.1002/adma.202305505
4. P. Srivastava, **S. K. Ammu**, S. Schyck, K. Masania, "3D Printing of tuneable dinoflagellate ink", *under preparation*.

Not pertaining to this thesis:

1. X. Chen, **S. K. Ammu,** K. Masania, P. G. Steeneken, F. Alijani, "Diamagnetic Composites for High-Q Levitating Resonators". *Adv. Sci.* 2022, 9, 2203619. https://doi.org/10.1002/advs.202203619